

POLITECNICO
MILANO 1863

SCUOLA DI INGEGNERIA INDUSTRIALE
E DELL'INFORMAZIONE

Spin manipulation and detection in semiconductor platforms

Doctoral Dissertation of:
Francesco Scali

Advisor: Prof. Federico Bottegoni
Tutor: Prof. Marco Finazzi
Year 2026 - XXXVIII Cycle

Abstract

As electronic devices shrink toward the nanometer scale, sustaining the scaling trajectory associated with Moore's law, first formulated in 1965, has become increasingly challenging. This has intensified the search for alternative approaches to information processing that remain compatible with the established semiconductor supply chain. One particularly promising route is spintronics, which seeks to harness and control the spin degree of freedom, enabling device concepts based on new operating principles. Within this context, my Ph.D. thesis examines how spin information can be converted into an electrical signal and dynamically manipulated in semiconductors. Semiconductors are appealing because they naturally interface with scalable electronics, but they also present a key challenge: spin signals are typically weak, and their characteristic length and time scales depend sensitively on band structure, scattering processes, and spin relaxation. In this thesis, I address these issues by combining calculations of optical spin injection with experimental measurements of spin-to-charge conversion and drift-diffusion modeling of spin transport. The findings identify useful platforms for spin-based applications and highlight that short spin diffusion lengths can allow very fast electrical control of spin-related signals.

Sommario

Man mano che i dispositivi elettronici si riducono fino alla scala nanometrica diventa sempre più difficile sostenere la traiettoria di scaling associata alla legge di Moore, formulata per la prima volta nel 1965. Quest'ultima è un'osservazione empirica secondo cui, mantenendo circa costanti i costi, il numero di transistor integrabili in un microchip raddoppia periodicamente (storicamente ogni 18-24 mesi). Questo aumento di densità ha portato per decenni a dispositivi più potenti, più piccoli e più efficienti, ma oggi è sempre più difficile da sostenere perché la miniaturizzazione si avvicina a limiti fisici e tecnologici. Ciò ha intensificato la ricerca di approcci alternativi per l'elaborazione dell'informazione che rimangano compatibili con l'attuale filiera industriale dei semiconduttori. Una direzione promettente è la spintronica, che mira a sfruttare e controllare il grado di libertà di spin delle particelle, introducendo dispositivi basati su nuovi principi di funzionamento. In questo contesto, la mia tesi di dottorato esamina come l'informazione di spin possa essere convertita in un segnale elettrico e manipolata dinamicamente nei semiconduttori. I semiconduttori sono attraenti perché si interfacciano naturalmente con i dispositivi elettronici; tuttavia, presentano segnali di spin tipicamente deboli che dipendono in modo sensibile dalla struttura a bande del materiale e dai processi di scattering e di rilassamento che coinvolgono i portatori di spin. In questa tesi affronto questi aspetti combinando calcoli sull'iniezione ottica di spin con misure sperimentali della conversione spin-carica e simulazioni sul trasporto di spin. I risultati individuano piattaforme utili per applicazioni logiche ed evidenziano che lunghezze di diffusione di spin ridotte sono in grado di garantire un controllo elettrico molto rapido di segnali correlati allo spin.

Contents

Abstract **i**

Sommario **iii**

Contents **v**

List of Figures **vii**

List of Tables **xv**

Introduction **1**

1 Theoretical background **7**

1.1 Spin transport 7

1.1.1 Spin populations 7

1.1.2 Spin and charge currents 10

1.2 Semiconductor spintronics 13

1.2.1 Spin-orbit interaction 14

1.2.2 Interband optical transitions 21

1.2.3 Optical orientation 25

1.2.4 $CdGeAs_2$ 33

1.2.5 Spin-charge interconversion 39

1.2.6 Spin relaxation 43

2 Methods **47**

2.1 General description of ARPES 47

2.2 Strategy for $CdGeAs_2$ growth 50

2.3 Equipment for ARPES on $CdGeAs_2$ 51

2.4 Equipment for photoinduced ISHE on $CdGeAs_2$ 51

3 Results **59**

3.1 Electronic structure of $CdGeAs_2$ 59

3.2 Optical orientation in $CdGeAs_2$ 62

3.3 Spin-to-charge conversion in $CdGeAs_2$ 73

3.4 Spin relaxation in Ge, Si, and GaAs 80

3.5 Frequency response of spin drift-diffusion 86

3.5.1 Temporal dependence of the spin density 88

3.5.2 Frequency dependence of the spin density 92

Conclusions **99**

Bibliography **101**

Appendix **109**

Acknowledgements **113**

List of Figures

1 (a) Schematic representation of the SOT-MRAM device. Writing is achieved by generating a spin accumulation at the interface between a non-magnetic metal (NM) with strong SOC and a ferromagnet (FM1), thereby rotating its magnetization. Reading is performed through a magnetic tunnel junction formed with a second ferromagnet (FM2), by detecting the tunneling magnetoresistance. (b) Illustration of the ISHE, in which a spin current density $\mathbf{j}_s$ is converted into a transverse charge current density $\mathbf{j}$, detectable as a voltage drop V under open-circuit conditions. Spin carriers with opposite spin orientations (blue and red) are deflected toward opposite edges owing to spin-orbit coupling.
(c) Geometry of a NL device. In this case, spin injection can occur electrically, using a FM-based tunnel junction, or optically, by means of optical orientation. The spin-polarized carriers can then diffuse and drift along the transport channel, before being detected with ferromagnetic or ISHE platforms. 2

2 (a) Illustration of the NL geometry implemented for manipulation of spin currents in Si with an electric field (E). In-plane spin injection occurs through optical orientation at the edges of a series of Pt stripes [21], [38]. Such spin polarization component is detected via ISHE as a voltage drop (ΔV) between two metallic pads in contact with a Pt bar and isolated from the substrate by a SiO_2 layer. The spin polarization is measured as a function of the bias voltage (V_b) applied to drift electrons during transport. (b) Map of the ΔV signal, where the Pt detector is located at the x position equal to zero. (c) The V_b dependence of the ΔV signal. (d) Scheme of the NL geometry implemented to detect spin transport in graphene. Spin-polarized electrons are injected in Ge, then transferred into graphene and detected via ISHE in Pt. The Schottky barrier between graphene and Ge is controlled by an external bias voltage (V_B). (e) Maps of the ΔV signal acquired for opposite V_B. Reversing V_B inverts ΔV because of opposite spin-polarized carriers transferred from Ge to graphene. 4

1.1 Band structures of (a) Ge, (b) Si, and (c) GaAs near the Γ point. Bands are calculated using a 30-band $\mathbf{k} \cdot \mathbf{p}$ model for Ge and GaAs, while an empirical pseudopotential model for Si. Calculations for Si are reported from Ref. [67]. The shaded colored region indicates the band gap, while the labels denote the conduction band (CB), the heavy-hole (HH), light-hole (LH), and split-off (SO) bands. 24

1.2 Scheme of the atomic energy levels at the Γ point in Ge and GaAs. The heavy hole (HH), light hole (LH) and split-off (SO) bands are separated by the spin-orbit splitting parameter Δ_{so}. The degenerate energy levels are labelled based on their m_j value. In blue and red, the allowed transitions for σ^-- and σ^+-circularly polarized light are represented, respectively. The numbers inside circles are associated to the rates of the specific transitions. 26

1.3 (a) The coefficient $\xi^{xx}(\omega)$ of the carrier-injection tensor calculated for Ge above the band gap E_g. (b) Decomposition of $\xi^{xx}(\omega)$ in single contributions from HH, LH and SO bands. (c) The imaginary part of the coefficient $\zeta^{xyz}(\omega)$ of the spin-injection pseudotensor calculated for Ge. (d) Decomposition of $\mathrm{Im}[\zeta^{xyz}(\omega)]$ in single contributions from HH, LH and SO bands. 31

1.4 (a) The photon-energy dependence of the degree of spin polarization (DSP) for Ge (dashed), Si (dashed and dotted), and GaAs (solid) illuminated by σ^--polarized light. The GaAs and Si spectra are adapted from Refs. [64], [67], respectively. 32

1.5 (a) Crystal system of $CdGeAs_2$. The conventional tetragonal unit cell is traced by black lines. (b) First bulk Brillouin zone. Labels indicate the high-symmetry points and the coordinate systems (k_x, k_y, k_z) used in the ARPES measurements of Sec. 3.3 (red), as well as (k'_x, k'_y, k'_z) corresponding to the reciprocal a^*, b^*, and c^* axes, respectively (blue). (c) Band structure near the band gap at the Γ point calculated with the 8-band $\mathbf{k} \cdot \mathbf{p}$ model. . 33

2.1 Schematic of the photoinduced ISHE setup. The laser passes through a chopper to modulate the intensity, and a photoelastic modulator (PEM) combined with a linear polarizer to alternate periodically circular polarization states. Then, the light passes through an objective lens in an off-axis configuration and is focused with a polar angle Θ with respect to the sample normal. 52

2.2 Functional scheme of a monochromator based on a Pellin-Broca prism. The prism splits the various photon frequencies (different colors) contained in the supercontinuum laser beam by dispersing them. It is mounted on a mechanical rotator, which allows the irises to select a desired wavelength in the output beam for a given rotational angle. A focusing lens is then used for coupling the beam inside a multimode fiber. 53

2.3 The photon-energy dependence of (a) the optical power W, and (b) the energy bandwidth ΔE, after the multimode fiber. The region in brown-yellow highlights the range explored in photoinduced ISHE measurements. 54

2.4 Scheme of the linear polarizer and photoelastic modulator (PEM) effects along the optical path. The PEM long axis (OA_{PEM}) is parallel to the applied strain direction along the y axis. The linear polarizer (in green) is set with an angle of $\pm 45°$ with respect to OA_{PEM}. The refractive index of the SiO_2 window (in orange) is thus modulated along the y axis (υ_y), while the one along the x axis (υ_x) remains unchanged. The light outgoing from the PEM results circularly polarized ($\sigma^{\pm}$) by applying a sufficiently strong modulation. 55

2.5 (a) Temporal dependence of the DCP for different PEM retardation $R_{\mathrm{PEM}} = 0.1\lambda$ (pink), 0.3λ (red), and 0.4λ (dark red). (b) First Bessel function $J_1(R_{\mathrm{PEM}})$. The arrows show the values of R_{PEM} used in (a). (Adapted from Ref. [105]) 57

3.1 (a) The orientation of the electron-wavevector directions k_{x}, k_{y}, k_{z} sampled in the ARPES measurements with respect to the first Brillouin zone (BZ). (b) Constant-energy map acquired at $E - E_{\mathrm{F}} = -0.2\,\mathrm{eV}$ using a photon energy of 72.5 eV. The Γ, X, and Γ′ points are indicated together with the boundary of the first BZ for $k_{\mathrm{z}} = 0\,\mathrm{Å}^{-1}$, corresponding to the red plane in panel (a). (c) Valence-band dispersion measured at a photon energy of 72.5 eV along k_{x}. The three bands forming the highest valence-band manifold are labeled VB1, VB2, and VB3, respectively, in agreement with the notation used in Sec. 1.2.4. (d) Photon-energy dependence map between 50 and 86 eV of the ARPES intensity constructed from energy distribution curves collected at the Γ point. 61

3.2 Valence-band dispersion measured with a photon energy of 86 eV along (a) k_{x} and (b) k_{y}. Panels (c) and (d) reproduce the very same band dispersions, with colored markers indicating the momentum-energy positions of VB1, VB2, and VB3. These are extracted as the peak positions of the momentum distribution curves integrated over a 25 meV energy window between −1.75 and −0.25 eV. Different colors correspond to band positions obtained from data sets acquired at photon energies of 77, 83, and 86 eV. Dark-blue lines indicate the best fits to the band positions: VB1 is well described by a parabolic dispersion, whereas VB2 and VB3 exhibit nearly linear dispersions with large band velocities. 63

3.3 Comparison between the band dispersion measured by ARPES and calculated using the 8-band $\mathbf{k} \cdot \mathbf{p}$ model proposed in Sec. 1.2.4, of VB1 (blue), VB2 (orange), and VB3 (yellow) bands along the (a) k_{x} and (b) k_{y} electron wavevector directions. 64

3.4 Scheme of the energy levels at the Γ point of $CdGeAs_2$. The conduction band (CB) is separated from the first valence band (VB1) by the band gap E_g. The VB1 band and the second valence bands (VB2) are separated by the energy splitting E_1, while VB2 and the third valence band (VB3) are separated by the energy splitting E_2. The degenerate energy levels are labelled based on their m_j value. The transitions allowed by dipole selection rules illuminating with σ^+- and σ^--polarized light are represented in red and blue, respectively. The transition rates are reported close to the arrows, being $|AB|^2 \simeq 1/7$ and $|CD|^2 \simeq 6/7$. 65

3.5 (a) The coefficients $\xi^{xx}(\omega)$ (azure), $\xi^{yy}(\omega)$ (pink), and $\xi^{zz}(\omega)$ (black) of the carrier-injection tensor calculated for $CdGeAs_2$. Decomposition of (b) $\xi^{xx}(\omega)$, (c) $\zeta^{yy}(\omega)$, and (d) $\zeta^{zz}(\omega)$ in single contributions from VB1 (green-blue), VB2 (orange), and VB3 (violet) bands. 67

3.6 (a) The imaginary part of the coefficients $\zeta^{xyz}(\omega)$ (azure), $\zeta^{yzx}(\omega)$ (pink), and $\zeta^{zxy}(\omega)$ (black) of the spin-injection pseudotensor calculated for $CdGeAs_2$. Decomposition of (b) $\mathrm{Im}[\zeta^{xyz}(\omega)]$, (c) $\mathrm{Im}[\zeta^{yzx}(\omega)]$, and (d) $\mathrm{Im}[\zeta^{zxy}(\omega)]$ in single contributions from VB1 (green-blue), VB2 (orange), and VB3 (violet) bands. 71

3.7 The photon-energy dependence of the degree of spin polarization (DSP) in $CdGeAs_2$ generated by illuminating with σ^+-polarized light with wavevector $\mathbf{k}_l$ parallel to the x (azure), y (pink), and z (black) axes, which correspond to the a, b, and c axes in Fig. 1.5a. 72

3.8 a) Sketch of the ISHE geometry. Two Au/Ti ohmic contacts are deposited on top of a $4 \times 2\,\mathrm{mm}^2$-wide and 1 mm-thick $CdGeAs_2$ sample. A circularly polarized light beam illuminates the sample at a polar angle Θ with respect to the normal in the xz plane. The u_s^x denotes the detected x-axis component of the spin-polarization unit vector, $\mathbf{j}_s$ the spin current density, and $\mathbf{j}_c$ the charge current density. b) The orientation of the ISHE geometry (black) with respect to the $\tilde{x}$, $\tilde{y}$ and $\tilde{z}$ axes (red), which correspond to the $[1\bar{1}0]$, $[c/a,\ c/a,\ -a/c]$ and [112] crystallographic directions, respectively. The angle $\eta \simeq 37°$ accounts for the in-plane alignment. 74

3.9 (a) ΔV_{ISHE} normalized to its maximum as a function of the polar angle Θ for $\hbar\omega = 0.8\,\mathrm{eV}$, $R_{\mathrm{PEM}} = 0.3\,\lambda$, and $W = 1.37\,\mathrm{mW}$. The solid red line represents the Θ-angle dependence of the spin-injection rate component $\dot{S}^x$ along the x axis in the geometry of Fig. 3.8a. (b) Dependence of ΔV_{ISHE} on the PEM retardation R_{PEM} for $\hbar\omega = 0.8\,\mathrm{eV}$, $\Theta = -27°$, and $W = 1.37\,\mathrm{mW}$. The solid red line represents the first-order Bessel function $J_1(\lambda)$. (c) ΔV_{ISHE} as a function of the incident optical power W for $\hbar\omega = 0.8\,\mathrm{eV}$, $R_{\mathrm{PEM}} = 0.3\,\lambda$, and $\Theta = -27°$. The solid red line represents a linear fit to the data. 75

3.10 Photon-energy dependence of ΔV_{ISHE}, normalized to the incident photon flux Φ, for $\Theta = -27°$ and $R_{\mathrm{PEM}} = 0.3\,\lambda$. The solid red line shows the model prediction for $\Delta V_{\mathrm{ISHE}}/\Phi$ obtained from the right-hand side of Eq. (3.20). . 77

3.11 (a) Effective carrier injection rate ξ and (b) spin injection rate ζ as functions of the photon energy for σ^- polarization, along with (c) the absorption coefficient α and (d) the degree of spin polarization DSP^x. These quantities are calculated from the 8-band $\mathbf{k}\cdot\mathbf{p}$ model described in Sec. 3.2. Individual contributions from VB1 (gray dashed line), VB2 (orange dashed line) and VB3 (green dashed line) are separated from the total ξ, ζ, α, and DSP^x (blue line). (e) Photon-energy dependence of $\mathrm{DSP}^x \alpha L_{\mathrm{s}}^2/(1+\alpha L_{\mathrm{s}})$ evaluated for a spin diffusion length $L_{\mathrm{s}} = 10\ \mu$m (blue line), 1 μm (gray line), and 100 nm (orange line). Each curve is normalized to the maximum and the gray area is the explored photon-energy range of the ISHE spectrum. The behavior for $L_{\mathrm{s}} = 100$ nm best reproduces the features of the ISHE spectrum and furnishes an estimation for the spin diffusion length in $CdGeAs_2$. 79

3.12 Optical $\tau_{\mathrm{m}}^{\mathrm{ph,o}}$ (red), acoustic $\tau_{\mathrm{m}}^{\mathrm{ph,a}}$ (blue), and inter-valley $\tau_{\mathrm{m}}^{\mathrm{ph,xx}}$ (green and violet) phonon-scattering times as functions of the electron kinetic energy E_{k} for (a) Ge ($x = \mathrm{L}$), (b) Si ($x = \Delta$), and (c) GaAs at 300 K. The vertical dotted lines indicate the thermal energy $k_{\mathrm{B}}T$. 84

3.13 Total phonon-scattering time $\tau_{\mathrm{m}}^{\mathrm{ph,tot}}$ (dashed and dotted), impurity-scattering time $\tau_{\mathrm{m}}^{\mathrm{imp}}$ (dashed), and total momentum lifetime $\tau_{\mathrm{m}}^{\mathrm{tot}}$ (solid) as functions of the doping density N_{d} for n-doped (a) Ge, (b) Si, and (c) GaAs at 300 K. 85

3.14 Elliott-Yafet (EY) spin lifetime induced by phonon scattering $\tau_s^{EY,ph}$ (dashed and dotted) and by impurity scattering $\tau_s^{EY,imp}$ (dashed), together with the Dyakonov-Perel (DP) spin lifetime τ_s^{DP} (dotted) and the total spin lifetime τ_s^{tot} (solid) as functions of the doping density N_d for n-doped (a) Ge, (b) Si, and (c) GaAs at 300 K. 87

3.15 The geometry of the simulation. A constant spin current injection happens for $x = 0$ by fixing $j_s(0,t) = j_{s,0}$. The spin density $s(x,t)$ is detected in a $10L_s$-long domain. The boundary condition at the channel end is fixed to $s(10L_s,t) = 0$, imposing a vanishing spin density far away from the injection point. The electric field $E(t)$ varies sinusoidally in time, as shown in the inset. 89

3.16 (a-c) Electron spin lifetime τ_s (black), diffusion coefficient D_e (blue), and (d-f) spin diffusion length L_s (orange) as functions of the doping density N_d for n-doped Ge, Si, and GaAs at 300 K. 90

3.17 Temporal dependence of (a) the electric field $E(t)$ and (b-c) the normalized spin density s/s_0 evaluated for an injector-detector distance $x = L_s/2$ (black), L_s (blue) and $2L_s$ (red). The amplitude of the field is (b) $E_0 = 10^3$ V/cm and (c) 10^4 V/cm, representative cases of the weak- and strong-field regimes, respectively. Spatial dependence of $s/s_0(0)$ evaluated for $E(t) < 0$ (black), $E(t) = 0$ (blue) and $E(t) > 0$ (red) with field's amplitude (d) $E_0 = 10^3$ V/cm and (e) 10^4 V/cm. Calculations are performed with a field frequency $f = 10^7$ Hz in n-doped Ge ($N_d = 5 \times 10^{18}$ cm^{-3}). . . 91

3.18 (a) The E_0 dependencies of the first s_ω/s_0 (solid lines) and second $s_{2\omega}/s_0$ (dashed lines) harmonics of s/s_0, for $x = L_s/2$ (black), $x = L_s$ (blue), and $x = 2L_s$ (red). (b) The N_d dependence of $E_{0,max}$ in Ge (green), Si (yellow) and GaAs (violet). The f dependencies of (c) s_ω/s_0 and (d) $s_{2\omega}/s_0$ for $E_0 = E_{0,max}$. The dashed vertical lines in panels (c) and (d) report the cut-off frequencies f_ω and $f_{2\omega}$, respectively. Calculations in panels (a), (c), and (d) are performed in n-doped Ge ($N_d = 5 \times 10^{18}$ cm^{-3}). 93

3.19 The cut-off frequency f_ω as a function of (a) τ_s, (b) E_0 and (c) D_e, evaluated for $x = 2L_s$. The dependencies are calculated by varying each single parameter keeping the others constant and equal to $\tau_s = 1$ ns, $E_0 = 10^3$ V/cm and $D_e = 80$ cm^2/s, respectively. 95

3.20 (a-c) The s_ω/s_0 and (d-f) f_ω as functions of the injector-detector distance x for Ge, Si, and GaAs. The N_d ranges between 1×10^{15} cm^{-3} (black), 2×10^{16} cm^{-3} (blue), 3×10^{17} cm^{-3} (red) and 5×10^{18} cm^{-3} (green). All the data are evaluated for $E_0 = E_{0,\mathrm{max}}$ and s_ω/s_0 is calculated with a field frequency $f < f_\omega$. 96

3.21 (a-c) The $s_{2\omega}/s_0$ and (d-f) $f_{2\omega}$ as functions of the injector-detector distance x for Ge, Si, and GaAs. The N_d ranges between 1×10^{15} cm^{-3} (black), 2×10^{16} cm^{-3} (blue), 3×10^{17} cm^{-3} (red) and 5×10^{18} cm^{-3} (green). All the data are evaluated for $E_0 = 10\, E_{0,\mathrm{max}}$ and $s_{2\omega}/s_0$ is calculated with a modulation frequency $f < f_{2\omega}$. 97

List of Tables

1.1 The basis functions and eigenstates at the Γ point for the three valence bands (VB1, VB2, VB3) and conduction band (CB) in the Kildal model [76]. The S wavefunction has symmetry properties of atomic s orbital; whereas the X, Y, and Z wavefunctions have symmetry properties of atomic p_{x}, p_{y}, and p_{z} orbitals, respectively. The bands are ordered from the higher to the lower in energy. 35

1.2 Effective masses evaluated along the ΓX and ΓT directions for the valence bands (VB1, VB2, VB3) and conduction band (CB) in $CdGeAs_2$. References: (1) Kildal [76]; (2) Limpijumnong and Lambrecht [77]. 37

1.3 Parameters employed in the 8-band $\mathbf{k} \cdot \mathbf{p}$ model. Note that another parameter, C_1, is set to zero following Ref. [77]. 38

3.1 Parameters employed in the calculation of τ_{m} in Ge, Si, and GaAs for intra-valley scattering, reported from Ref. [114]. m_0 is the free electron mass. 83

3.2 Parameters employed in the calculation of τ_{m} in Ge and Si for inter-valley scattering, reported from Ref. [114]. 83

3.3 Experimental and calculated spin lifetime τ_{s} of thermalized electrons at 300 K in Ge, Si, and GaAs. References: (1) Zucchetti, Bollani, Isella, *et al.* [123]; (2) Yamada, Tsukahara, Fujita, *et al.* [40]; (3) Rortais, Vergnaud, Marty, *et al.* [124]; (4) Li, Song, and Dery [117]; (5) Bottegoni, Zucchetti, Ciccacci, *et al.* [112]; (6) Zucchetti, Scali, Grassi, *et al.* [49]; (7) Dash, Sharma, Patel, *et al.* [120]; (8) Jeon, Min, Shin, *et al.* [121]; (9) Suzuki, Sasaki, Oikawa, *et al.* [119]; (10) Cheng, Wu, and Fabian [73]; (11) Li and Dery [122]; (12) Oertel, Huebner, and Oestreich [125]; (13) Jiang and Wu [126]. 88

Introduction

While spintronics has successfully advanced information storage devices based on metals, like MRAM [1], [2], STT-MRAM [3], [4], and SOT-MRAM [5]–[7], this work focuses on semiconductors. Most electronic devices used in everyday life rely on the intrinsic properties of semiconductors, where electric fields are employed to regulate charge transport. Here, I explore their potential to detect and manipulate information, rather than store it, using the spin degree of freedom of electrons. Within this context, significant advantages in terms of data processing speed and power consumption are expected. Indeed, encoding information in the electron spin could lead to a substantial reduction in energy consumption due to minimized Joule heating, as well as in capacitive effects that currently limit the speed of electronic devices [8]. Spintronic memory technologies have already demonstrated operation on ultrafast time scales, with SOT-MRAM (Fig. 1a) showing deterministic switching down to 180 ps, corresponding to a characteristic working frequency on the order of 5.6 GHz, and reported switching current densities as low as 3-6 $\times 10^{10}$ A/m^2 in optimized metal-based stacks [9]. These results highlight the potential of spin-based approaches for fast and low-power information processing. This interest is reinforced by the energy footprint of modern data centers, whose global electricity consumption is estimated at about 415 TWh in 2024, corresponding to roughly 1.5% of worldwide electricity use, while in large economies such as the United States, China, and the European Union they already account for about 2-4% of total electricity consumption [10]. These perspectives have inspired the field of semiconductor spintronics, which aims to develop high-performance, energy-efficient applications for future computing architectures [11]–[13].

One of the major challenges in employing conventional non-magnetic semiconductors for spintronic devices is their lack of a net magnetization. As a result, charge currents are typically not spin-polarized as in ferromagnets, which complicates effective electrical spin injection. Ferromagnet-based tunnel junctions [14] can accomplish this task, although spin injection efficiency is affected by interface quality and band alignment [15], [16]. Another potential solution lies in diluted magnetic semiconductors (DMS), which exhibit hybrid properties of both semiconductors and ferromagnets [17]. In this context, fundamental

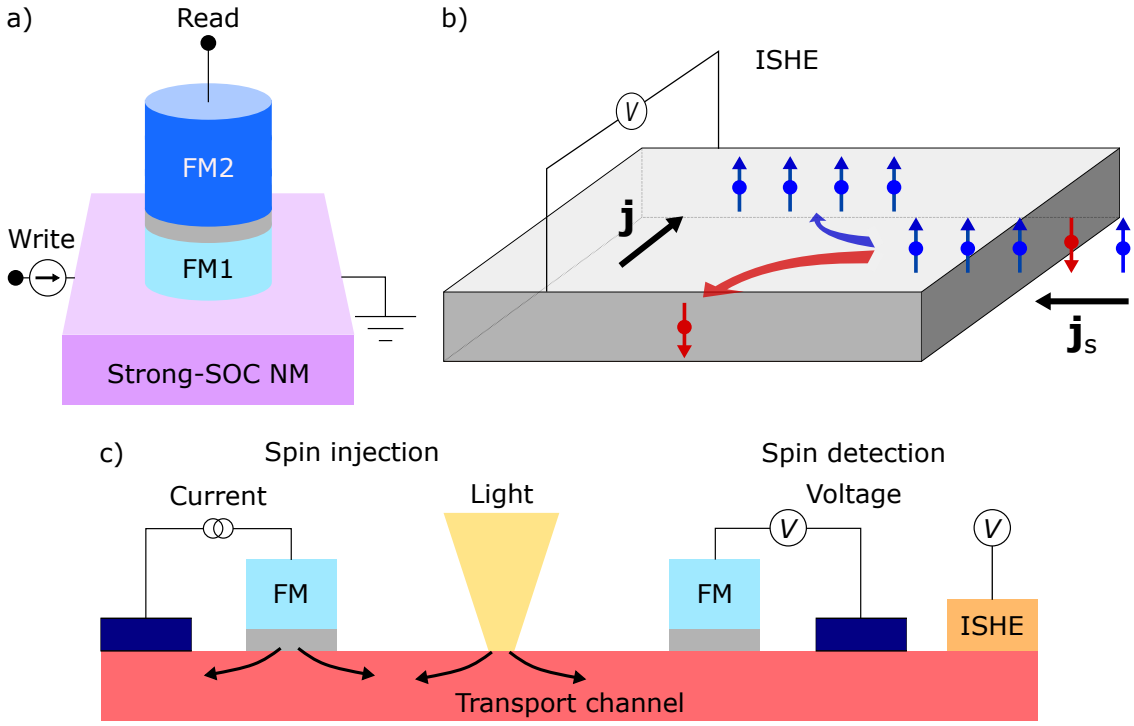

Figure 1: (a) Schematic representation of the SOT-MRAM device. Writing is achieved by generating a spin accumulation at the interface between a non-magnetic metal (NM) with strong SOC and a ferromagnet (FM1), thereby rotating its magnetization. Reading is performed through a magnetic tunnel junction formed with a second ferromagnet (FM2), by detecting the tunneling magnetoresistance. (b) Illustration of the ISHE, in which a spin current density $\mathbf{j}_s$ is converted into a transverse charge current density $\mathbf{j}$, detectable as a voltage drop V under open-circuit conditions. Spin carriers with opposite spin orientations (blue and red) are deflected toward opposite edges owing to spin-orbit coupling. (c) Geometry of a NL device. In this case, spin injection can occur electrically, using a FM-based tunnel junction, or optically, by means of optical orientation. The spin-polarized carriers can then diffuse and drift along the transport channel, before being detected with ferromagnetic or ISHE platforms.

research is focused on characterizing the magnitude and orientation of magnetization as a function of ferromagnetic particle density, as well as exploring how this magnetization affects electronic properties of materials [18]. The spin-dependent interaction at the basis of such behaviors is the exchange interaction, as in ferromagnets. Alternatively, the spin-orbit coupling (SOC) interaction can be exploited to engineer the spin at the fundamental level in non-magnetic systems. The SOC allows for the creation of nonequilibrium spin-polarized carriers in semiconductors through optical orientation [19]–[23], thus establishing a link between spintronics and optoelectronics. Based on the transfer of angular

momentum from circularly polarized photons to electrons, optical orientation was the first method of spin injection demonstrated in semiconductors [24], leading to the initial observations of spin-related mechanisms in these materials [25], [26]. Furthermore, SOC permits the interconversion between charge and spin currents, one of the most widely used mechanisms for generating and detecting nonequilibrium spin accumulations without ferromagnetic contacts [27]–[29]. The direct spin Hall effect (SHE) and its reciprocal phenomenon presented in Fig. 1b, the inverse spin Hall effect (ISHE), are spin-charge interconversion (SCI) phenomena used to electrically generate and detect spin currents [30]–[33]. Today, SHE, ISHE, and other SCI mechanisms are at the forefront of spintronics research [34]–[37].

The spin is preserved over longer time scales in semiconductors compared to metals [12], allowing for external manipulation during transport. Non-local (NL) architectures (Fig. 1c), where the spin injection is spatially separated with respect to the spin detection, are employed to modulate spin currents within the transport channel [38]–[40]. Spin manipulation is usually achieved by inducing spin precession with external magnetic fields [41]. Unfortunately, these require bulky current coils or permanent magnets poorly compatible with complementary metal–oxide–semiconductor (CMOS) technology and entail significant power consumption, thus conflicting with the demands of device miniaturization [4]. Moreover, unlike electric fields, magnetic fields are difficult to confine locally to a single device, inevitably leading to unintended control of neighboring elements in integrated circuits. Therefore, achieving spin manipulation by purely electrical means is highly desirable. SOC enables the conversion of external electric fields into effective magnetic fields, thereby inducing spin precession as in spin field-effect transistors (spin-FETs) [42]. To date, however, all-electrical spin precession have been realized only in systems where carriers are confined to low dimensions under cryogenic conditions [43]–[46]. Furthermore, this mechanism requires relatively long length scales even in semiconductors with strong SOC, which limits its applicability for sub-1-μm devices.

Alternatively, the spin polarization can also be controlled through its magnitude, rather than through its orientation. Indeed, spin-polarized electrons generated in the semiconductor can be accelerated or decelerated by an applied electric field before reaching the spin detector. Because of the finite spin lifetime and spin relaxation [11], acceleration allows spin-polarized electrons to travel longer distances before losing their polarization, whereas deceleration reduces the distance they can cover before depolarizing. As a result, the spin-dependent signal measured at the detector is electrically modulated, even at room temperature, without relying on SOC-induced spin precession, thereby enabling either high or low output voltages in a NL device or spin interconnect [47]–[49].

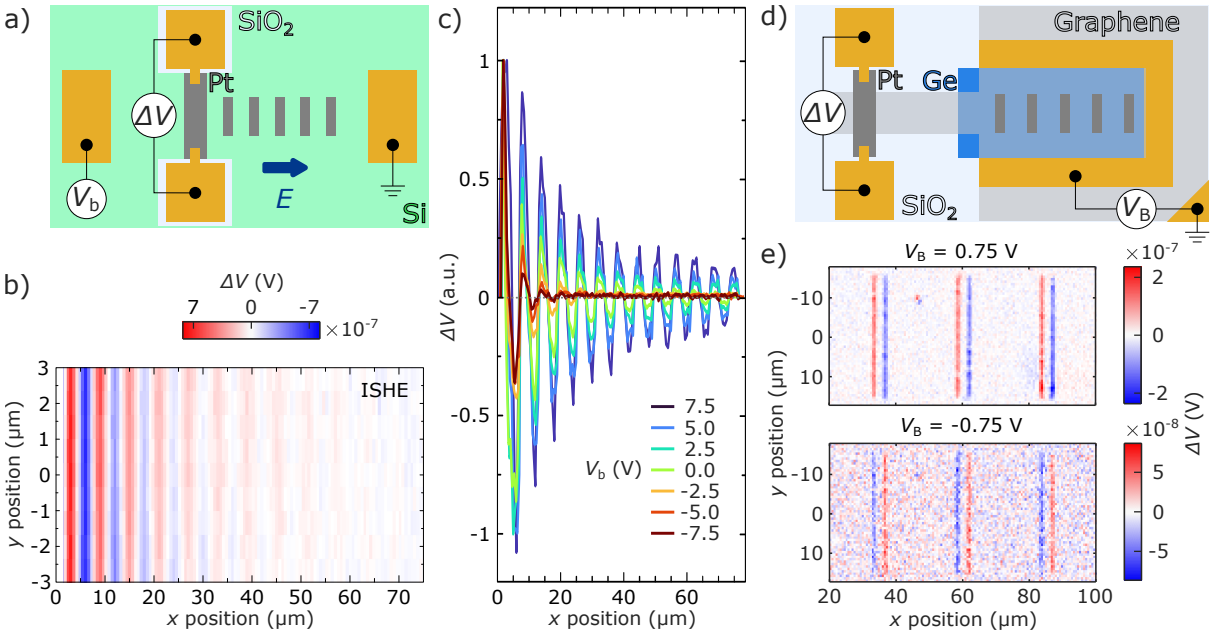

Figure 2: (a) Illustration of the NL geometry implemented for manipulation of spin currents in Si with an electric field (E). In-plane spin injection occurs through optical orientation at the edges of a series of Pt stripes [21], [38]. Such spin polarization component is detected via ISHE as a voltage drop (ΔV) between two metallic pads in contact with a Pt bar and isolated from the substrate by a SiO_2 layer. The spin polarization is measured as a function of the bias voltage (V_b) applied to drift electrons during transport. (b) Map of the ΔV signal, where the Pt detector is located at the x position equal to zero. (c) The V_b dependence of the ΔV signal. (d) Scheme of the NL geometry implemented to detect spin transport in graphene. Spin-polarized electrons are injected in Ge, then transferred into graphene and detected via ISHE in Pt. The Schottky barrier between graphene and Ge is controlled by an external bias voltage (V_B). (e) Maps of the ΔV signal acquired for opposite V_B. Reversing V_B inverts ΔV because of opposite spin-polarized carriers transferred from Ge to graphene.

This thesis presents the fruits of a three-year investigation conducted during my Ph.D. at the Politecnico di Milano, under the supervision of Doctor Carlo Zucchetti, Professor Marco Finazzi and Professor Federico Bottegoni. This period included a six-month research internship at the Kungliga Tekniska högskolan (KTH, Royal Institute of Technology) in Stockholm within the Quantum Materials group of Professor Oscar Tjernberg. Silicon (Si), as the foundation of modern electronics, and compatible materials like germanium (Ge), are studied as platforms especially attractive for integrating spintronic functionalities directly into existing technologies. Gallium arsenide (GaAs) has been extensively investigated in literature because of its direct band gap nature and strong SOC

and, therefore, it is also discussed. During my Ph.D., I investigated several NL geometries. The first device was designed to control the spin polarization magnitude in Si (Fig. 2a). Optically-oriented electrons are drifted by an in-plane electric field and collected in a platinum (Pt) bar, working as an ISHE detector [31]. The magnitude of the ISHE voltage drop decays with the distance from the detector (Fig. 2b) and the characteristic decay length is electrically modulated (Fig. 2c). How fast such manipulation can occur is a question that I address in this thesis. A second device (Fig. 2d) was designed to investigate spin transport in graphene [50]. Spin-polarized electrons are optically oriented in Ge, then transferred into graphene and detected via ISHE in Pt, while an external bias voltage controls the Schottky barrier at the junction between graphene and Ge. Maps of the ISHE signal (Fig. 2e) show an inversion of its phase reversing the bias voltage, which indicates opposite spin-polarized carriers that are transferred to graphene from Ge [51]. Because of time constraints, I will not discuss in detail these topics along the thesis. Whereas, the study of an alternative strong-SOC semiconductor, $CdGeAs_2$, and of the manipulation dynamics in the drift-diffusion regime of spin-dependent signals in NL devices are the core of this work. The valence-band manifold near the top of the valence band in $CdGeAs_2$ is mapped using angle-resolved photoemission spectroscopy (ARPES), while optical orientation and spin-to-charge conversion are demonstrated through a photoinduced ISHE experiment. Then, the frequency response of an electrically-modulated spin signal in the drift-diffusion regime is evaluated through finite-element simulations.

The thesis is structured as follows:

- Chapter 1 provides the theory that forms the foundation of this study.
- Chapter 2 describes the experimental methodology exploited for this research.
- Chapter 3 presents the primary scientific results and contributions.

The thesis concludes with a synthesis of the findings, final remarks, and the bibliography. Appendices also include the list of publications and conference proceedings. Finally, I extend my deepest gratitude to all those who have helped me during the Ph.D course.

1 | Theoretical background

This chapter presents the theoretical concepts that form the basis of the experimental work discussed in the Ch. 3. Section 1.1 introduces the key variables and parameters governing spin-polarized electron transport. Section 1.2 describes the spin-orbit coupling (SOC) interaction and provides a detailed discussion of optical orientation, spin-charge interconversion (SCI), and spin relaxation in non-magnetic bulk semiconductors.

1.1. Spin transport

In this section, the notion of spin, firstly introduced by Goudsmit and Uhlenbeck and later placed on a rigorous theoretical foundation by Dirac in 1929 through relativistic quantum mechanics, is outlined and the conventions adopted in the present work are defined. Subsequently, the analysis focuses on the spatial and temporal evolution of nonequilibrium spin populations, which is described within the drift-diffusion approach.

1.1.1. Spin populations

Each elementary particle carries an intrinsic angular momentum, the spin, whose value s is fixed and depends solely on the nature of the particle. While external fields can modify the spin state (e.g., the spin projection or polarization), they cannot change the value of s itself. This property makes spin a fundamental characteristic of the particle. The spin-statistics theorem [52] establishes a direct correspondence between the value of the spin and the quantum statistics obeyed by the particle. Particles with integer spin, such as photons, gluons, and the weak gauge bosons W and Z with spin $s = 1$, as well as the hypothetical graviton with spin $s = 2$, are classified as bosons and are described by Bose-Einstein statistics. Conversely, particles with half-integer spin, including electrons, neutrinos, and quarks with spin $s = 1/2$, are fermions and obey Fermi-Dirac statistics.

The spin degree of freedom of conduction-band electrons in a semiconductor is described by the spin angular momentum operator $\hat{\mathbf{S}}$. Its square, $\hat{S}^2$, and its projection along a quantization axis chosen as the z axis, $\hat{S}_\mathrm{z}$, are characterized by the quantum numbers

$s = 1/2$ and $m_\mathrm{s} = \pm 1/2$, respectively. The corresponding eigenvalue equations are:

$$\hat{S}^2 \left|s, m_\mathrm{s}\right\rangle = s(s+1)\hbar^2 \left|s, m_\mathrm{s}\right\rangle, \tag{1.1a}$$

$$\hat{S}_\mathrm{z} \left|s, m_\mathrm{s}\right\rangle = m_\mathrm{s}\hbar \left|s, m_\mathrm{s}\right\rangle. \tag{1.1b}$$

The eigenvalue of $\hat{S}^2$ is unique and equals $3\hbar^2/4$, while $\hat{S}_\mathrm{z}$ has two eigenvalues, $\pm\hbar/2$. The corresponding eigenstates form a basis of the two-dimensional spin Hilbert space, and a general spin state is a vector in this space, called *spinor*. The $\hat{S}_\mathrm{z}$ eigenstates are the spinors $|1/2, +1/2\rangle$ and $|1/2, -1/2\rangle$, often denoted $|\uparrow\rangle$ and $|\downarrow\rangle$. Since $\hat{S}^2$ and $\hat{S}_\mathrm{z}$ commute, *i.e.*, $[\hat{S}^2, \hat{S}_\mathrm{z}] = 0$, the spinors $|\uparrow\rangle$ and $|\downarrow\rangle$ are eigenstates of $\hat{S}^2$ as well. The spin operator can be expressed in terms of the vector of Pauli matrices $\hat{\boldsymbol{\sigma}} = (\hat{\sigma}_\mathrm{x}, \hat{\sigma}_\mathrm{y}, \hat{\sigma}_\mathrm{z})$:

$$\hat{\sigma}_\mathrm{x} = \begin{pmatrix} 0 & 1 \\ 1 & 0 \end{pmatrix}, \quad \hat{\sigma}_\mathrm{y} = \begin{pmatrix} 0 & -i \\ i & 0 \end{pmatrix}, \quad \hat{\sigma}_\mathrm{z} = \begin{pmatrix} 1 & 0 \\ 0 & -1 \end{pmatrix}, \tag{1.2}$$

as:

$$\hat{\mathbf{S}} = \frac{\hbar}{2}\hat{\boldsymbol{\sigma}}, \tag{1.3}$$

and the associated spin magnetic moment is:

$$\hat{\boldsymbol{\mu}}_\mathrm{s} = -g_\mathrm{s}\mu_\mathrm{B}\frac{\hat{\mathbf{S}}}{\hbar} \simeq -\mu_\mathrm{B}\hat{\boldsymbol{\sigma}}, \tag{1.4}$$

where $g_\mathrm{s} \simeq 2$ is the electron g-factor and μ_B is the Bohr magneton.

In the present work, spin phenomena are not discussed at the level of single particles, but rather in terms of ensembles of electrons characterized by a nonequilibrium spin population polarized along a quantization unit vector $\mathbf{u}_\mathrm{s}$. Experimentally, one probes the ensemble-averaged spin, *i.e.*, the expectation value $\langle\hat{\mathbf{S}}\rangle$, or its projection along the measurement axis. In this scenario, the appropriate framework for describing the ensemble-averaged spin is provided by the density-matrix formalism [53]. In this framework, the spin density s and the total electron density n of the ensemble are generally evaluated as:

$$s = \mathrm{Tr}(\hat{\boldsymbol{\rho}}\hat{\boldsymbol{\sigma}}), \tag{1.5a}$$

$$n = \mathrm{Tr}(\hat{\boldsymbol{\rho}}), \tag{1.5b}$$

where $\hat{\boldsymbol{\rho}}$ is the density-matrix operator. Here, we restrict ourselves to resolving n into spin-up and spin-down electron densities, defined with respect to $\mathbf{u}_\mathrm{s}$, and to describe spin-polarized transport through the drift-diffusion model. Although this approach is not fully rigorous, it nevertheless provides quantitative predictions for spin-transport phenomena [47]–[49]. If the spin-resolved electron densities are $n_\uparrow$ and $n_\downarrow$, the total electron density is:

$$n = n_\uparrow + n_\downarrow, \tag{1.6}$$

whereas the spin density is:

$$s = n_\uparrow - n_\downarrow. \tag{1.7}$$

This procedure yields a scalar spin density polarized along the $\mathbf{u}_\mathrm{s}$ vector. In many experimental configurations, the measured signal is sensitive primarily to a single spin component along a specific axis set by the probe, which can be calculated by projecting $\mathbf{u}_\mathrm{s}$ along the measurement axis. In non-magnetic semiconductors, the equilibrium spin density vanishes in the absence of external fields. This stems from time-reversal symmetry, which implies Kramers degeneracy [54]: electronic states at opposite crystal momenta and with opposite spin character have the same energy and are related by time-reversal. This yields:

$$E(\mathbf{k}, \uparrow) = E(-\mathbf{k}, \downarrow), \tag{1.8}$$

where E is the band energy and $\mathbf{k}$ is the electron wavevector. This concept will be revisited in the next section, where the band structure is discussed in more detail. As a result, under equilibrium conditions the spin-up and spin-down electronic states are equally populated, leading to identical spin-resolved electron densities, $n_\uparrow = n_\downarrow$, and hence to a vanishing spin density, $s = 0$. A nonequilibrium spin population with a finite polarization is thus needed to study spin phenomena in these systems and typically generated via optical orientation or electrical spin injection. To quantify the nonequilibrium spin polarization, it is convenient to introduce the spin polarization vector $\mathbf{P}_\mathrm{s}$ and the degree of spin polarization (DSP):

$$\mathbf{P}_\mathrm{s} = \frac{s}{n}\,\mathbf{u}_\mathrm{s} = \mathrm{DSP}\,\mathbf{u}_\mathrm{s}, \tag{1.9}$$

which measure the relative imbalance between spin-up and spin-down electron densities.

1.1.2. Spin and charge currents

Carrier transport describes how the total electron density n varies in space and time, and it is governed by the continuity equation [11]:

$$\frac{\partial n}{\partial t} = -\nabla \cdot \mathbf{J}, \tag{1.10}$$

where $\mathbf{J}$ is the electron particle current density. This can be described within the drift-diffusion model by the equation [11]:

$$\mathbf{J} = -\mu_{\mathrm{e}} n \mathbf{E} - D_{\mathrm{e}} \nabla n, \tag{1.11}$$

where μ_{e} is the electron mobility, D_{e} is the electron diffusion coefficient, and $\mathbf{E}$ the electric field. The diffusion coefficient is given by $D_{\mathrm{e}} = \mu_{\mathrm{e}} k_{\mathrm{B}} T/q$, where k_{B} is the Boltzmann constant and T the absolute temperature. The Eq. (1.10) expresses the conservation of particles: the electron density within a given volume can increase only if the current flowing into the volume exceeds the current flowing out. Equivalently, this condition corresponds to $\nabla \cdot \mathbf{J} < 0$. The Eq. (1.11) describes the generation of a current either via the drift of electrons under an externally applied electric field $\mathbf{E}$ or as a result of diffusion driven by a spatial imbalance in the electron density n. For this reason, Eq. (1.11) is commonly referred to as the drift-diffusion equation. Both Eqs. (1.10) and (1.11) are written in terms of the particle current density $\mathbf{J}$ rather than the charge current density $\mathbf{j}$ in order to avoid ambiguity in the current direction appearing in the continuity equation. For electrons, the charge current density is $\mathbf{j} = -q\,\mathbf{J}$, being q the elementary charge. Consequently, the drift-diffusion and continuity equations take the form:

$$\mathbf{j} = q\left(\mu_{\mathrm{e}} n \mathbf{E} + D_{\mathrm{e}} \nabla n\right), \tag{1.12a}$$

$$\frac{\partial n}{\partial t} = \frac{\nabla \cdot \mathbf{j}}{q}. \tag{1.12b}$$

An analogous description applies to spin-polarized transport. Introducing spin-resolved electron densities $n_\uparrow$ and $n_\downarrow$, their dynamics obey a similar continuity equation:

$$\frac{\partial n_\lambda}{\partial t} = \frac{\nabla \cdot \mathbf{j}_\lambda}{q} - w\left(n_\lambda - n_{-\lambda}\right), \tag{1.13}$$

where $\lambda = \uparrow (\downarrow)$, $-\lambda = \downarrow (\uparrow)$. The additional term $w\,(n_\lambda - n_{-\lambda})$, which appears when compared with the continuity equation in Eq. (1.12b), accounts for spin-flip processes, with w denoting the spin-flip rate. To first approximation, spin-flip processes are proportional to the spin-resolved electron density and therefore lead to a redistribution of the spin population in favor of spin depolarization, ultimately restoring the equilibrium condition of vanishing spin density. In this context, the additional term acts as a sink and a source term for the majority and minority spin-resolved electron densities, respectively. Note that, when the total electron density is calculated by substituting Eq. (1.13), evaluated for each spin projection, in Eq. (1.6), the contribution correctly disappears. The spin-resolved charge current densities read:

$$\mathbf{j}_\lambda = q\left(\mu_\mathrm{e} n_\lambda \mathbf{E} + D_\mathrm{e} \nabla n_\lambda\right), \tag{1.14}$$

following the drift-diffusion equation of Eq. (1.12a) applied for each spin-resolved electron density. At this stage, we define the total charge and spin-polarized current densities as:

$$\mathbf{j} = \mathbf{j}_\uparrow + \mathbf{j}_\downarrow, \tag{1.15a}$$

$$\mathbf{j}_\mathrm{s} = \mathbf{j}_\uparrow - \mathbf{j}_\downarrow. \tag{1.15b}$$

In this way, Eq. (1.15a) fully satisfies Eq. (1.12a), which can be recovered by substituting Eq. (1.14) evaluated for each spin projection. Moreover, one obtains the spin drift-diffusion equation:

$$\mathbf{j}_\mathrm{s} = q\left(\mu_\mathrm{e} s \mathbf{E} + D_\mathrm{e} \nabla s\right), \tag{1.16}$$

and the spin continuity equation:

$$\frac{\partial s}{\partial t} = \frac{\nabla \cdot \mathbf{j}_\mathrm{s}}{q} - \frac{s}{\tau_\mathrm{s}}, \tag{1.17}$$

where we have defined the spin lifetime as $\tau_\mathrm{s} = (2w)^{-1}$. The spin continuity and drift-diffusion equations constitute the theoretical basis of spin transport in this work. They will be explicitly solved whenever the spatial and temporal evolution of spin-polarized electrons is required, with the solution depending on the spin lifetime. As in the case of charge transport, Eq. (1.16) indicates that a spin-polarized current can be generated either by drift in a medium with a finite spin polarization or by diffusion resulting from a

spatially inhomogeneous spin distribution. In these equations, the electron mobility and diffusion coefficient are assumed to be identical for both spin projections, and no spin-selective phenomena are included. Spin depolarization, also known as spin relaxation, mediated by spin-flip processes is whereas accounted by the spin lifetime, which must be calculated by considering microscopic mechanisms for quantitative predictions.

The Eqs. (1.16) and (1.17) present an analytical solution if the electric field is time-independent. We can start by solving them in the absence of an external electric field drifting electrons, *i.e.*, $\mathbf{E} = 0$. In a one-dimensional (1D) geometry with the boundary condition $s(x, t = 0) = s_0\delta(x)$, being s_0 the initial spin density localized in $x = 0$ and $\delta(x)$ the Dirac delta function, the solution is:

$$s(x,t) = \frac{s_0}{2\sqrt{\pi}L_s} e^{-x^2/4L_s^2} e^{-t/\tau_s}, \tag{1.18}$$

where we have defined the spin diffusion length as $L_s = \sqrt{D_e\tau_s}$. The first exponential term describes the spatial diffusion of the spin population, while the second represents its temporal relaxation. The time-dependent behavior of s can be determined by integrating over the 1D space:

$$s(t) = \int_{-\infty}^{+\infty} s(x,t)dx = s_0 e^{-t/\tau_s}. \tag{1.19}$$

Thus, τ_s characterizes the temporal decay of the spin population and is therefore referred to as the spin lifetime, or spin relaxation time. In general, once the perturbations that sustain a nonequilibrium spin state are removed, the spin density relaxes toward its equilibrium value, which is zero in non-magnetic semiconductors, on a characteristic timescale set by τ_s. We can now solve Eqs. (1.16) and (1.17) in the steady-state regime, with $\partial s/\partial t = 0$, and for $\mathbf{E} = 0$. The steady-state spin density satisfies:

$$\nabla^2 s = \frac{s}{L_s^2}. \tag{1.20}$$

In one dimension, the solution for a fixed spin density at $x = 0$ in a positive semi-infinite domain reads:

$$\mathbf{s}(x) = \mathbf{s}_0 e^{-x/L_s}. \tag{1.21}$$

Thus, L_s characterizes the exponential decay of the spin density away from the injection

point as a result of diffusion and spin relaxation, and is therefore referred to as the spin diffusion length. Equivalently, L_s represents the average distance over which spin-polarized electrons propagate before losing their spin polarization. Both τ_s and L_s are characteristic quantities that govern spin-polarized transport in non-magnetic semiconductors and constitute the primary physical objects of investigation in this work.

In analogy with the definition of the spin polarization in Eq. (1.9), we define the spin current polarization $\mathbf{P}_\mathrm{j}$ as:

$$P_\mathrm{j}^i = \frac{j_\mathrm{s}^i}{j^i}, \quad i = x, y, z. \tag{1.22}$$

This quantity is useful to distinguish a distinct situation. When the charge current density vanishes, *i.e.*, $\mathbf{j} = 0$, while a finite spin current density $\mathbf{j}_\mathrm{s}$ is present, the spin current polarization diverges. This regime is referred to as a pure spin current, to distinguish it from the general case of a spin-polarized current, or simply spin current. Such a condition can be realized, for example, in the absence of an electric field when a spin imbalance exists without any charge imbalance, as described by Eqs. (1.12a) and (1.16). In this situation, spin-up and spin-down electrons flow in opposite directions to compensate the spin imbalance s, resulting in zero net charge transport. This regime is of particular interest in spintronics, as it offers the possibility to transport information encoded in the electron spin with negligible energy loss, effectively avoiding Joule heating. In practice, however, the generation of a pure spin current often requires a charge current, and its detection typically involves conversion into an electrical signal. The transformations between charge and pure spin currents, known as spin-charge interconversion, is also investigated in this thesis. Furthermore, any generic spin current can be decomposed into a combination of a pure charge current and a pure spin current, meaning that spin-charge interconversion processes are generally applicable to spin currents as well.

1.2. Semiconductor spintronics

Semiconductor spintronics is concerned with the study of equilibrium and nonequilibrium spin populations in semiconductors and semiconductor heterostructures, including spin generation, transport, manipulation, and detection, as well as spin dynamics and relaxation. In non-magnetic semiconductors, spin-orbit coupling is the key microscopic interaction governing spin behavior in all these processes. Given its central role, spin-orbit coupling is introduced in detail in the following section. Subsequently, spin-orbit-related phenomena, including optical orientation, spin-charge interconversion, and spin relax-

ation, are discussed. The present work focuses on bulk Ge, Si, GaAs, and $CdGeAs_2$, for which the relevant processes and mechanisms are described in detail.

1.2.1. Spin-orbit interaction

Spin-orbit interaction is a relativistic quantum mechanical phenomenon that results in the lifting of the degeneracy of single-particle energy levels in both atomic and solid-state physics. In solids, electronic properties are often described using the nonrelativistic Schrödinger equation as a first approximation, for instance in band-structure calculations, which reads:

$$i\hbar\frac{\partial}{\partial t}\Psi(\mathbf{r},t) = \hat{H}\Psi(\mathbf{r},t), \tag{1.23}$$

where i is the imaginary unit, $\hbar$ is the reduced Plank constant, $\Psi(\mathbf{r},t)$ is the wavefunction of a nonrelativistic particle, and $\hat{H}$ is the Hamiltonian operator corresponding to the total energy of the particle. The latter is related to the momentum operator $\hat{\mathbf{p}} = -i\hbar\nabla$ and the potential energy function $V(\mathbf{r},t)$, representing the environment surrounding the particle, through the equation:

$$\hat{H} = \frac{\hat{\mathbf{p}}^2}{2m} + V(\mathbf{r},t), \tag{1.24}$$

where m is the particle mass. In the case of an electron moving in the periodic electrostatic potential of a crystal, *i.e.*, the lattice potential, the Hamiltonian is not an explicit function of time. The Eq. 1.23 can therefore be solved by separation of variables, *i.e.*, by seeking solutions that factorize into spatial and temporal components. The resulting wavefunction takes the form:

$$\Psi(\mathbf{r},t) = \psi(\mathbf{r})e^{-iEt/\hbar}, \tag{1.25}$$

being E the electron energy. The resulting wavefunctions are therefore standing waves, commonly referred to as stationary states, since their only time dependence is given by a phase factor, which cancels out when computing the probability density. The spatial part of the full wavefunction solves the eigenvalue equation:

$$\hat{H}\psi(\mathbf{r}) = E\psi(\mathbf{r}), \tag{1.26}$$

which allows to determine the E values. Solutions to Eq. 1.26 for a lattice potential energy $V(\mathbf{r})$ are represented by the Bloch states, which are plane waves modulated by periodic functions. These are defined as:

$$\psi(\mathbf{r}) = e^{i\mathbf{k}\cdot\mathbf{r}}u(\mathbf{r}), \tag{1.27}$$

being $\mathbf{k}$ the electron wavevector and $u(\mathbf{r})$ a periodic function with the same periodicity of the crystal lattice. These eigenstates are denoted as $\psi_{n\mathbf{k}}(\mathbf{r})$, where n is a discrete index, referred to as the band index. This index arises because multiple wavefunctions exist for a given wavevector $\mathbf{k}$, each characterized by a different periodic component $u_{n\mathbf{k}}(\mathbf{r})$. Within a given band, the eigenstates $\psi_{n\mathbf{k}}(\mathbf{r})$ vary continuously with $\mathbf{k}$, as does the corresponding energy. Moreover, the Bloch states are defined only up to a reciprocal lattice vector $\mathbf{K}$, such that $\psi_{n\mathbf{k}} = \psi_{n(\mathbf{k}+\mathbf{K})}$. Consequently, the wavevector $\mathbf{k}$ can be restricted to the first Brillouin zone (BZ) of the reciprocal lattice without loss of generality. For the $u_{n\mathbf{k}}(\mathbf{r})$ functions it holds an eigenvalue equation similar to Eq. 1.26:

$$\hat{H}_{\mathbf{k}}u_{n\mathbf{k}}(\mathbf{r}) = \left[\frac{(\hat{\mathbf{p}} + \hbar\mathbf{k})^2}{2m_0} + V(\mathbf{r})\right] u_{n\mathbf{k}}(\mathbf{r}) = E_{n\mathbf{k}}u_{n\mathbf{k}}(\mathbf{r}), \tag{1.28}$$

with the boundary conditions:

$$u_{n\mathbf{k}}(\mathbf{r}) = u_{n\mathbf{k}}(\mathbf{r} + \mathbf{R}), \tag{1.29}$$

where m_0 is the electron mass, $\hbar\mathbf{k}$ is called the crystal momentum, and $\mathbf{R}$ is any real lattice vector. In this context, $\mathbf{k}$ acts as a parameter of the Hamiltonian, leading to a continuous family of eigenvalues $E_{n\mathbf{k}}$ that depend on the continuous variable $\mathbf{k}$. This naturally introduces the fundamental concept of an electronic band structure. The Eq. (1.28) cannot be solved analytically for a realistic lattice potential. Therefore, the electronic band structure is computed using approximate methods, such as $\mathbf{k}\cdot\mathbf{p}$ [55], [56], tight-binding [57], empirical pseudopotential [58], [59] or first-principles [60] approaches.

When relativistic effects are neglected, the Schrödinger Hamiltonian defined in Eq. (1.24) is spin independent, so each Bloch band is at least twofold degenerate with respect to spin. Including spin-orbit coupling adds a spin- and momentum-dependent term that couples orbital and spin degrees of freedom, thereby lifting band degeneracies and producing the characteristic spin-orbit splittings of the electronic structure. Within the nonrelativistic description, spin-orbit interaction is thus included as a relativistic correction to the Schrödinger equation. Near the Brillouin-zone center where $\mathbf{k} = 0$, *i.e.*, the Γ point, the

spin-orbit interaction term can be written in the form:

$$\hat{H}_{\mathrm{so}} = \frac{\hbar}{4m_0^2c^2}\left(\nabla V(\mathbf{r}) \times \hat{\mathbf{p}}\right) \cdot \hat{\boldsymbol{\sigma}}, \tag{1.30}$$

where $\hat{\boldsymbol{\sigma}}$ is the vector of Pauli matrices [20]. To outline the origin of this correction, the appropriate starting point is the Dirac equation, which provides a fundamental description of electronic systems by naturally incorporating both electron spin and relativistic effects. Within this framework, spin and spin-orbit coupling emerge directly from first principles, as can be seen by starting from the relativistic expression for the total energy of a particle, *i.e.*, the relativistic energy-momentum relation:

$$\hat{H}^2 = c^2\hat{\mathbf{p}}^2 + m^2c^4, \tag{1.31}$$

where m is the rest mass. From Eq. (1.31), we first introduce a relativistic correction to the Schrödinger Hamiltonian by using a Taylor expansion. This correction, while not corresponding to the spin-orbit coupling term, exhibits the same $1/c^2$ dependence. To this end, we expand the relativistic energy-momentum relation in the limit $\hat{\mathbf{p}} \ll mc$:

$$\begin{aligned}
\hat{H} = \sqrt{c^2\hat{\mathbf{p}}^2 + m^2c^4} &= mc^2\sqrt{1 + \left(\frac{\hat{\mathbf{p}}}{mc}\right)^2} \\
&\simeq mc^2\left[\,1 + \frac{\hat{\mathbf{p}}^2}{2m^2c^2} - \frac{\hat{\mathbf{p}}^4}{8m^4c^4} + O\left(\frac{\hat{\mathbf{p}}^6}{m^6c^6}\right)\right] \\
&\simeq mc^2 + \frac{\hat{\mathbf{p}}^2}{2m} - \frac{\hat{\mathbf{p}}^4}{8m^3c^2} + O\left(\frac{\hat{\mathbf{p}}^6}{m^5c^4}\right).
\end{aligned} \tag{1.32}$$

The term mc^2 is a constant contribution to the total energy and can be absorbed into the energy E in Eq. (1.25), resulting only in an additional global phase. The term $\hat{\mathbf{p}}^2/2m$ is the nonrelativistic kinetic energy. The term $-\hat{\mathbf{p}}^4/8m^3c^2$ is the relativistic correction to the kinetic energy, and it is typically treated as a small perturbation to the Schrödinger Hamiltonian. The spin-orbit coupling correction originates in the presence of an electric field, *i.e.*, a spatially varying electrostatic potential energy $V(\mathbf{r})$, as can be inferred from Eq. (1.30). In atoms, the internal electric field originates from the nuclear Coulomb potential, whereas in solids it arises from the spatial gradients of the lattice potential. The scalar potential ϕ and the vector potential $\mathbf{A}$ can be introduced in Eq. (1.31) by performing the substitutions $\hat{\mathbf{p}} \to \hat{\mathbf{p}} - e\mathbf{A}$ and $\hat{H} \to \hat{H} - e\phi$, where e is the electron charge. This procedure yields:

$$(\hat{H} - e\phi)^2 = c^2(\hat{\mathbf{p}} - e\mathbf{A})^2 + m^2c^4. \tag{1.33}$$

From this expression of the relativistic dispersion relation, we get the relativistic wave equation:

$$\left[(\hat{H} - e\phi)^2 - c^2(\hat{\mathbf{p}} - e\mathbf{A})^2 - m^2c^4\right]\Psi = 0. \tag{1.34}$$

The Eq. (1.34) can be rewritten in the form:

$$\left[\hat{H} - e\phi - c\hat{\boldsymbol{\alpha}}\cdot(\hat{\mathbf{p}} - e\mathbf{A}) - \hat{\beta}mc^2\right]\left[\hat{H} - e\phi + c\hat{\boldsymbol{\alpha}}\cdot(\hat{\mathbf{p}} - e\mathbf{A}) + \hat{\beta}mc^2\right]\Psi = 0. \tag{1.35}$$

In Eq. (1.35), $\hat{\boldsymbol{\alpha}}$ and $\hat{\beta}$ are the Dirac operators satisfying:

$$\{\hat{\alpha}_i, \alpha_j\} = 2\delta_{ij}\mathbb{I}, \qquad \{\hat{\alpha}_i, \hat{\beta}\} = 0, \qquad \hat{\beta}^2 = \mathbb{I}. \tag{1.36}$$

where $\{A, B\} = AB + BA$ denotes the anticommutator and $\mathbb{I}$ is the identity matrix. We consider only the first term in Eq. (1.35), which yields a Hamiltonian that is linear in the momentum operator $\hat{\mathbf{p}}$. It is worth noting that any solution of the first part of Eq. (1.35) is also a solution of the full equation. In this manner, one obtains a relativistic wave equation that is first order in time, namely the Dirac equation, in the presence of electric and magnetic fields:

$$\left[\hat{H} - e\phi - c\hat{\boldsymbol{\alpha}}\cdot(\hat{\mathbf{p}} - e\mathbf{A}) - \hat{\beta}mc^2\right]\Psi = 0, \tag{1.37}$$

The latter can be rewritten to explicate the Dirac Hamiltonian by substituting $\hat{H} = i\hbar\partial_t$:

$$i\hbar\frac{\partial}{\partial t}\Psi = \hat{H}_D\Psi, \tag{1.38a}$$

$$\hat{H}_{\mathrm{D}} = e\phi + c\hat{\boldsymbol{\alpha}}\cdot(\hat{\mathbf{p}} - e\mathbf{A}) + \hat{\beta}mc^2. \tag{1.38b}$$

The Foldy-Wouthuysen (FW) low-energy expansion [61] of the Dirac Hamiltonian, valid for time-independent weak fields, can be performed to obtain relativistic corrections to the nonrelativistic Hamiltonian. This expansion employs the Baker-Campbell-Hausdorff

(BCH) identity and introduces two operators, $\hat{\mathcal{E}}$ and $\hat{\mathcal{O}}$, which are even and odd with respect to $\hat{\beta}$, meaning that they commute and anticommute with $\hat{\beta}$, respectively. The operators are given by:

$$\hat{\mathcal{E}} \equiv e\,\phi\,\mathbb{I} \qquad \longrightarrow \quad [\hat{\beta}, \hat{\mathcal{E}}] = 0, \tag{1.39a}$$

$$\hat{\mathcal{O}} \equiv c\,\hat{\boldsymbol{\alpha}} \cdot (\hat{\mathbf{p}} - e\mathbf{A}) \quad \longrightarrow \quad \{\hat{\beta}, \hat{\mathcal{O}}\} = 0. \tag{1.39b}$$

where $[A, B] = AB - BA$ denotes the commutator. The even and odd relations are consequences of the conditions satisfied by the Dirac matrices, presented in Eq. (1.36). It can be noted that the even operator $\hat{\mathcal{E}}$ corresponds to the electrostatic potential energy $V(\mathbf{r})$, and it is therefore substituted in the subsequent analysis. After applying the FW unitary transformation, using the BCH formula for the expansion and dropping terms beyond $1/c^2$, the FW Hamiltonian is given by [62]:

$$\hat{H}_{\mathrm{FW}} = \hat{\beta}mc^2 + V(\mathbf{r}) + \frac{\hat{\beta}\hat{\mathcal{O}}^2}{2mc^2} - \frac{[\hat{\mathcal{O}}, [\hat{\mathcal{O}}, V(\mathbf{r})]]}{8m^2c^4} - \frac{\hat{\beta}\hat{\mathcal{O}}^4}{8m^3c^6} + \ldots . \tag{1.40}$$

The problem is now reduced to evaluate $\hat{\mathcal{O}}^2$, $[\hat{\mathcal{O}}, [\hat{\mathcal{O}}, V(\mathbf{r})]]$, and $\hat{\mathcal{O}}^4$. In the standard Dirac (4×4) representation, the Dirac matrices $\hat{\boldsymbol{\alpha}}$ are connected to the Pauli matrices $\hat{\boldsymbol{\sigma}}$ by the relation:

$$\hat{\alpha}_i = \begin{pmatrix} 0 & \hat{\sigma}_i \\ \hat{\sigma}_i & 0 \end{pmatrix}, \quad i = x, y, z. \tag{1.41}$$

Given $\hat{\boldsymbol{\alpha}}$, the following relations hold keeping only real terms linear with the fields [62]:

$$\hat{\mathcal{O}}^2 = c^2 \left[(\hat{\mathbf{p}} - e\mathbf{A})^2 + e\hbar\,\hat{\boldsymbol{\Sigma}} \cdot \mathbf{B} \right], \tag{1.42a}$$

$$[\hat{\mathcal{O}}, [\hat{\mathcal{O}}, V(\mathbf{r})]] = -2\hbar c^2 \left(\nabla V(\mathbf{r}) \times \hat{\mathbf{p}}\right) \cdot \hat{\boldsymbol{\Sigma}} - \hbar^2 c^2 \nabla^2 V(\mathbf{r}) + \ldots, \tag{1.42b}$$

$$\hat{\mathcal{O}}^4 = c^4 (\hat{\mathbf{p}} - e\mathbf{A})^4 + \ldots, \tag{1.42c}$$

where $\mathbf{B} = \nabla \times \mathbf{A}$ and the matrices $\hat{\boldsymbol{\Sigma}}$ are equal to:

$$\hat{\Sigma}_i = \begin{pmatrix} \hat{\sigma}_i & 0 \\ 0 & \hat{\sigma}_i \end{pmatrix}, \quad i = x, y, z. \tag{1.43}$$

Finally, the FW Hamiltonian is found by substituting Eqs. (1.42) in Eq. (1.40), which becomes:

$$\begin{aligned}\hat{H}_{\mathrm{FW}} = \hat{\beta}mc^2 + V(\mathbf{r}) + \hat{\beta}\,\frac{(\hat{\mathbf{p}} - e\mathbf{A})^2}{2m} - \hat{\beta}\,\frac{(\hat{\mathbf{p}} - e\mathbf{A})^4}{8m^3c^2} + \hat{\beta}\,\frac{e\hbar}{2m}\hat{\mathbf{\Sigma}}\cdot\mathbf{B} \\ + \frac{\hbar}{4m^2c^2}\,(\nabla V(\mathbf{r}) \times \hat{\mathbf{p}})\cdot\hat{\mathbf{\Sigma}} + \frac{\hbar^2}{8m^2c^2}\nabla^2 V(\mathbf{r}) + \ldots .\end{aligned} \tag{1.44}$$

The FW Hamiltonian in Eq. (1.44) has a (4×4) block-diagonal structure, in which the upper (2×2) block describes positive energy states, while the lower block corresponds to negative energy states. Since electrons are described by positive energy states, it is sufficient to retain only the upper block. In this case, $\hat{\mathbf{\Sigma}}$ is replaced by $\hat{\boldsymbol{\sigma}}$ and $\hat{\beta}$ is set equal to 1, yielding a relativistic wavefunction in which the individual corrections to the nonrelativistic Hamiltonian are clearly disentangled. The first four terms then reproduce the nonrelativistic Hamiltonian of Eq. (1.24) in the presence of time-independent electric and magnetic fields, together with the relativistic correction to the kinetic energy, which was previously obtained via the Taylor expansion in Eq. (1.32). The fifth term corresponds to the Zeeman correction, representing the magnetic dipole energy and giving rise to the splitting of electronic states in the presence of an external magnetic field. The sixth term describes the spin-orbit interaction correction, previously introduced in Eq. (1.30), and derived here directly from the Dirac equation. The final term is the Darwin correction, which provides a significant contribution in regions where the electrostatic potential varies extremely rapidly, such as in the vicinity of nuclei, and is proportional to the charge density. In what follows, we adopt a nonrelativistic approach, treating spin-orbit coupling as a small perturbation to the Schrödinger equation. The spin-orbit correction can be recast to explicitly show its dependence on the orbital angular momentum operator $\hat{\mathbf{L}}$ and the spin angular momentum operator $\hat{\mathbf{S}}$ by considering a spherically symmetric potential:

$$\hat{\boldsymbol{\sigma}}\cdot(\nabla V(\mathbf{r}) \times \hat{\mathbf{p}}) = \frac{2}{\hbar}\frac{1}{r}\frac{\partial V}{\partial r}\left(\frac{\hbar}{2}\hat{\boldsymbol{\sigma}}\right)\cdot(\mathbf{r} \times \hat{\mathbf{p}}) = \frac{2}{\hbar}\frac{1}{r}\frac{\partial V}{\partial r}\hat{\mathbf{S}}\cdot\hat{\mathbf{L}}\,. \tag{1.45}$$

Therefore, the Eq. (1.30) becomes:

$$\hat{H}_{\mathrm{so}} = \frac{1}{2m_0^2c^2r}\frac{\partial V}{\partial r}\hat{\mathbf{S}}\cdot\hat{\mathbf{L}}\,. \tag{1.46}$$

The Eqs. (1.1) are also valid for the orbital angular momentum by substituting the spin operators $\hat{S}^2$ and $\hat{S}_{\mathrm{z}}$ with their orbital counterparts $\hat{L}^2$ and $\hat{L}_{\mathrm{z}}$, and the quantum numbers

s and m_s with the orbital quantum numbers l and m_l, respectively.

The spin-orbit term in the full Hamiltonian modifies the band structure in solids whenever electronic states possess orbital character. At the Γ point, the top valence band manifold in most common semiconductors derives from atomic p orbitals with quantum number $l = 1$, thus spin-orbit interaction directly reshapes the band structure. Because the spin-orbit term couples orbital and spin degrees of freedom, the eigenstates of the full Hamiltonian are not eigenstates of the spin and orbital operators. Instead, they are eigenstates of the total angular momentum operator $\hat{\mathbf{J}} = \hat{\mathbf{L}} + \hat{\mathbf{S}}$, satisfying relations analogous to Eqs. (1.1) upon the substitutions $\hat{S}^2 \to \hat{J}^2$, $\hat{S}_\mathrm{z} \to \hat{J}_\mathrm{z}$, $s \to j$, and $m_\mathrm{s} \to m_\mathrm{j}$. Therefore, valence band states at the Γ point are labeled by the quantum numbers j and m_j. As a result, the sixfold degeneracy of the valence band is lifted [63], splitting the band into a fourfold-degenerate $j = 3/2$ manifold, corresponding to heavy-hole (HH) band with $m_\mathrm{j} = \pm 3/2$ and light-hole (LH) band with $m_\mathrm{j} = \pm 1/2$, and a twofold-degenerate $j = 1/2$ split-off (SO) band with $m_\mathrm{j} = \pm 1/2$. Each electronic band remains at least twofold degenerate because time-reversal symmetry enforces Kramers degeneracy in a non-magnetic system. The latter implies a spin twofold degeneracy of all the bands at the time-reversal invariant momenta (TRIM), where $\mathbf{k} = -\mathbf{k} + \mathbf{K}$, and in particular at the Γ point, where $\mathbf{k} = 0$. This condition can be derived directly from Eq. (1.8). The energy separation between the $j = 3/2$ and $j = 1/2$ states is quantified by the spin-orbit splitting parameter Δ_so, whose magnitude depends strongly on the atomic number of the constituent elements. For instance, in Si the spin-orbit splitting of the valence band amounts to $\Delta_\mathrm{so}^\mathrm{Si} \simeq 0.044$ eV, whereas for semiconductors with heavy atoms can become quite large. In Ge, $\Delta_\mathrm{so}^\mathrm{Ge} \simeq 0.29$ eV, in GaAs, $\Delta_\mathrm{so}^\mathrm{GaAs} \simeq 0.32$ eV, and, in $CdGeAs_2$, $\Delta_\mathrm{so}^\mathrm{CdGeAs} \simeq 0.34$ eV. The spin-orbit splitting of the valence band manifolds plays a central role in optical orientation.

In contrast, the lowest conduction band at the Γ point typically originates from atomic s orbitals with zero orbital angular momentum, *i.e.*, $l = 0$. Therefore, spin-orbit coupling does not split the conduction band minimum which remains doubly degenerate due to Kramers degeneracy. This description accurately captures the behavior in Ge, GaAs, and $CdGeAs_2$, whereas in Si the lowest conduction band also derives from atomic p orbitals and thus exhibits spin-orbit splitting [64]. However, this splitting is very small, approximately 0.032 eV, and of limited relevance given the indirect band gap nature of Si (details about the band structure outside the Γ point are given in the next section).

Here, we have discussed the origin of the spin-orbit interaction and its role in splitting valence band manifolds at the Γ point in many semiconductors. However, its impact extends well beyond the mere splitting of energy levels. For instance, spin-orbit coupling

strongly influences both the optical and transport properties of these materials. Before addressing the details of optical orientation, we briefly present fundamental concepts of light-matter interaction and interband optical transitions, along with the band structure of Ge, Si, and GaAs. $CdGeAs_2$ will be discussed subsequently.

1.2.2. Interband optical transitions

Light-matter interaction is described here within the framework of the Fermi's golden rule (FGR), which provides an analytical expression for the transition rate W between well-defined energy levels. Within the electric dipole approximation, the FGR is given by [65]:

$$W_{\mathrm{i,f}}(\mathbf{k}) = \frac{2\pi}{\hbar}\left(\frac{qE_0}{m_0\omega}\right)^2 M_{\mathrm{i,f}}(\mathbf{k})^2\delta[E_{\mathrm{f}}(\mathbf{k}) - E_{\mathrm{i}}(\mathbf{k}) - \hbar\omega], \tag{1.47}$$

where the subscripts i and f refer to the initial and final electronic states with energies $E_{\mathrm{i}}(\mathbf{k})$ and $E_{\mathrm{f}}(\mathbf{k})$, respectively. Considering a transverse plane wave, the frequency ω and amplitude E_0 characterize the perturbation field $\mathbf{E}(t) = \mathbf{E}(\omega)e^{(-i\omega t)} + c.c.$, where $\mathbf{E}(\omega) = E_0\,\mathbf{e}$ is the polarization vector. The unit vector $\mathbf{e}$ equals $(\mathbf{e}_{\mathrm{x}} + (-)\,i\mathbf{e}_{\mathrm{y}})/\sqrt{2}$ for $\sigma^{+(-)}$ circular polarizations, where $\mathbf{e}_{\mathrm{x}}$ and $\mathbf{e}_{\mathrm{y}}$ are the unit vectors of the x and y axes in the laboratory frame, respectively. The term $M_{\mathrm{i,f}}(\mathbf{k}) = |\mathbf{e}\cdot\langle\phi_{\mathrm{f}}|\,\hat{\mathbf{p}}\,|\phi_{\mathrm{i}}\rangle|$ is the modulus of the transition matrix element of the momentum operator $\hat{\mathbf{p}} = -i\hbar\nabla$ between the initial and final states, represented by the wavefunctions $|\phi_{\mathrm{i}}\rangle$ and $|\phi_{\mathrm{f}}\rangle$, respectively.

The Dirac delta function in Eq. (1.47) implies that we have a nonzero transition rate only if the energy difference between levels equals the photon energy $\hbar\omega$. Therefore, considering light absorption, electrons from the valence band are promoted into the conduction band only if the initial and final states match this energy conservation rule. Once the condition regarding energy conservation is satisfied, the intensity of the transition depends on the matrix element of the momentum operator. The latter acts only on the spatial part of the wavefunction, leaving the spin component unchanged. Moreover, being an odd operator under inversion symmetry, $\hat{\mathbf{p}}$ leads to nonzero matrix elements only for transitions between states of opposite parity. Within the spherical harmonics expansion of energy levels, this requirement corresponds to the first dipole selection rule, which imposes $\Delta l = \pm 1$. At the Γ point, the conduction band edge often derives from s-type orbitals, which are even under inversion, while valence band edge derives from p-type orbitals, which are odd. This parity difference allows optical transitions between these bands. The corresponding dipole selection rules can then be established:

$$\Delta l = \pm 1, \quad \Delta s = 0, \quad \Delta m_{\mathrm{s}} = 0, \quad \Delta m_{\mathrm{j}} = 0, \pm 1. \tag{1.48}$$

The final selection rule in Eq. (1.48) reflects the conservation of the angular momentum, including that carried by the photon, during light absorption and thus links the allowed optical transitions to the polarization state of the light. In particular, photons of circularly polarized light carry a projection of the angular momentum along their propagation direction equal to +1 and -1 (in $\hbar$ units) for left-handed (σ^+) and right-handed (σ^-) polarizations, respectively. Consequently, the absorption of σ^+- or σ^--polarized photons transfers angular momentum to the excited carriers, leading to transitions with $\Delta m_{\mathrm{j}} = +1$ or -1. In contrast, photons of unpolarized or linearly polarized light are in a superposition of σ^+ and σ^- polarization states, thus dipole selection rules permit optical transitions with both $\Delta m_{\mathrm{j}} = 0$ and $\Delta m_{\mathrm{j}} = \pm 1$.

In crystals, the large number of available states requires integrating Eq. (1.47) over the entire first BZ to account for all possible transitions respecting energy conservation and to evaluate the total carrier-injection rate. Refined calculations of the band structure provide the base for this type of evaluations, as discussed in more detail in the following sections. In the description presented so far, we have considered optical transitions allowed by the dipole selection rules, for which the photon momentum is negligible on the scale of the BZ. As a consequence, optical transitions are vertical in $\mathbf{k}$-space, *i.e.*, they connect valence and conduction band states with the same crystal momentum and do not induce scattering across the BZ. However, the band dispersion also allows indirect optical transitions, in which electrons undergo transitions between valence and conduction bands while changing their crystal momentum. Since photon momentum is insufficient to provide the required $\Delta\mathbf{k}$, crystal momentum conservation is ensured by the absorption or emission of a phonon. Phonons are lattice excitations that carry crystal momentum and typically have energies much smaller than those of optical photons. Consequently, indirect transitions involve a two-particle process, consisting of photon absorption or emission accompanied by phonon absorption or emission. A proper treatment of indirect transitions introduces, in addition to the energy conservation delta function, an additional delta function enforcing conservation of the total crystal momentum and accounting for momentum transfer between electrons and phonons.

The band structures of Ge, Si, and GaAs near the Γ point are presented in Figs. 1.1a - 1.1c to visualize interband optical transitions in these systems. Band structures are calculated using a 30-band $\mathbf{k}\cdot\mathbf{p}$ model for Ge and GaAs, following Refs. [55], [66]. For Si, we rely on empirical pseudopotential calculations of Ref. [67]. Interband optical transitions involving

HH and LH bands can be driven by photons with energy $\hbar\omega > E_g$, where E_g is the band gap. GaAs is a direct band gap semiconductor, meaning that conduction and valence band edges are aligned both at the same electron wavevector $\mathbf{k}$, in particular at the Γ point. Its band gap is found experimentally to be $E_g^{GaAs} = 1.42\,eV$ at room temperature. Ge and Si are both indirect band gap semiconductor, with the conduction band edge located at the L point and along the Δ direction connecting the Γ and the X points of the BZ, respectively. Their band gaps are $E_g^{Ge} = 0.66\,eV$ and $E_g^{Si} = 1.12\,eV$. Therefore, upon absorption of light in the visible and near-infrared regime, an electron is excited in the conduction band, accompanied by the creation of a hole in the valence band. In Ge and Si, because of their indirect band gap nature, the absorption of a photon must be accompanied by the absorption or emission of a phonon to compensate for the variation in crystal momentum. It is worth noting that, the direct band gap energy is relatively close to the indirect one in Ge, with a value of $E_{dg}^{Ge} = 0.8\,eV$, which matches the most widely exploited window for optical telecommunications (1550 nm). Therefore, direct transitions are accessible by slightly increasing the photon energy, leading to an optical orientation process at the Γ point very similar to that observed in GaAs. If the photon energy exceeds $E_g + \Delta_{so}$, transitions involving the SO band also occur. The kinetic energy of the excited electrons in the conduction band is given by $E_k = E_1 - E_c + k_B T$, where E_1 is the energy of the final state, determined with the energy conservation rule, E_c is the energy of the conduction band edge, and $k_B T$ is the thermal energy. Therefore, at fixed $\hbar\omega$, excitations from the SO band promote electrons with lower kinetic energy compared to excitations from the HH and LH bands. This kinetic energy difference accounts for characteristic features in the photon-energy dependence of spin-dependent signals in Ge [68].

Before concluding this section, it is worth making a remark about inversion symmetry in these semiconductors. Si and Ge crystallize in the diamond cubic structure belonging to the space group $Fd\bar{3}m$ (No. 227) and are therefore centrosymmetric. In non-magnetic centrosymmetric crystals, the spin twofold degeneracy at fixed electron wavevector $\mathbf{k}$ is preserved because of the combination of time-reversal and inversion symmetries. The inversion symmetry forces:

$$E(\mathbf{k}, \uparrow) = E(-\mathbf{k}, \uparrow). \tag{1.49}$$

where E is the band energy. Therefore, combining Eq. (1.8) with Eq. (1.49) yields $E(\mathbf{k}, \uparrow) = E(\mathbf{k}, \downarrow)$ for any wavevector $\mathbf{k}$, and each electronic state remains twofold degenerate throughout the entire BZ. In contrast, GaAs adopts the zinc-blende cubic structure belonging to the space group $F\bar{4}3m$ (No. 216), which lacks inversion symmetry. In

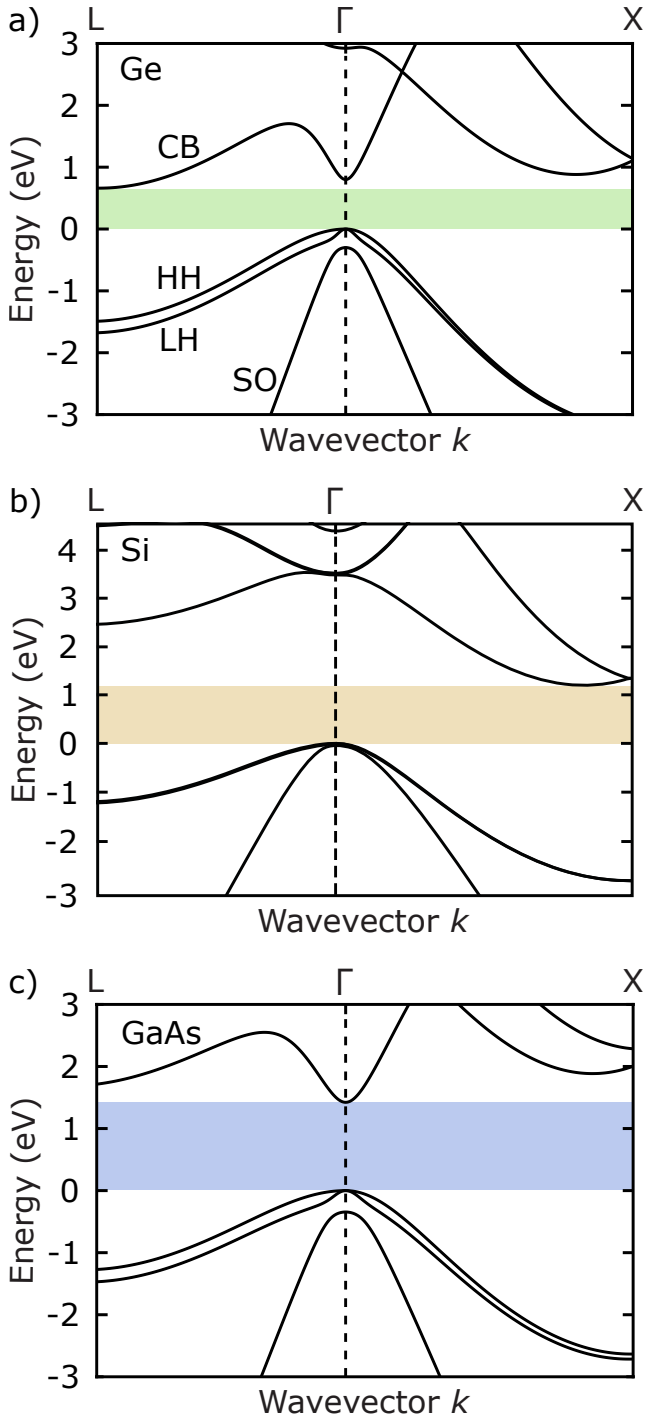

Figure 1.1: Band structures of (a) Ge, (b) Si, and (c) GaAs near the Γ point. Bands are calculated using a 30-band $\mathbf{k}\cdot\mathbf{p}$ model for Ge and GaAs, while an empirical pseudopotential model for Si. Calculations for Si are reported from Ref. [67]. The shaded colored region indicates the band gap, while the labels denote the conduction band (CB), the heavy-hole (HH), light-hole (LH), and split-off (SO) bands.

such noncentrosymmetric crystals, time-reversal symmetry alone does not enforce spin degeneracy for arbitrary wavevectors $\mathbf{k}$, except at the TRIMs. Consequently, spin-orbit coupling can lift spin degeneracy while still preserving Kramers degeneracy between states at $\mathbf{k}$ and $-\mathbf{k}$. For zinc-blende semiconductors, the bulk inversion asymmetry (BIA) effect is captured by the Dresselhaus interaction [69], [70]:

$$\hat{H}_{\mathrm{DH}} \sim \hat{\sigma}_{\mathrm{x}} k_{\mathrm{x}} \left(k_{\mathrm{y}}^2 - k_{\mathrm{z}}^2\right) + \hat{\sigma}_{\mathrm{y}} k_{\mathrm{y}} \left(k_{\mathrm{z}}^2 - k_{\mathrm{x}}^2\right) + \hat{\sigma}_{\mathrm{z}} k_{\mathrm{z}} \left(k_{\mathrm{x}}^2 - k_{\mathrm{y}}^2\right), \tag{1.50}$$

which is cubic in $\mathbf{k}$ and vanishes at the Γ point. Since this contribution was not included in the band structure calculations, the bands in Fig. 1.1c remain spin degenerate.

1.2.3. Optical orientation

Optical orientation refers to the generation of spin-polarized carriers in semiconductors through the absorption of circularly polarized light. Owing to the conservation of the angular momentum, the photo-excited electrons in the conduction band (CB) acquire a net spin polarization. The following discussion demonstrates this statement by focusing on the theoretical framework of optical orientation. The FGR and fully linear response theory are employed to quantify injection rates and spin polarization in the simpler cases of Ge and GaAs, considering only vertical transitions.

At the Γ point, when unpolarized or linearly polarized photons with energy $\hbar\omega = E_{\mathrm{g}}$ are absorbed, transitions from both HH and LH bands to the CB are allowed with $\Delta m_{\mathrm{j}} = 0, \pm 1$, according to the dipole selection rules. However, when $\sigma^{+(-)}$-polarized photons with the same energy are absorbed, the transitions are restricted to those with $\Delta m_{\mathrm{j}} = +(-)1$, respectively. In an atomic-like model, the allowed transitions for σ^+ and σ^- polarizations are depicted with the relative transition rates in Fig. 1.2. Without delving into the detailed derivation [64], [71], the transition rates from the valence bands (VBs) to the CB are:

$$W_{\mathrm{HH,CB}} \propto 1;\ W_{\mathrm{LH,CB}} \propto \frac{1}{3};$$

$$W_{\mathrm{SO,CB}} \propto \frac{2}{3}.$$

The values are normalized with respect to $W_{\mathrm{HH,CB}}$. Under σ^+ excitation ($\Delta m_{\mathrm{j}} = +1$), for every electron promoted from the LH band ($m_{\mathrm{j}} = -\frac{1}{2}$) to the CB ($m_{\mathrm{j}} = +\frac{1}{2}$), three electrons are exited from the HH band ($m_{\mathrm{j}} = -\frac{3}{2}$) to the CB ($m_{\mathrm{j}} = -\frac{1}{2}$). This leads to a spin population in the CB at the generation time with $m_{\mathrm{j}} = -\frac{1}{2}$, which cannot be obtained with unpolarized or linearly polarized light. Conversely, σ^- excitation results in a spin

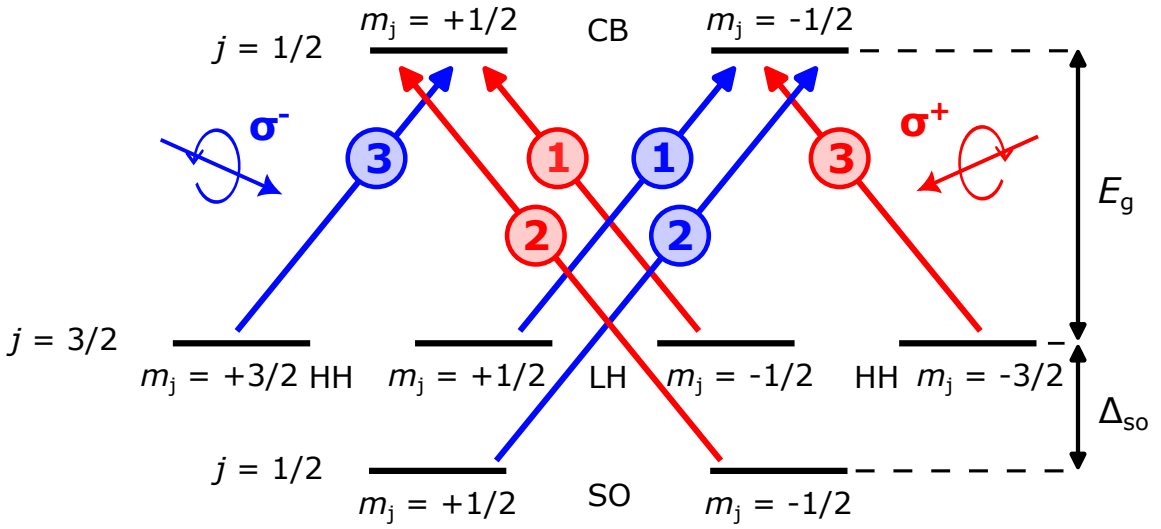

Figure 1.2: Scheme of the atomic energy levels at the Γ point in Ge and GaAs. The heavy hole (HH), light hole (LH) and split-off (SO) bands are separated by the spin-orbit splitting parameter Δ_{so}. The degenerate energy levels are labelled based on their m_{j} value. In blue and red, the allowed transitions for σ^-- and σ^+-circularly polarized light are represented, respectively. The numbers inside circles are associated to the rates of the specific transitions.

population with $m_{\mathrm{j}} = +\frac{1}{2}$. The spin population can be described by the spin polarization vector $\mathbf{P}_{\mathrm{s}}$ and the degree of spin polarization DSP, both introduced in Eq.(1.9). In cubic systems, like Ge and GaAs, $\mathbf{P}_{\mathrm{s}}$ is along the light wavevector of the impinging light [64] and its orientation fixed by the sign of the DSP. The DSP can be calculated as:

$$\mathrm{DSP} = \frac{n_\uparrow - n_\downarrow}{n_\uparrow + n_\downarrow}, \tag{1.51}$$

where $n_\uparrow$ and $n_\downarrow$ are the spin-resolved electron densities with spin-up and spin-down character, respectively. Therefore, the DSP results equal to -50% by illuminating with σ^+-polarized light with photon energy $\hbar\omega = E_{\mathrm{g}}$. This value can be calculated from the previous reported transition rates, following Eq. (1.51):

$$\sigma^+ \longrightarrow \mathrm{DSP} = \frac{\frac{1}{3} - 1}{\frac{1}{3} + 1} = -50\%.$$

Conversely, under σ^--polarized light:

$$\sigma^- \longrightarrow \mathrm{DSP} = \frac{1 - \frac{1}{3}}{1 + \frac{1}{3}} = 50\%.$$

When the photon energy increases beyond the band gap, $\hbar\omega > E_g$, and the absorption edge shifts away from the Γ point, this simplified description of optical orientation is no longer valid. In this regime, a proper account of the photon-energy dependence of the DSP requires the explicit calculation of the carrier-injection rate $\dot{n}$ and the spin-injection rate $\dot{\mathbf{S}}$. Despite this limitation, the picture at Γ correctly predicts the drop of the DSP upon excitation of electrons from the SO states. Indeed, if the photon energy satisfies $\hbar\omega \geq E_g + \Delta_{so}$, transitions driven by σ^+-polarized light from the SO band ($m_j = -\frac{1}{2}$) to the CB ($m_j = +\frac{1}{2}$) become allowed and equal numbers of electrons are injected into CB states with $m_j = \pm\frac{1}{2}$, yielding zero spin polarization. In particular, the DSP for both σ^+ and σ^- polarizations is given by:

$$\sigma^+ \longrightarrow \text{DSP} = \frac{\frac{1}{3} + \frac{2}{3} - 1}{\frac{1}{3} + \frac{2}{3} + 1} = 0\%,$$

$$\sigma^- \longrightarrow \text{DSP} = \frac{1 - \frac{1}{3} - \frac{2}{3}}{1 + \frac{1}{3} + \frac{2}{3}} = 0\%.$$

It is worth to note that, when the photon energy exceeds the onset of the SO states, all VBs are excited. In this regime, the excitation becomes effectively equivalent to that of VBs in the absence of spin–orbit coupling, and, accordingly, the optical orientation process vanishes. At this stage, we introduce the rigorous approach for calculating the DSP, based on the evaluation of $\dot{n}$ and $\dot{\mathbf{S}}$ within the fully linear response theory, and apply it to cubic systems.

Fully linear response theory

Carrier- and spin-injection rates can be calculated considering the response to a continuous wave field $\mathbf{E}(t) = \mathbf{E}(\omega)e^{-i\omega t} + \mathbf{E}^*(\omega)e^{i\omega t}$, being ω the frequency such that $\hbar\omega \geq E_g$. Within the fully linear response theory [64], [71], the spin-injection rate $\dot{\mathbf{S}}$ is proportional to the field intensity:

$$\dot{S}^a = \zeta^{abc}(\omega)E^{b*}(\omega)E^c(\omega) = \sum_b \sum_c \zeta^{abc}(\omega)E^{b*}(\omega)E^c(\omega), \tag{1.52}$$

where $\zeta^{abc}(\omega)$ is a third rank pseudotensor that accounts for spin-injection coefficients along different Cartesian coordinates, which are indicated with superscript Roman letters. These when repeated imply summation over the corresponding components, as explicate in Eq. (1.52), using the Einstein summation convention. The third-rank pseudotensor $\zeta^{abc}(\omega)$ is obtained by integrating the spin operator and a FGR-derived expression [71] over the entire first BZ, yielding in $\hbar/2$ units:

$$\zeta^{abc}(\omega) = \frac{2}{\hbar}\frac{\pi q^2}{(\hbar\omega)^2}\sum_{c,\bar{c},v}{}' \int \frac{d\mathbf{k}}{8\pi^3} S^a_{c\bar{c}}(\mathbf{k}) v^{b*}_{cv}(\mathbf{k}) v^c_{\bar{c}v}(\mathbf{k}) \times (\delta[\omega_{cv}(\mathbf{k}) - \omega] + \delta[\omega_{\bar{c}v}(\mathbf{k}) - \omega]). \tag{1.53}$$

Subscripts denote the VB (v) and the CB (c and $\bar{c}$). The prime on the summation indicates that the sum is to be done over pairs of CB states, c and $\bar{c}$, that are quasidegenerate accounting for coherent excitations. When the energy separation between different CB states is smaller than the spectral width of the laser pulse, as is the case for the spin-split states in noncentrosymmetric semiconductors such as GaAs or $CdGeAs_2$, the excitation process generates a coherent superposition of quasidegenerate states. This effect is essential to be included in Eq. (1.53) to explicitly account for the resulting coherences and to reproduce experimental observations [64]. The criterion used to define the coherences in the calculations is arbitrary; however, it must account for both the energy width of the laser pulse and thermal broadening. Accordingly, an energy interval of $\Delta E = 30\,\text{meV}$ is typically chosen. $S^a_{c\bar{c}}(\mathbf{k})$ is the matrix element of the spin operator $\hat{S}^a$ along a between the c and $\bar{c}$ states at wavevector $\mathbf{k}$: $\langle c\mathbf{k}|\hat{S}^a|\bar{c}\mathbf{k}'\rangle = S^a_{c\bar{c}}(\mathbf{k})\delta(\mathbf{k}-\mathbf{k}')$. $v^a_{c(\bar{c})v}(\mathbf{k})$ is the matrix element of the velocity operator $\hat{v}^a$ along a between the $c(\bar{c})$ and v states at wavevector $\mathbf{k}$: $\langle c(\bar{c})\mathbf{k}|\hat{v}^a|v\mathbf{k}'\rangle = v^a_{c(\bar{c})v}(\mathbf{k})\delta(\mathbf{k}-\mathbf{k}')$. The velocity operator in a crystal is $\hat{\mathbf{v}} = \nabla_{\mathbf{k}}\hat{H}/\hbar$. $\omega_{c(\bar{c})v}(\mathbf{k})$ is defined as the difference $\omega_{c(\bar{c})v}(\mathbf{k}) \triangleq \omega_{c(\bar{c})}(\mathbf{k}) - \omega_v(\mathbf{k})$, being $\hbar\omega_{c(\bar{c})}(\mathbf{k})$ and $\hbar\omega_v(\mathbf{k})$ the energies of the eigenstates $c(\bar{c})$ and v, respectively. Note that the δ functions reduce the three-dimensional integral over the full BZ volume to an integral over the BZ surface defined by the condition $\omega_{c(\bar{c})v}(\mathbf{k}) = \omega$. Moreover, in Eq. (1.53) we are assuming that, in the ground state, the VB is fully occupied while the CB is empty. The integration is nontrivial due to the complexity of the constant energy surface involved and is typically performed using the linear tetrahedron method with an adaptive mesh [64]. The calculation of $\zeta^{abc}(\omega)$ and consequently of $\dot{\mathbf{S}}$ is thus reduced to calculate the matrix elements from the electronic band structure, which can be done performing pseudopotential or $\mathbf{k}\cdot\mathbf{p}$ calculations. Using $\mathbf{k}\cdot\mathbf{p}$ calculations, the velocity operator becomes $\hat{\mathbf{v}} = \nabla_{\mathbf{k}}\hat{H}_{\mathbf{k}\cdot\mathbf{p}}/\hbar$, where $\hat{H}_{\mathbf{k}\cdot\mathbf{p}}$ is the total Hamiltonian matrix of the model [72]. The coefficients $\zeta^{abc}(\omega)$ reflect the symmetry properties of the crystal. For example, in a cubic system only a single independent coefficient of the spin-injection pseudotensor exists, namely $\zeta^{xyz}(\omega)$, which is purely imaginary. The other nonzero coefficients are given by: $\zeta^{yzx}(\omega) = \zeta^{zxy}(\omega) = \zeta^{xyz}(\omega) = -\zeta^{xzy}(\omega) = -\zeta^{zyx}(\omega) = -\zeta^{yxz}(\omega)$. In the cubic case, the cartesian coordinates define a coordinate system aligned with the crystallographic directions [100], [010], and [001].

Although $\dot{\mathbf{S}}$ is useful for quantifying the total spin injected into the CB, it does not distinguish between two different situations: one involving a large number of weakly polarized electrons and the other involving a small number of highly polarized electrons. To distinguish these two distinct cases, the DSP is introduced to quantify the average electron spin polarization and defined as the spin-injection rate component $\dot{S}^a$ normalized to the carrier-injection rate $\dot{n}$:

$$\mathrm{DSP}^a = \frac{\dot{S}^a}{\dot{n}}. \tag{1.54}$$

In the fully linear response theory, the carrier-injection rate $\dot{n}$ is also proportional to the field intensity:

$$\dot{n} = \xi^{ab}(\omega) E^{a*}(\omega) E^b(\omega), \tag{1.55}$$

where $\xi^{ab}(\omega)$ is the tensor:

$$\xi^{ab}(\omega) = \frac{2\pi q^2}{(\hbar\omega)^2} \sum_{c,v} \int \frac{d\mathbf{k}}{8\pi^3} v_{cv}^{a*}(\mathbf{k}) v_{cv}^{b}(\mathbf{k}) \times \delta[\omega_{cv}(\mathbf{k}) - \omega]. \tag{1.56}$$

The carrier-injection rate $\dot{n}$ can be related to the absorption coefficient of the material via [67]:

$$\alpha = \frac{\hbar\omega}{2\upsilon c\varepsilon_0} \frac{\dot{n}}{|E_0|^2}, \tag{1.57}$$

where c is the speed of light, υ the real part of the refractive index, ε_0 the vacuum permittivity, and $|E_0|^2$ the field intensity. In cubic systems, there is only a unique coefficient of the carrier-injection tensor, namely $\xi^{xx}(\omega)$, which is purely real and related to the material susceptibility through $\mathrm{Im}[\chi(\omega)] = [\hbar/(2\varepsilon_0)]\, \xi^{xx}(\omega)$ [71]. The other nonzero coefficients are given by: $\xi^{yy}(\omega) = \xi^{zz}(\omega) = \xi^{xx}(\omega)$.

We now consider the absorption of σ^+-polarized light propagating along the z axis, with electric field $\mathbf{E}(\omega) = E_0(\mathbf{e}_\mathrm{x} + i\mathbf{e}_\mathrm{y})/\sqrt{2}$. Using Eq. (1.52), the spin-injection rate $\dot{\mathbf{S}}$ is calculated as (0, 0, $\dot{S}^z$) with $\dot{S}^z = i\zeta^{xyz}(\omega)|E_0|^2$. Therefore, spin-polarized electrons injected into the CB are fully polarized along the z axis, that is the direction of the light wavevector $\mathbf{k}_\mathrm{l}$. The alignment of $\dot{\mathbf{S}}$ with $\mathbf{k}_\mathrm{l}$, derived here for light propagating along the z axis, holds generally in cubic systems and is independent of the wavevector orientation with respect to the crystallographic axes [64]. Using Eqs. (1.54) and (1.55), the carrier-

injection rate is calculated as $\dot{n} = \xi^{xx}(\omega)|E_0|^2$ and the absorption coefficient is given by $\alpha = \hbar\omega\,\xi^{xx}(\omega)/(2\upsilon c\varepsilon_0)$. Consequently, the degree of spin polarization then results $\mathrm{DSP}^z = -\mathrm{Im}[\zeta^{xyz}(\omega)]/\xi^{xx}(\omega)$. Contrary, under σ^--polarized light propagating along the z axis with $\mathbf{E}(\omega) = E_0(\mathbf{e}_\mathrm{x} - i\mathbf{e}_\mathrm{y})/\sqrt{2}$, the spin-injection rate has the opposite sign, while the carrier-injection rate remains unchanged. Hence, reversing the circular polarization results only in a sign change of the DSP.

Calculated $\xi^{xx}(\omega)$ and $\mathrm{Im}[\zeta^{xyz}(\omega)]$ for Ge are presented as functions of the photon energy in Figs. 1.3a - 1.3d. Above 0.8 eV, corresponding to the band gap at the Γ point, both $\xi^{xx}(\omega)$ (Fig. 1.3a) and $\mathrm{Im}[\zeta^{xyz}(\omega)]$ (Fig. 1.3c) begin to increase due to optical absorption from both HH and LH states. The decomposition into individual valence band contributions (Figs. 1.3b and 1.3d) shows that HH and LH states contribute to spin injection with the same sign, each yielding a 50% contribution to the polarization. This behavior is not captured by the simplified picture of optical orientation discussed earlier, which correctly estimates the total DSP but fails to predict the sign of the individual contributions. As the photon energy is increased beyond 1.1 eV, $\mathrm{Im}[\zeta^{xyz}(\omega)]$ decreases as a result of both a reduction in the LH contribution and the onset of absorption from the SO band, which provides an opposite contribution to spin injection. The calculations also reveal a sharp increase in both $\xi^{xx}(\omega)$ and $\mathrm{Im}[\zeta^{xyz}(\omega)]$ at photon energies around 2.2 eV, corresponding to the direct band gap at the L point of the BZ. This increase arises only from transitions involving the HH band, which is no longer degenerate with the LH band away from the Γ point. Immediately above this energy, $\xi^{xx}(\omega)$ remains large due to strong absorption in regions along the Γ–L direction while $\mathrm{Im}[\zeta^{xyz}(\omega)]$ decreases rapidly due to excitations from LH states that contribute with opposite sign to spin injection.

Fig. 1.4 presents the calculated DSP spectrum for Ge illuminated by σ^--polarized light, along with the one for GaAs adapted from Ref. [64]. In both cases, the spin polarization reaches values of up to 50% at the absorption edge, where only HH and LH states at the Γ point contribute. The smaller band gap of Ge accounts for the earlier onset in the spectrum. In both semiconductors, the DSP remains above 40% as the photon energy increases over a range comparable to the spin–orbit splitting of the VB (290 meV for Ge and 320 meV for GaAs). Upon further increasing, the DSP decreases to values below 10% due to the combined effect of absorption from the SO band and a reduction in the polarization contribution from the LH states.

The framework described so far can be extended to evaluate the DSP in Si, which likewise crystallizes in a diamond structure, by considering optical absorption across the direct band gap [64]. Nevertheless, the direct band gap of Si is approximately 4.17 eV, which implies that photon energies in the ultraviolet range are required to induce direct

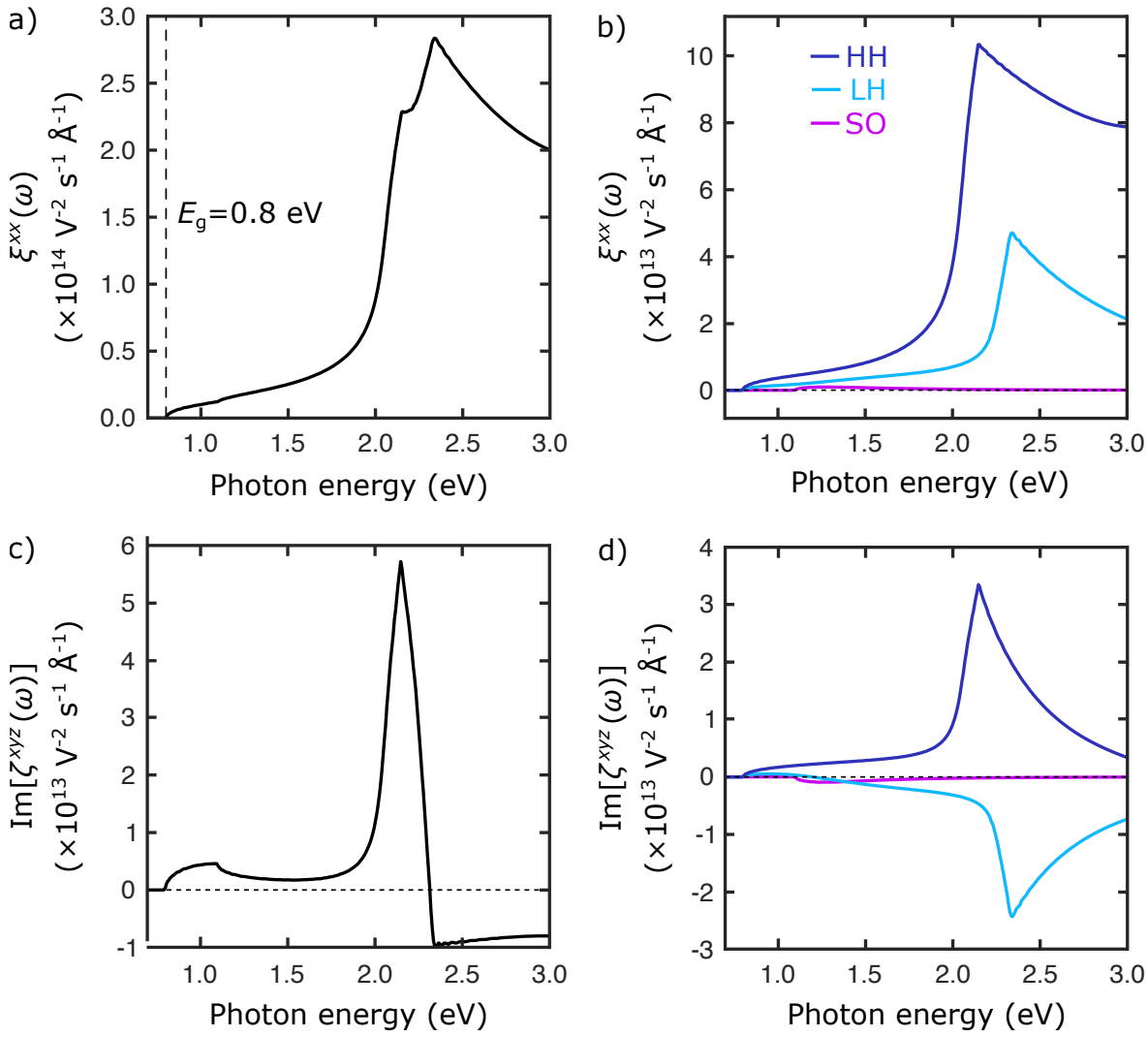

Figure 1.3: (a) The coefficient $\xi^{xx}(\omega)$ of the carrier-injection tensor calculated for Ge above the band gap E_g. (b) Decomposition of $\xi^{xx}(\omega)$ in single contributions from HH, LH and SO bands. (c) The imaginary part of the coefficient $\zeta^{xyz}(\omega)$ of the spin-injection pseudotensor calculated for Ge. (d) Decomposition of Im$[\zeta^{xyz}(\omega)]$ in single contributions from HH, LH and SO bands.

optical transitions. Such wavelengths are of limited relevance for semiconductor optoelectronics and telecommunications, which are primarily focused on the telecommunication window around 1550 nm ($\simeq$ 0.8 eV). Moreover, electrons optically injected through direct transitions rapidly scatter away from the Γ point via nonradiative processes that do not preserve spin [73], making the investigation of spin-transport properties particularly challenging.

The situation in Si becomes considerably more interesting when a nonequilibrium spin population is generated via phonon-assisted indirect optical transitions. Because the

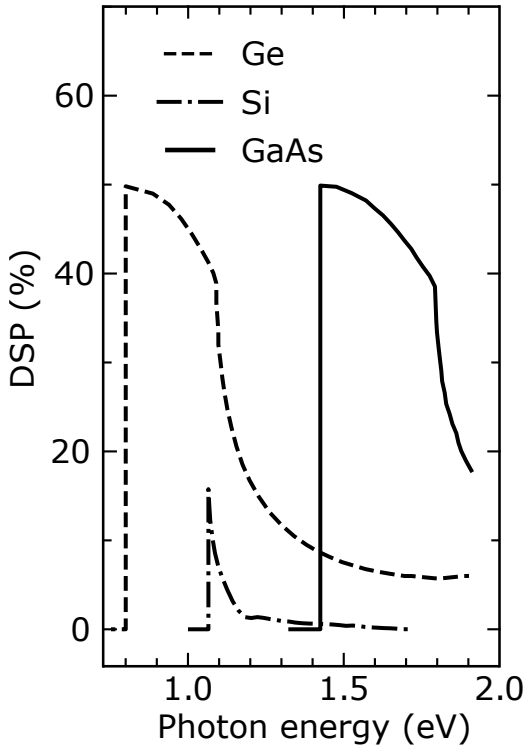

Figure 1.4: (a) The photon-energy dependence of the degree of spin polarization (DSP) for Ge (dashed), Si (dashed and dotted), and GaAs (solid) illuminated by σ^--polarized light. The GaAs and Si spectra are adapted from Refs. [64], [67], respectively.

indirect band gap along the Δ direction is 1.12 eV, lower photon energies in the near-infrared and visible range can drive these excitations, making them more attractive for technological applications. In addition, spin-polarized electrons oriented across the Δ valleys tend to exhibit longer lifetimes, as they are less susceptible to spin-flip processes induced by phonon and impurity scattering. Cheng *et al.* performed a full band-structure calculation using an empirical pseudopotential model to evaluate the indirect carrier- and spin-injection rates mediated by all relevant phonon branches throughout the entire BZ, accounting for contributions from each VB and all six Δ valleys in the CB [67]. This approach allows the calculation of the DSP above the indirect band gap onset, as presented in Fig. 1.4. In this case, the maximum DSP reaches 15% at the onset of the spectrum. Notably, this occurs below the indirect band gap energy because the calculation includes phonon-assisted processes in which a photon is absorbed simultaneously with the emission of a phonon. Therefore, the phonon energy effectively lowers the threshold photon energy required for the transition.

These considerations on the DSP in cubic systems, derived within the fully linear response theory, conclude the present discussion. In the next section, $CdGeAs_2$ is introduced, and

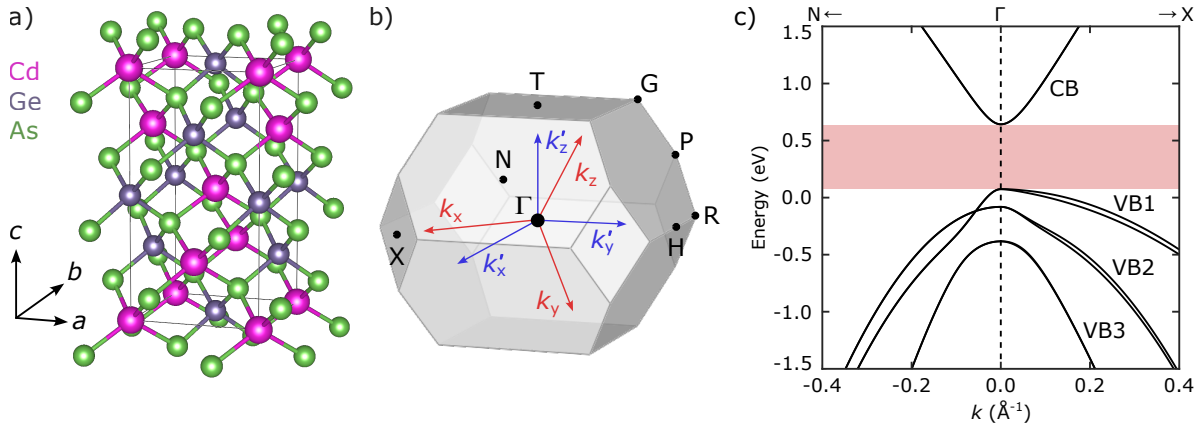

Figure 1.5: (a) Crystal system of $CdGeAs_2$. The conventional tetragonal unit cell is traced by black lines. (b) First bulk Brillouin zone. Labels indicate the high-symmetry points and the coordinate systems (k_x, k_y, k_z) used in the ARPES measurements of Sec. 3.3 (red), as well as (k'_x, k'_y, k'_z) corresponding to the reciprocal a^*, b^*, and c^* axes, respectively (blue). (c) Band structure near the band gap at the Γ point calculated with the 8-band $\mathbf{k}\cdot\mathbf{p}$ model.

the equations presented here are applied to discuss optical orientation in this chalcopyrite semiconductor.

1.2.4. $CdGeAs_2$

$CdGeAs_2$ is a chalcopyrite ternary compound of the family ABC_2. Atoms are arranged in a body-centered tetragonal crystal system belonging to the noncentrosymmetric space group $I\bar{4}2d$ (No. 122). The lattice parameters are $a = 5.94$ Å and $c = 11.21$ Å, corresponding to a tetragonal distortion $c/a = 1.89$ [74]. $CdGeAs_2$ consists of alternating As and Cd-Ge layers along the [100] and [001] directions of the conventional cell. The latter contains four formula units and is presented in Fig. 1.5a. It is defined by two equal in-plane lattice vectors, **a** and **b**, lying in the basal ab plane, and a third lattice vector, **c**, perpendicular to this plane. Accordingly, the cell has a square base and is elongated along the c axis (the [001] direction). Cd and Ge occupy sites along the fourfold axis, while As lies on the twofold axis. Atoms are covalently bonded like in diamond, adopting an sp^3 hybridization and tetrahedral coordination. Each Cd and Ge atom is bonded to four As atoms, and each As atom is coordinated by two Cd and two Ge cations. Due to the different bond lengths between the As anion and the Cd and Ge cations, the As anion is displaced from the ideal zinc-blende site at the center of the tetrahedron by $\delta u = 0.21$ Å [75].

In reciprocal space, the periodicity is described in terms of the body-centered tetragonal

primitive cell, which has half the volume of the conventional cell (two formula units). The corresponding primitive lattice vectors are $\mathbf{a}_1 = (a/2, -a/2, c/2)$, $\mathbf{a}_2 = (a/2, a/2, c/2)$, and $\mathbf{a}_3 = (-a/2, -a/2, c/2)$. The associated first Brillouin zone (BZ) is shown in Fig. 1.5b, where the high-symmetry points (Γ, G, N, P, R, H, T, X) are indicated along with the coordinate systems (k_x, k_y, k_z) and (k'_x, k'_y, k'_z). The former coincides with the directions investigated in the ARPES measurements of Sec. 3.3: k_y and k_z are parallel to low-symmetry axes, whereas k_x is parallel to the ΓX axis. The latter corresponds to the coordinate system aligned with the reciprocal a^*, b^*, and c^* axes, which lie along the ΓH and ΓT directions, respectively. Using as basis vectors $\mathbf{k}'_\mathrm{x}$, $\mathbf{k}'_\mathrm{y}$, and $\mathbf{k}'_\mathrm{z}$, the unit vectors of the coordinate systems are:

$$\mathbf{k}'_\mathrm{x} = (1,0,0)\,, \quad \mathbf{k}'_\mathrm{y} = (0,1,0)\,, \quad \mathbf{k}'_\mathrm{z} = (0,0,1)\,,$$

$$\mathbf{k}_\mathrm{x} = \left(\frac{1}{\sqrt{2}}, -\frac{1}{\sqrt{2}}, 0\right), \quad \mathbf{k}_\mathrm{y} = \frac{1}{\gamma}\,(a, a, -c)\,, \quad \mathbf{k}_\mathrm{z} = \frac{1}{\gamma}\left(\frac{c}{\sqrt{2}}, \frac{c}{\sqrt{2}}, \frac{2a}{\sqrt{2}}\right),$$

where $\gamma = \sqrt{2a^2 + c^2}$.

Many of the characteristic properties of chalcopyrites arise from the coexistence of electronic bands with markedly different effective masses and that can exhibit nearly linear dispersion and high carrier mobilities. This behavior is captured by the Kildal $\mathbf{k}\cdot\mathbf{p}$ model [76], *i.e.*, an extension of the Kane Hamiltonian [56] that incorporates the anisotropic crystal field present in tetragonal semiconductors to describe the low-energy states near $\mathbf{k} = 0$. In the Kildal model, spin-orbit interaction and anisotropic crystal potential induced by tetragonal distortion are treated as independent perturbations. The full Hamiltonian is:

$$\hat{H} = \hat{H}_0 + \hat{H}', \tag{1.58a}$$

$$\hat{H}_0 = \frac{\hat{\mathbf{p}}^2}{2m_0} + V_0, \tag{1.58b}$$

$$\hat{H}' = V_\mathrm{cr} + \frac{\hbar}{m_0}\mathbf{k}\cdot\hat{\mathbf{p}} + \frac{\hbar^2\mathbf{k}^2}{2m_0} + \frac{\hbar}{4m_0^2c^2}(\nabla V_0 \times \hat{\mathbf{p}})\cdot\hat{\boldsymbol{\sigma}}. \tag{1.58c}$$

Here, $\hat{H}_0$ is the unperturbed Hamiltonian for an electron in a periodic potential V_0 with cubic symmetry, whereas $\hat{H}'$ is the perturbative Hamiltonian where V_cr is the anisotropic crystal potential. The second and third terms represent, respectively, the $\mathbf{k}\cdot\hat{\mathbf{p}}$ coupling and the free-electron kinetic contribution $\hbar^2\mathbf{k}^2/(2m_0)$, and arise from expanding $\left(\hat{\mathbf{p}}+\hbar\mathbf{k}\right)^2$ in Eq. (1.28). The last term corresponds to the spin-orbit interaction, in which the

Table 1.1: The basis functions and eigenstates at the Γ point for the three valence bands (VB1, VB2, VB3) and conduction band (CB) in the Kildal model [76]. The S wavefunction has symmetry properties of atomic s orbital; whereas the X, Y, and Z wavefunctions have symmetry properties of atomic p_{x}, p_{y}, and p_{z} orbitals, respectively. The bands are ordered from the higher to the lower in energy.

Band	Basis function	Eigenstate at the Γ point	m_{j}
CB	$\lvert iS\downarrow\rangle$	$\lvert iS\downarrow\rangle$	$-1/2$
	$\lvert iS\uparrow\rangle$	$\lvert iS\uparrow\rangle$	$+1/2$
VB1	$\lvert\frac{1}{\sqrt{2}}(X-iY)\uparrow\rangle$	$A\left(B\lvert\frac{1}{\sqrt{2}}(X-iY)\uparrow\rangle+\lvert Z\downarrow\rangle\right)$	$-1/2$
	$\lvert-\frac{1}{\sqrt{2}}(X+iY)\downarrow\rangle$	$A\left(B\lvert-\frac{1}{\sqrt{2}}(X+iY)\downarrow\rangle+\lvert Z\uparrow\rangle\right)$	$+1/2$
VB2	$\lvert Z\downarrow\rangle$	$\lvert\frac{1}{\sqrt{2}}(X+iY)\uparrow\rangle$	$+3/2$
	$\lvert Z\uparrow\rangle$	$\lvert\frac{1}{\sqrt{2}}(X-iY)\downarrow\rangle$	$-3/2$
VB3	$\lvert\frac{1}{\sqrt{2}}(X+iY)\uparrow\rangle$	$C\left(D\lvert\frac{1}{\sqrt{2}}(X-iY)\uparrow\rangle+\lvert Z\downarrow\rangle\right)$	$-1/2$
	$\lvert\frac{1}{\sqrt{2}}(X-iY)\downarrow\rangle$	$C\left(D\lvert-\frac{1}{\sqrt{2}}(X+iY)\downarrow\rangle+\lvert Z\uparrow\rangle\right)$	$+1/2$

where $A=\left[1+\frac{1}{2}(\frac{2\Delta_{\mathrm{so}}}{2\Delta_{\mathrm{so}}+3E_1})\right]^{-\frac{1}{2}}$, $B=\frac{\sqrt{2}\Delta_{\mathrm{so}}}{3E_1+2\Delta_{\mathrm{so}}}$, $C=\left[1+\frac{1}{2}(\frac{2\Delta_{\mathrm{so}}}{2\Delta_{\mathrm{so}}+3E_2})\right]^{-\frac{1}{2}}$, and $D=\frac{\sqrt{2}\Delta_{\mathrm{so}}}{3E_2+2\Delta_{\mathrm{so}}}$.

contribution of the anisotropic crystal potential is neglected. A set of eight wavefunctions (Table 1.1), which are eigenstates of $\hat{H}_0$ at the Γ point, is adopted as a basis [56]. These states have the symmetry properties of atomic s and p orbitals to describe the CB and VB, respectively, yielding an 8×8 Hamiltonian matrix. The limitation to these eight wavefunctions, by neglecting bands higher and lower in energy, is reliable in $CdGeAs_2$ as the energy separation for $\mathbf{k}=0$ between the neglected bands and those considered is significantly larger than the band gap [76].

The complete matrix, for which I remand to Ref. [76], contains the spin-orbit Δ_{so} and the crystal-field δ splitting parameters. After diagonalizing the matrix, the eigenstates and eigenvalues valid for small electron wavevectors outside the Γ point are determined. The eigenstates at the Γ point are reported in Table 1.1 along with the corresponding quantum number m_{j} evaluated using spherical harmonics expansion. The model predicts parabolic energy bands with longitudinal (parallel to the c axis) and transverse (orthogonal to the c axis) effective masses. In $CdGeAs_2$, they vary significantly among the bands (Table 1.2), attaining low values that reflect the presence of highly dispersive states. Moreover, the CB remains twofold degenerate since it is described by s-type states, which have spherical

symmetry and zero orbital angular momentum. As a result, it is unaffected by anisotropic crystal field and spin-orbit coupling corrections. The VB, which is sixfold degenerate in the unperturbed problem, splits into three twofold degenerate levels. The energy splitting for $\mathbf{k} = 0$ are:

$$E_{1(2)} = -\frac{1}{2}(\Delta_{\mathrm{so}} + \delta) \, {}^{+}_{(-)} \, \frac{1}{2}\sqrt{(\Delta_{\mathrm{so}} + \delta)^2 - \frac{8}{3}\Delta_{\mathrm{so}}\delta} \tag{1.59}$$

The anisotropic crystal field produced by the tetragonal distortion lifts the degeneracy of VBs that would otherwise be degenerate in a cubic crystal. Indeed, the energy splitting E_1 obtained from Eq. (1.59) is different from zero only if $\delta \neq 0$. Therefore, the HH and LH are no longer degenerate as in cubic semiconductors, and this effect can be exploited to generate photoelectrons with very high spin polarization, approaching 100%, by means of optical orientation. The Eq. (1.59) also describes the energy splitting for $\mathbf{k} = 0$ of VBs due to spin-orbit interaction in cubic semiconductors imposing $\delta = 0$. This yields $E_1 = 0$ and $E_2 = -\Delta_{\mathrm{so}}$, so that the HH and LH remain degenerate, while the SO separates from them towards negative energies by the spin–orbit splitting parameter. Moreover, it is worth noting that Eq. (1.59) without spin-orbit coupling leads to $E_1 = 0$ and $E_2 = -\delta$, therefore the VB splits in a twofold degenerate level (singlet) and a fourfold degenerate level (doublet). The singlet lays above the doublet if $\delta < 0$ [77].

$CdGeAs_2$ is a direct band gap semiconductor with the VB maximum and the CB minimum at the Γ point. Its band gap and energy splitting are known from electroreflectance measurements: $E_{\mathrm{g}} = 0.57\,\mathrm{eV}$, $E_1 = 0.16\,\mathrm{eV}$, and $E_2 = -0.29\,\mathrm{eV}$ [78]. These results, combined with Eq. (1.59), provide a direct estimate of $\Delta_{\mathrm{so}}^{\mathrm{CdGeAs_2}} = 0.34\,\mathrm{eV}$ and $\delta = -0.21\,\mathrm{eV}$. These values are further confirmed by first-principles calculations performed within the local density approximation [77]. Its strong spin–orbit coupling makes $CdGeAs_2$ of interest for spintronics, by leading to a large spin Hall angle through extrinsic and intrinsic spin-charge interconversion mechanisms. The parameters A, B, C, and D, used to express the wavefunctions at the Γ point (Table. 1.1), can be estimated from E_1, E_2, and Δ_{so}, yielding $A \simeq 0.9238$, $B \simeq 0.4145$, $C \simeq 0.3675$, and $D \simeq -2.5307$.

Fig. 1.5c presents calculations of the electronic structure near the band gap of $CdGeAs_2$ along the ΓX and ΓN high-symmetry directions, obtained from the Kildal model combined with the Limpijumnong and Lambrecht valence-band model [77]. The latter provides an accurate description of the VB in $CdGeAs_2$ by employing a 6×6 Hamiltonian matrix constructed following the theory of invariants [79] for chalcopyrites semiconductors. Moreover, they estimate effective masses (Table 1.2) by performing parabolic fits to first-principles calculated bands in a region around the Γ point with $k \leq 0.04\ 2\pi/a$.

Table 1.2: Effective masses evaluated along the ΓX and ΓT directions for the valence bands (VB1, VB2, VB3) and conduction band (CB) in $CdGeAs_2$. References: (1) Kildal [76]; (2) Limpijumnong and Lambrecht [77].

Band	$m^*_{\Gamma X}$ $[m_0]$	$m^*_{\Gamma T}$ $[m_0]$	Ref. (see caption)
CB	0.039	0.030	1
	0.080	0.067	2
VB1	0.640	0.035	1
	0.290	0.078	2
VB2	0.079	-	1
	0.128	0.351	2
VB3	0.140	0.540	1
	0.141	0.219	2

Their results further confirm the strongly dispersing character of the bands. By merging the two approaches, we obtain an 8-band $\mathbf{k}\cdot\mathbf{p}$ model with a full Hamiltonian matrix:

$$\hat{H} = \begin{pmatrix} E_\mathrm{s} & 0 & iPk_\mathrm{x} & iPk_\mathrm{y} & iPk_\mathrm{z} & 0 & 0 & 0 \\ & E_\mathrm{s} & 0 & 0 & 0 & iPk_\mathrm{x} & iPk_\mathrm{y} & iPk_\mathrm{z} \\ & & d_1 & -i\Delta_\mathrm{so}^{\parallel} & e_1 & 0 & 0 & \Delta_\mathrm{so}^{\perp} \\ & & & d_2 & e_2 & 0 & 0 & -i\Delta_\mathrm{so}^{\perp} \\ & & & & d_3 & -\Delta_\mathrm{so}^{\perp} & i\Delta_\mathrm{so}^{\perp} & 0 \\ & & & & & d_1 & i\Delta_\mathrm{so}^{\parallel} & e_1 \\ & & & & & & d_2 & e_2 \\ & & & & & & & d_3 \end{pmatrix},$$

with:

$$\begin{aligned} d_1 &= (A_0 + A_2)k_\mathrm{x}^2 + B_0 k_\mathrm{y}^2 + (B_0 + B_1 + A_1)k_\mathrm{z}^2 + \delta, \\ d_2 &= (A_0 + A_2)k_\mathrm{y}^2 + B_0 k_\mathrm{x}^2 + (B_0 + B_1 + A_1)k_\mathrm{z}^2 + \delta, \\ d_3 &= (A_0 + A_1)k_\mathrm{z}^2 + (B_0 + A_2)(k_\mathrm{x}^2 + k_\mathrm{y}^2), \\ e_1 &= C_0 k_\mathrm{x} k_\mathrm{z} + iDk_\mathrm{y}, \\ e_2 &= C_0 k_\mathrm{y} k_\mathrm{z} - iDk_\mathrm{x}. \end{aligned}$$

The adopted notation indicates that the lower-triangular part of the matrix is given by the Hermitian conjugate of the upper-triangular part. The anisotropy of the spin-orbit interaction in a tetragonal system is now explicitly considered, describing SOC with two separated spin-orbit splitting parameters, $\Delta_\mathrm{so}^{\parallel}$ and $\Delta_\mathrm{so}^{\perp}$. The parameter E_s corresponds to the conduction-band eigenvalue of $\hat{H}_0$ for $\mathbf{k} = 0$. The parameters P, D, and A_i, B_i, C_0

Table 1.3: Parameters employed in the 8-band $\mathbf{k}\cdot\mathbf{p}$ model. Note that another parameter, C_1, is set to zero following Ref. [77].

Description	Parameter	Value
CB eigenvalue at $\mathbf{k}=0$	E_s	0.642 eV
Crystal-field splitting parameter	δ	-0.195 eV
Spin-orbit splitting parameters	$\Delta_{so}^{\parallel}$	0.114 eV
	$\Delta_{so}^{\perp}$	0.119 eV
Linear coupling terms	P	6.840 eV· Å
	D	0.252 eV· Å
Quadratic coupling terms	A_0	-17.533 eV· Å^2
	A_1	-2.523 eV· Å^2
	A_2	-0.704 eV· Å^2
	B_0	-6.238 eV· Å^2
	B_1	-6.764 eV· Å^2
	C_0	-18.610 eV· Å^2

represent coupling terms that are linear and quadratic in $\mathbf{k}$, respectively. The parameter P describes the interband coupling between the conduction and valence bands [76]. The parameters D, A_i, B_i, and C_0 are relativistic coupling terms associated with spin–orbit interaction and arise from the invariant theory used to construct the 6×6 Hamiltonian matrix in Ref. [77]. The parameter's values (Table 1.3) are adjusted from Refs. [76], [77] to account for both earlier reports and the ARPES measurements presented in Sec. 3.3. In the full Hamiltonian matrix, the free-electron kinetic energy is excluded and added a posterior to the calculated eigenvalues. The basis functions used in the 8-band $\mathbf{k}\cdot\mathbf{p}$ model are the conduction-band states $|S\uparrow\rangle$, $|S\downarrow\rangle$, and the valence-band states $|X\uparrow\rangle$, $|Y\uparrow\rangle$, $|Z\uparrow\rangle$, $|X\downarrow\rangle$, $|Y\downarrow\rangle$, $|Z\downarrow\rangle$.

The zero on the energy axis in Fig. 1.5c corresponds to the VB maximum of the unperturbed system. After including the SOC and the anisotropic crystal field, the VB maximum is given by the eigenvalues of the full Hamiltonian matrix for $\mathbf{k}=0$, and shifts to 0.071 eV. The CB minimum results equal to E_s, thus the calculated band gap is 0.571 eV. The VB splittings at the Γ point, extracted from the remaining eigenvalues, are $E_1 = 0.149$ eV and $E_2 = 0.305$ eV. These values are in very good agreement with experiments [78]. Electronic states with markedly different energy dispersions and spin degeneracy are obtained outside the Γ point. Along ΓX, the highest valence band, labeled VB1, is flatter than the intermediate valence band, VB2. This is consistent with VB1 having a larger effective mass than VB2, as reported in Table 1.2. Moreover, the spin

degeneracy of VB1 and VB2 is lifted and each band splits into two distinct states as a consequence of the noncentrosymmetric crystal structure, which breaks inversion symmetry. This is already reported in Ref. [77] where the effect is ascribed to the D parameter. Along ΓN, the situation is reversed and the two bands intersect without lifting the degeneracy. The band crossing between VB1 and VB2 is permitted as the bands belong to different irreducible representation, Γ_7 and Γ_6 in double group notation [77], respectively. Along this direction as well, the spin degeneracy is expected to be lifted outside the Γ point. The model does not accurately capture this behavior, likely because it includes only linear and quadratic terms in $\mathbf{k}$, neglecting higher-order relativistic coupling terms. Remarkably, the lowest valence band, VB3, and the CB exhibit nearly linear dispersion in both directions with negligible anisotropy.

This concludes the introduction regarding $CdGeAs_2$. The 8-band $\mathbf{k}\cdot\mathbf{p}$ model, proposed here to calculate the electronic structure around the band gap, will be used in Ch. 3 to evaluate the spin-injection rate $\dot{\mathbf{S}}$, the carrier-injection rate $\dot{n}$, and the DSP in the CB as functions of the photon energy, providing a quantitative description of optical orientation in $CdGeAs_2$. In the next section, spin–charge interconversion mechanisms in bulk materials are introduced, together with their microscopic origins, as they are exploited to detect optically injected spin currents.

1.2.5. Spin-charge interconversion

Spin-charge interconversion (SCI) refers to SOC-related processes in which a spin current generates a charge current, or vice versa. These effects are fundamental to spintronics, serving as standard mechanisms for both generating and detecting spin currents.

Among SCI phenomena, the spin Hall effect (SHE) is a bulk phenomenon that converts a charge current density $\mathbf{j}$ into a transverse spin current density $\mathbf{j}_\mathrm{s}$. The latter is also perpendicular to the unit vector of the spin polarization $\mathbf{u}_\mathrm{s}$. The SHE is described by the following phenomenological equation:

$$\mathbf{j}_\mathrm{s} = \gamma_\mathrm{sc}\,\mathbf{j}\times\mathbf{u}_\mathrm{s}, \tag{1.60}$$

where γ_sc is the spin Hall angle, a dimensionless parameter that quantifies the spin-charge interconversion efficiency. This parameter is often written as the ratio of the spin Hall conductivity $\sigma_\mathrm{SH} = \gamma_\mathrm{sc}\,\sigma_\mathrm{c}$, to the electrical conductivity σ_c, and is proportional to the strength of the spin–orbit interaction. In non-magnetic systems, no net spin polarization exists at equilibrium. When a longitudinal charge current $\mathbf{j}$ is driven in an unpolarized regime,

spin-dependent deflection does not induce a transverse charge current, since the opposite contributions from the two spin characters cancel out. Instead, the SHE generates a transverse pure spin current $\mathbf{j}_\mathrm{s}$ and a spatially separated spin accumulation, with opposite spin polarizations at opposite edges of the sample. This nonequilibrium spin accumulation is not directly detectable with conventional charge-based measurement techniques. However, the resulting spin-related effects can be exploited at material interfaces and the pure spin current can be converted into an electrical signal via spin-to-charge conversion processes, as the inverse spin Hall effect (ISHE).

The ISHE is the temporal inverse of the SHE. In this case, a charge current density is produced when a spin current density flows:

$$\mathbf{j} = \gamma_\mathrm{sc}\, \mathbf{j}_\mathrm{s} \times \mathbf{u}_\mathrm{s}. \tag{1.61}$$

Since opposite spin polarizations are redirected in contrary directions in the material through which the spin current density passes, the outcome is a lateral charge accumulation. The Eq. (1.61) can also be stated in terms of the electromotive field $\mathbf{E}_\mathrm{ISHE}$ that generates the charge accumulation:

$$\mathbf{E}_\mathrm{ISHE} = \frac{\gamma_\mathrm{sc}}{\sigma_\mathrm{c}} \mathbf{j}_\mathrm{s} \times \mathbf{u}_\mathrm{s}. \tag{1.62}$$

The origin of ISHE is dated back to 1971, when Dyakonov and Perel's innovative studies first highlighted the potential to produce a charge accumulation from a spin current [16]. Bakun et al. empirically confirmed this effect in 1984 [30]. The ISHE is suitable for spin current measurements in materials where γ_sc is large, as in Ta, W, and Pt. In contrast, the detection of ISHE in semiconductors is more difficult due to the lower SOC. For instance, $\gamma_\mathrm{sc} \simeq 0.1$ in Pt [80]–[84], whereas in semiconductors it is approximately $10^{-4} - 10^{-2}$ [85]–[88]. A measurement can be carried by electrically probing the voltage drop ΔV_ISHE between two contacts in touch with the edges of the detector, in an open circuit condition. The Eq. (1.62) can be coupled to $\Delta V_\mathrm{ISHE} = E_\mathrm{ISHE}\, d$, where d is the distance between the electrodes and E_ISHE is the component of the electric field along the probed direction.

Microscopically, the SHE arises from three distinct mechanisms: skew-scattering, side-jump, and the intrinsic mechanism. A natural framework for classifying these contributions is adopted from the theory of the anomalous Hall effect (AHE) [89], later generalized for the SHE. This classification is based on the dependence of each contribution on the momentum relaxation time τ_m, defined as the average time between consecu-

tive scattering events. The spin Hall conductivity is proportional to τ_{m} in the skew scattering and independent to τ_{m} in the side-jump and intrinsic mechanisms. Despite semiclassical approaches are present in the literature [20], [29], a consistent treatment of skew-scattering, side-jump and intrinsic effects requires an extended transport theory incorporating interband-coherence effects [90]. Here, we restrict ourselves to qualitative considerations regarding the three contributions.

Skew-scattering mechanism

Skew scattering is a consequence of chiral Mott scattering in solid-state systems [16] and is therefore connected to scattering centers, such as heavy nuclei and doping impurities. In Mott scattering [91], an electron beam incident on a target scatter elastically from nuclei and undergo an asymmetric, spin-dependent deflection due to SOC. As a result, the deflection angle is larger for scattering centers with a large atomic number. In crystals, skew scattering arises from chiral features when SOC is included in the Hamiltonian [29]. These features cause asymmetric deflection angles that depend on the electron's spin state. The spin dependence originates from different transition probabilities for right-handed and left-handed deviations relative to the electron's spin polarization direction. In the simplest picture of skew scattering [20], an electron approaches a charged scattering center and is deflected by its electrostatic field $\mathbf{E}$. In the rest frame of the electron moving with nonrelativistic velocity $\mathbf{v}$ ($v \ll c$), the electric field is accompanied by an effective magnetic field given by:

$$\mathbf{B} = \frac{\mathbf{E} \times \mathbf{v}}{2c^2}. \tag{1.63}$$

During the collision both $\mathbf{E}$ and $\mathbf{v}$ vary in space and time, yielding a nonuniform magnetic field $\mathbf{B}(\mathbf{r})$ which exerts opposite forces on opposite spin states:

$$\mathbf{F} = \boldsymbol{\mu}_{\mathrm{s}} \cdot \nabla \mathbf{B}(\mathbf{r}). \tag{1.64}$$

This spin-dependent asymmetry leads to a transverse deflection whose sign depends on the spin polarization.

The effective magnetic field $\mathbf{B}$ in Eq. (1.63) used to justify the asymmetric deflection comes from the spin-orbit interaction. This can be seen by expressing the SOC term in Eq. (1.30) as a Zeeman term for an electron immersed in an electrostatic potential. Using the relation between the gradient of the potential energy $\nabla V(\mathbf{r}) = e\mathbf{E}$ and the electric field $\mathbf{E}$, and the relation $\hat{\mathbf{v}} = \hat{\mathbf{p}}/m_0$, we express the spin-orbit Hamiltonian:

$$\hat{H}_{\mathrm{so}} = \frac{e\hbar}{4m_0c^2}\left(\mathbf{E}\times\hat{\mathbf{v}}\right)\cdot\hat{\boldsymbol{\sigma}} = \frac{e\hbar}{2m_0}\frac{\left(\mathbf{E}\times\hat{\mathbf{v}}\right)}{2c^2}\cdot\hat{\boldsymbol{\sigma}} = \frac{e\hbar}{2m_0}\hat{\mathbf{B}}\cdot\hat{\boldsymbol{\sigma}} = -\hat{\boldsymbol{\mu}}_{\mathrm{s}}\cdot\hat{\mathbf{B}}. \tag{1.65}$$

The force is finally obtained as $\mathbf{F} = -\nabla\hat{H}_{\mathrm{so}}$.

Intrinsic mechanism

Electrons can also experience intrinsic SHE [92], which is present even in a perfect crystal, free from disorder and impurities, and depends only on the band structure. In particular, it arises from the nonequilibrium dynamics of Bloch electrons in the presence of spin-dependent splitting [20]. In a system described by a two-dimensional Rashba Hamiltonian, the spin-dependent splitting is introduced by the combination of SOC and asymmetry of the crystal potential in the direction perpendicular to the plane. In this scenario, both a semiclassical approach based on the Bloch equations [41] and refined calculations with the Kubo formula [93] of the spin Hall conductivity predicts that the transverse spin current generated by the intrinsic SHE is linked to the momentum-space Berry phase [94]. Owing to this Berry phase dependence, the largest spin Hall angles occur when the spin-dependent splitting at the Fermi level is large. This mechanism predicts particularly large spin Hall angles in heavy transition metals.

Side-jump mechanism

The side-jump mechanism is introduced after the skew-scattering and the intrinsic contributions from equation [29]:

$$\sigma_{\mathrm{SH}} = \sigma_{\mathrm{SH}}^{\mathrm{int}} + \sigma_{\mathrm{SH}}^{\mathrm{ss}} + \sigma_{\mathrm{SH}}^{\mathrm{sj}}, \tag{1.66}$$

where $\sigma_{\mathrm{SH}}^{\mathrm{int}}$ and $\sigma_{\mathrm{SH}}^{\mathrm{ss}}$ are the spin Hall conductivity of intrinsic and skew-scattering mechanisms. From a semiclassical approach based on classical mechanics [20], an electron displaces laterally after a collision in the side-jump mechanism, with the direction of displacement depending on its spin state. This effect results from the local distortion induced by SOC of the electron wavefunction near a scattering center and was first proposed in the context of the AHE [95]. Nevertheless, from microscopic theories [89], [90] the process results scattering-independent, as indicated by its lack of dependence on the momentum lifetime τ_{m}. The underlying mechanism comprises two contributions [29]: one arises from the scattering of the SOC-uncorrelated part of the electron's wavefunction from the disorder Hamiltonian that includes SOC, while the other originates from the scattering of the SOC-correlated part from the scalar potential without SOC. The first contribution is captured by the semiclassical approach and dominates in systems with weak spin-orbit

coupling, whereas the second is dominant in heavy elements. In simple models, the side jump does not alter the electron's velocity, in contrast to skew scattering which changes the propagation direction. We now turn to describe spin relaxation.

1.2.6. Spin relaxation

Several distinct microscopic processes contribute to spin relaxation in the conduction band of non-magnetic semiconductors. All mechanisms rely on an additional spin-dependent term in the full Hamiltonian that leads to the presence of time-varying, effective magnetic fields [11]. These induce stochastic spin precession and the progressive loss of information regarding the spin momentum.

Elliott-Yafet mechanism

The first mechanism is the Elliott-Yafet (EY), in which spin relaxation occurs through momentum scattering from phonons or impurities combined with SOC [96], [97]. During a scattering event, an effective magnetic field $\mathbf{B}$ is generated by SOC from the electric field associated with perturbations of the lattice potential or charged impurities [20], as shown for the skew scattering in Eq. (1.65). If the electron spin is not exactly parallel to the effective magnetic field, it will precess around $\mathbf{B}$ during the time of collision, causing spin relaxation. An alternative perspective on this mechanism is to note that the electronic states in crystals are not pure spin states, but contain small admixtures of opposite-spin components because of SOC. Consequently, each scattering event carries a finite probability for a spin flip and the spin lifetime $\tau_{\mathrm{s}}^{\mathrm{EY}}$ scales with the momentum lifetime τ_{m}, which is the characteristic time elapsed between two consecutive scattering events. This mechanism operates in materials both with and without inversion symmetry, and is the leading term in centrosymmetric semiconductors such as Ge and Si [11]. For details regarding the EY theory and its derivation, I remand to Refs. [96]–[98]. Here, the approximation firstly introduced by Chazalviel [99] for III-V semiconductors based on the Kane model [56] is used to have a quantitative expression of the spin relaxation rate:

$$(\tau_{\mathrm{s}}^{\mathrm{EY}})^{-1} = A \left(\frac{\Delta_{\mathrm{so}}}{E_{\mathrm{g}} + \Delta_{\mathrm{so}}} \frac{E_{\mathrm{k}}}{E_{\mathrm{g}}} \right)^2 (\tau_{\mathrm{m}})^{-1}, \tag{1.67}$$

where A is a numerical factor of order 1 and E_{k} is the electron kinetic energy. This expression is obtained calculating the band structure near the Γ point using the Kane model [56], and therefore it is rigorously valid only for $\mathbf{k} \simeq 0$.

It is worth to note that strong SOC in the valence bands produces substantial spin mixing,

making hole spin relaxation extremely efficient through the EY mechanism. In semiconductors, the spin relaxation time of holes in the VB is in order of magnitude close to the hole momentum lifetime. The fast spin relaxation of spin-polarized holes justify to neglect their contribution to spin injection and transport in this work.

Dyakonov-Perel mechanism

A second spin relaxation mechanism is the Dyakonov-Perel (DP), which is active in non-centrosymmetric materials, such as zinc-blende and chalcopyrite semiconductors [16]. BIA and SOC lead to spin splitting of the band structure outside the TRIMs, which can be seen as the effect of an effective, momentum-dependent magnetic field. In particular, the spin-dependent term in the full Hamiltonian of zinc-blende semiconductors is the Dresselhaus in Eq. (1.50), that can be rewritten to explicit the effective magnetic field $\mathbf{\Omega}(\mathbf{k})$:

$$\hat{H}_{\mathrm{DH}} \sim \mathbf{\Omega}(\mathbf{k}) \cdot \hat{\boldsymbol{\sigma}}. \tag{1.68}$$

where:

$$\Omega_{\mathrm{x}} = k_{\mathrm{x}} \left(k_{\mathrm{y}}^2 - k_{\mathrm{z}}^2\right), \quad \Omega_{\mathrm{y}} = k_{\mathrm{y}} \left(k_{\mathrm{z}}^2 - k_{\mathrm{x}}^2\right), \quad \Omega_{\mathrm{z}} = k_{\mathrm{z}} \left(k_{\mathrm{x}}^2 - k_{\mathrm{y}}^2\right).$$

The spin precesses around this field as electrons propagate. Momentum scattering from phonons or impurities alters the electron's wavevector, and hence the magnitude and direction of the effective field. The precession axis and frequency therefore change randomly after each scattering event. Spin relaxation arises through this stochastic precession rather than during the scattering events themselves. As a result, increasing the scattering rate suppresses spin relaxation in the DP mechanism. For details regarding the full derivation of the DP depolarization, I remand to Refs. [11], [16]. Here, the spin relaxation rate related to this mechanism is evaluated following the Pikus-Titkov model for thermalized electrons in III-V semiconductors [98]:

$$(\tau_{\mathrm{s}}^{\mathrm{DP}})^{-1} = \frac{Q\alpha_c^2 (k_{\mathrm{B}}T)^3}{\hbar^2 E_{\mathrm{g}}} \tau_{\mathrm{m}}, \tag{1.69}$$

where Q is a dimensionless parameter of order 1 that depends on the dominant scattering mechanism, α_c is the spin splitting parameter due to BIA, k_{B} is the Boltzmann constant, and T is the lattice temperature. The factor $k_{\mathrm{B}}T$ is the thermal energy.

Bir-Aronov-Pikus mechanism

In p-doped semiconductors (not treated in this thesis), the dominant mechanism is often

the Bir-Aronov-Pikus (BAP) process [100]. In this case, spin relaxation proceeds via the exchange interaction between electrons and holes. Although electron-electron exchange conserves the total spin and does not by itself lead to relaxation, exchange with holes becomes effective because the hole spin decays rapidly due to the EY mechanism. Therefore, holes act as a fast spin-relaxation reservoir: spin-polarized electrons transfer their spin to the hole system, where it is quickly lost. For details regarding this spin depolarization mechanism, I remand to Refs. [98], [100]. Here, we neglect its contribution dealing always with n-doped semiconductors. The knowledge of the typical timescales on which scattering phenomena occur is therefore essential for determining spin relaxation and, consequently, transport properties. In Ch. 3, momentum and spin lifetimes of polarized electrons are calculated evaluating scattering and relaxation processes in n-doped Ge, Si, and GaAs.

2 | Methods

This chapter presents the methodologies implemented during experiments. Section 2.1 describes the basic principles behind ARPES, which is used to characterize electronic states of $CdGeAs_2$. Section 2.2 illustrates the growth process of $CdGeAs_2$ single crystals. Section 2.3 presents the equipment implemented in the ARPES characterization on $CdGeAs_2$. Section 2.4 explains the instrumentation employed in the photoinduced ISHE measurements on $CdGeAs_2$.

2.1. General description of ARPES

ARPES is a spectroscopy technique based on the photoelectric effect, in which a photon with energy $\hbar\omega$ incident on a sample is absorbed by an electron that can escape from the material with a maximum kinetic energy $\hbar\omega - \phi$. ϕ is the material work function, *i.e.*, the value of the potential barrier at the surface that prevents the valence electrons from escaping, and is typically around $4 - 5\,\mathrm{eV}$ for metals. In ARPES, photons eject electrons from a crystalline solid into the vacuum and, by measuring their kinetic energy and emission direction, one reconstructs the energy dispersion of the occupied electronic states.

An ARPES setup is constitute by a beam of monochromatized radiation supplied by a source, for instance a gas-discharge lamp, or an high-harmonic generation (HHG) system, or a synchrotron beamline. The light impinges on a freshly exposed sample surface, which has to be properly prepared and aligned to reconstruct the energy dispersion. Electrons are emitted into many directions because of the photoelectric effect, and collected by an electron energy analyzer characterized by a finite acceptance angle and a detector. The analyzer measures the kinetic energy E_k for given emission angles θ, which allows to determine the electron momentum $\mathbf{p}$, assuming a nearly free-electron final state. Its modulus is given by $p = \sqrt{2m_0 E_\mathrm{k}}$, and its components parallel and perpendicular to the sample surface are determined by:

$$\mathbf{p} = \begin{pmatrix} \mathbf{p}_{\parallel} \\ \mathbf{p}_{\perp} \end{pmatrix} = \sqrt{2m_0 E_{\mathrm{k}}} \begin{pmatrix} \sin\theta \\ \cos\theta \end{pmatrix}. \tag{2.1}$$

Within a non-interacting electron picture, energy conservation relates E_{k} to $\hbar\omega$, ϕ, and the binding energy E_{B} of the initial state, defined with respect to the Fermi level E_{F}:

$$E_{\mathrm{k}} = \hbar\omega - \phi - |E_{\mathrm{B}}|. \tag{2.2}$$

Whereas, momentum conservation relates $\mathbf{p}_{\parallel}$ to the in-plane crystal momentum $\hbar\mathbf{k}_{\parallel}$ through:

$$\mathbf{p}_{\parallel} = \hbar\mathbf{k}_{\parallel} + \mathbf{G}_{\parallel} = \sqrt{2m_0 E_{\mathrm{k}}}\sin\theta. \tag{2.3}$$

where $\mathbf{G}_{\parallel}$ is a generic in-plane reciprocal lattice vector. Here, the momentum transfer from the photon is neglected because of the low photon energies employed in ARPES experiments. Therefore, at larger θ, one can probe electrons with momenta $\mathbf{k}_{\parallel}$ located in higher-order BZs. Subtracting the appropriate reciprocal-lattice vector $\mathbf{G}$ yields the corresponding reduced crystal momentum folded back into the first BZ. Because the electron escape depth is finite (typically $\lesssim 1\,\mathrm{nm}$ for $\hbar\omega$ within $20-100\,\mathrm{eV}$ [101]), ARPES is inherently surface sensitive. This implies that while the in-plane momentum $\mathbf{k}_{\parallel}$ is conserved up to a surface reciprocal lattice vector, the out-of-plane component $\mathbf{k}_{\perp}$ is not conserved because of broken translational symmetry. However, the discontinuity at the surface of $\mathbf{k}_{\perp}$ can be accounted by a step-like function V_0:

$$\mathbf{k}_{\perp} = \sqrt{\frac{2m}{\hbar^2}\Big(E_{\mathrm{k}}\cos^2\theta + V_0\Big)}. \tag{2.4}$$

The V_0 function represents the inner potential, *i.e.*, the electrostatic potential experienced by an electron inside a material. The Eq. (2.4) is useful for tracking $\mathbf{k}_{\perp}$ dispersion by varying $\hbar\omega$ and, consequently, E_{k}. Once the analyzer energy scale is calibrated and the sample is referenced to a well-defined E_{F}, Eqs. (2.2) - (2.4) provide a direct conversion from the measured quantities, E_{k} and θ, to the energy dispersion $\varepsilon_{\mathbf{k}} = |E_{\mathrm{B}}(\mathbf{k})|$ inside a solid.

Contributions to ARPES spectra

In a real ARPES experiment the primary observable is not the energy dispersion $\varepsilon_{\mathbf{k}}$, but the photoemission intensity, which can vary strongly with photon energy, light po-

larization, and experimental geometry even when the underlying electronic structure is unchanged. Within a standard description [102], the measured intensity can be written as:

$$I_{\text{meas}}(\mathbf{k},\nu) = \Big[I_0(\mathbf{k},\hbar\omega,\mathbf{E})\, f(\nu)\, A(\mathbf{k},\nu)\Big] \otimes R(\Delta\mathbf{k},\Delta\nu) + B(\mathbf{k},\nu), \tag{2.5}$$

where ν is the electron energy with respect to the E_{F}, $f(\nu)$ is the Fermi-Dirac distribution, $A(\mathbf{k},\nu)$ is the single-particle spectral function, $I_0(\mathbf{k},\hbar\omega,\mathbf{E})$ contains the matrix-element effects, $R(\Delta\mathbf{k},\Delta\nu)$ accounts for the finite instrumental resolution in energy and momentum, $B(\mathbf{k},\nu)$ denotes the inelastic background, and $\otimes$ indicates the convolution product. The Eq. (2.5) highlights that ARPES intensity encodes both intrinsic electronic states through $A(\mathbf{k},\nu)$ and extrinsic modulations through I_0, R, and B.

The dispersion that one extracts from the data is encoded in $A(\mathbf{k},\nu)$. The spectral function represents the probability of removing an electron with momentum $\mathbf{k}$ and energy ν, leaving the system in an excited (N-1)-particle state. In the non-interacting limit, $A(\mathbf{k},\nu)$ collapses to a delta peak at the band energy, $A(\mathbf{k},\nu) \propto \delta(\nu - \varepsilon_{\mathbf{k}})$, so the measured maxima directly trace the bare band structure $\varepsilon_{\mathbf{k}}$. However, interactions in real materials enter through the self-energy $\Sigma(\mathbf{k},\nu) = \Sigma'(\mathbf{k},\nu) + i\Sigma''(\mathbf{k},\nu)$, which renormalizes and broadens the spectral features. As a result, the observed band dispersion is given approximately by the peak condition $\nu \simeq \varepsilon_{\mathbf{k}} + \Sigma'(\mathbf{k},\nu)$, while the linewidth is governed by $\Sigma''(\mathbf{k},\nu)$. Therefore, $A(\mathbf{k},\nu)$ contains the intrinsic information on the electronic structure and many-body effects.

The prefactor $I_0(\mathbf{k},\hbar\omega,\mathbf{E}) \propto M_{\text{i,f}}(\mathbf{k})^2$ summarizes how the photoemission intensity depends on the light-matter interaction within the electric dipole approximation. This includes dependencies on the electron wave vector $\mathbf{k}$, the photon energy $\hbar\omega$, and the polarization vector $\mathbf{E}$. Consequently, intensity modulations as a function of $\hbar\omega$ can arise from both $\mathbf{k}_\perp$ dispersion and dipole matrix-element effects, and should therefore be interpreted with care. Another key consequence is that ARPES is selective, which means that specific orbitals and symmetries can be enhanced or suppressed by choosing the measurement geometry and polarization. For instance, with respect to a mirror plane defined by the analyzer slit and the sample normal, p- and s-polarized light can preferentially couple to initial states of different parity, leading to pronounced intensity variations without any change in the underlying band dispersion. Moreover, the $\mathbf{k}$ dependence hides a θ-angle dependence of the matrix element, affecting the intensity for different emission angles. This point is essential when interpreting constant-energy maps and repeated BZs. Even if two momenta are equivalent by in-plane reciprocal-lattice translation, $\mathbf{k}_\parallel \to \mathbf{k}_\parallel + \mathbf{G}$, the

dispersion remains identical, but the intensity may differ markedly because $M_{\mathrm{i,f}}(\mathbf{k})^2$ can change with emission direction, besides energy and polarization of the incoming photon.

The factor $f(\nu)$ restricts ARPES to occupied states. Near E_{F}, finite temperature smears the cutoff, and the measured spectrum is further broadened by the instrumental resolution $R(\Delta\mathbf{k}, \Delta\nu)$, commonly approximated by a Gaussian in energy. Experimentally, the energy resolution is often characterized by measuring the Fermi edge of a reference metal and fitting it as a convolution of a Fermi-Dirac function with a Gaussian. The momentum resolution, in turn, depends on the photon energy, angular (θ-angle) resolution, emission angle, and any additional broadening mechanisms. The most relevant are vibrations, sample-charging effects, space-charge effects at high flux, and surface inhomogeneities. The effective spectral resolution is affected by both $R(\Delta\mathbf{k}, \Delta\nu)$ and the intrinsic linewidth of the bands $\Sigma''(\mathbf{k}, \nu)$. While $R(\Delta\mathbf{k}, \Delta\nu)$ is fixed by the source and analyzer settings, $\Sigma''(\mathbf{k}, \nu)$ reduces by cooling the sample since electron-phonon scattering rate decreases, improving the spectral quality.

Eventually, photoelectrons can undergo inelastic scattering during transport to the surface after being excited in the bulk and before escaping into vacuum, as correctly accounted by a three-step model [102]. Inelastic scattering generates secondary electrons that contribute to a smooth, typically weakly dispersive background $B(\mathbf{k}, \nu)$. In practice, band dispersions are commonly extracted by tracking maxima in energy and momentum distribution curves, EDCs and MDCs, respectively. In quantitative analyses based on EDCs or MDCs, it is therefore common to include a background term in the fit of the intensity. The Eq. (2.5) makes clear that the visibility of a band depends not only on $A(\mathbf{k}, \nu)$ but also on $I_0(\mathbf{k}, \hbar\omega, \mathbf{E})$ and $B(\mathbf{k}, \nu)$. Therefore, when a feature is weak or missing in a given cut or map, it is good practice to test its robustness by varying photon energy and polarization, and to compare symmetry-related cuts to disentangle genuine electronic-structure effects from matrix-element-induced contrast.

2.2. Strategy for $CdGeAs_2$ growth

High-quality $CdGeAs_2$ single crystals are grown by chemical vapor transport (CVT) using bromine as the transport agent. This approach is particularly suited to $CdGeAs_2$, where the strong anisotropy of the thermal expansion coefficients often leads to cracking during cooling in melt-based growth methods. CVT has been shown to yield large crack-free crystals in this material [74].

Here, polycrystalline $CdGeAs_2$ is first synthesized by solid-state reaction. Stoichiometric amounts of 4N-purity Cd, Ge, and As are sealed under high vacuum in a carbon-coated

quartz ampule. The mixture is reacted at 550°C and 650°C for 24 h, with intermediate grinding performed in an Ar-filled glove box to improve homogeneity. For CVT growth, the resulting powders are mixed with liquid bromine (2 μl/cm^3) and sealed in a 40 cm-long quartz ampule at an internal pressure of $\sim 10^{-1}$ Pa. The charge and growth ends of the ampule are placed in a horizontal two-zone furnace held at 675°C and 650°C, respectively, for 200 h. In the CVT ampule, the charge end (hot zone) contains the starting polycrystalline material and transport agent, where volatile species are generated, whereas the growth end (cold zone) is where these species recondense and crystallize [103]. After growth, the furnace is cooled to room temperature at 2°C/min, and single crystals are collected from the growth end of the ampule.

2.3. Equipment for ARPES on $CdGeAs_2$

ARPES measurements on $CdGeAs_2$ are carried out at the APE-LE beamline of the Elettra synchrotron (Trieste), which provides tunable vacuum ultra violet (VUV) photons with variable polarization in the 10-100 eV range. Photoelectrons are analyzed with a Scienta Omicron DA30 hemispherical analyzer operated in deflection mode for the lens system, enabling the acquisition of θ-angle maps without rotating the sample. Linear horizontal and vertical polarizations are employed in the $50 - 86$ eV photon-energy range to scan the out-of-plane momentum and probe the three-dimensional dispersion of bulk bands. The angular resolution is set to 0.5°, and the overall energy resolution, considering the beamline and the analyzer, is ~ 30 meV. Samples are measured at $T = 130$ K, providing a compromise between improved spectral quality and limited sample-charging effects. In semiconductors, charging effects are particularly critical because the low conductivity can prevent the sample from rapidly replenishing the photoemitted electrons, leading to a non-uniform electrostatic potential at the surface [104]. This alters the trajectories and kinetic energies of the emitted electrons, thereby shifting and broadening spectral features. In practice, charging is mitigated by improving electrical contact and by increasing the sample temperature to enhance carrier conductivity. Therefore, thermal and electrical contact with the sample holder is ensured using conductive silver epoxy.

2.4. Equipment for photoinduced ISHE on $CdGeAs_2$

Spin-to-charge conversion in $CdGeAs_2$ is investigated by optical orientation, where circularly polarized light excites spin-polarized electrons in the CB through dipole-allowed optical transitions. As the injected spin population diffuse, spin-dependent scattering generates an electromotive field via the ISHE, according to Eq. (1.62), which is detected

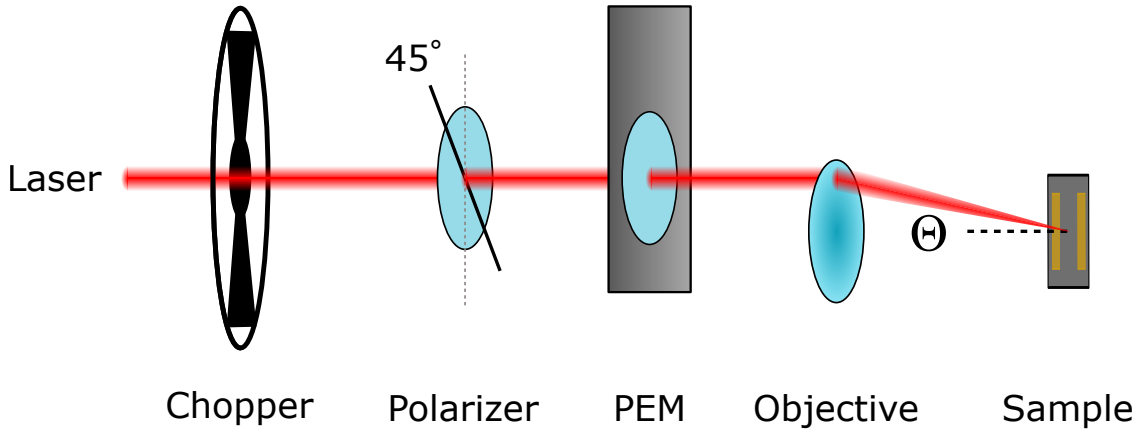

Figure 2.1: Schematic of the photoinduced ISHE setup. The laser passes through a chopper to modulate the intensity, and a photoelastic modulator (PEM) combined with a linear polarizer to alternate periodically circular polarization states. Then, the light passes through an objective lens in an off-axis configuration and is focused with a polar angle Θ with respect to the sample normal.

as a voltage drop ΔV_{ISHE} across two electrodes evaporated at the crystal edges. Fig. 2.1 presents the measurement setup. A double-modulation scheme is employed: the circular polarization is modulated at 50 kHz by a photoelastic modulator (PEM), while the beam intensity is modulated at 23 Hz by a mechanical chopper. The laser beam is focused onto the sample at a polar angle Θ with respect to the sample normal, using an off-axis configuration with a 0.65 numerical-aperture 40×magnification polarization-maintaining objective. The signal is demodulated using two lock-in amplifiers in cascade, tuned to the PEM and chopper frequencies, respectively. All ISHE measurements are carried out at room temperature.

Light source

The excitation source is a monochromatized pulsed supercontinuum laser (SuperK FIANIUM FIR-20, NKT Photonics) covering the $0.65 - 1.15$ eV photon-energy range with a bandwidth within $10 - 20$ meV. The laser has a repetition rate of 78 MHz, and each pulse in output lasts for a few nanoseconds. The laser emits a collimated broadband beam with an overall power of ≈ 6.5 W, consisting of wavelengths in the range of $475 - 2400$ nm. The fundamental wavelength is 1064 nm. A Pellin-Broca prism is exploited to monochromatize the emitted light. As depicted in Fig. 2.2, this prism separates the various photon frequencies in the output beam by dispersing them. The prism is placed on top of a controlled mechanical rotator, which enables the irises to select a certain photon frequency coming from the laser source. As a result, the final beam coupled with a multimode fiber (50 μm-large core) has a peak at a given photon energy and bandwidths between

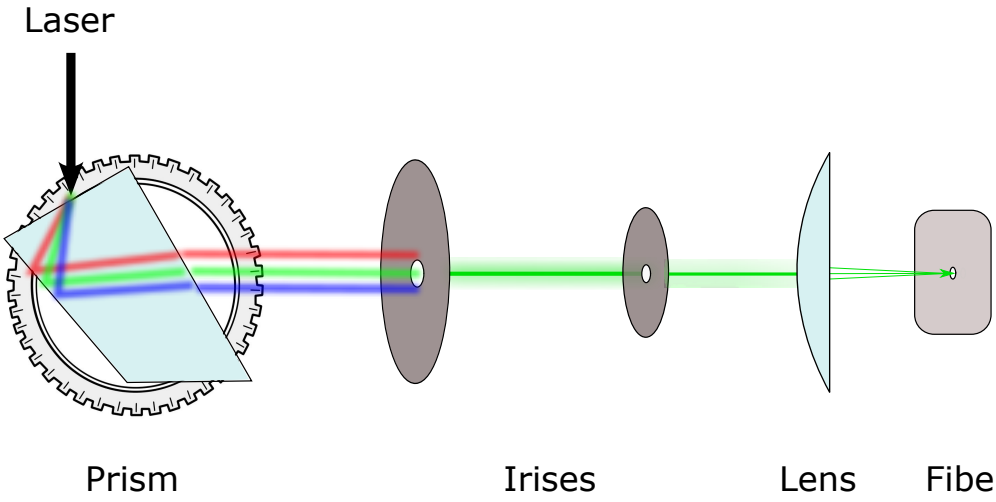

Figure 2.2: Functional scheme of a monochromator based on a Pellin-Broca prism. The prism splits the various photon frequencies (different colors) contained in the supercontinuum laser beam by dispersing them. It is mounted on a mechanical rotator, which allows the irises to select a desired wavelength in the output beam for a given rotational angle. A focusing lens is then used for coupling the beam inside a multimode fiber.

$10 - 20\,\text{meV}$. To link each rotational angle to the appropriate $\hbar\omega$ and bandwidth ΔE, a preliminary calibration is required. The optical power W of the monochromatized laser after leaving the fiber is shown in Fig. 2.3a, as a function of the photon energy. The power peak results $\approx 4\,\text{mW}$ and is achieved at approximately $0.95\,\text{eV}$. The average bandwidth in Fig. 2.3b is in the range between $10 - 20\,\text{meV}$ and is almost consistent across the energy spectrum.

Photoelastic modulator

The light polarization is modulated in time using a PEM, that alternates periodically σ^+ and σ^- polarization states with a frequency $\omega = 50\,\text{kHz}$. The photoelastic effect, a direct correlation between applied strain and changes of the refractive index in a material, is at the basis of the PEM's operation. Indeed, the PEM periodically exerts a mechanical strain on an SiO_2 window along a fixed axis, modulating in this manner its refractive index. The PEM long axis (OA_{PEM}) is defined as the axis parallel to the applied strain direction. Consequently, the electric field component perpendicular to OA_{PEM} has a different phase delay compared to the one oriented parallel. The phase difference between the two components varies periodically, in accordance with the modulation frequency ω:

$$\phi = R_{\text{PEM}} \cos(\omega t), \tag{2.6}$$

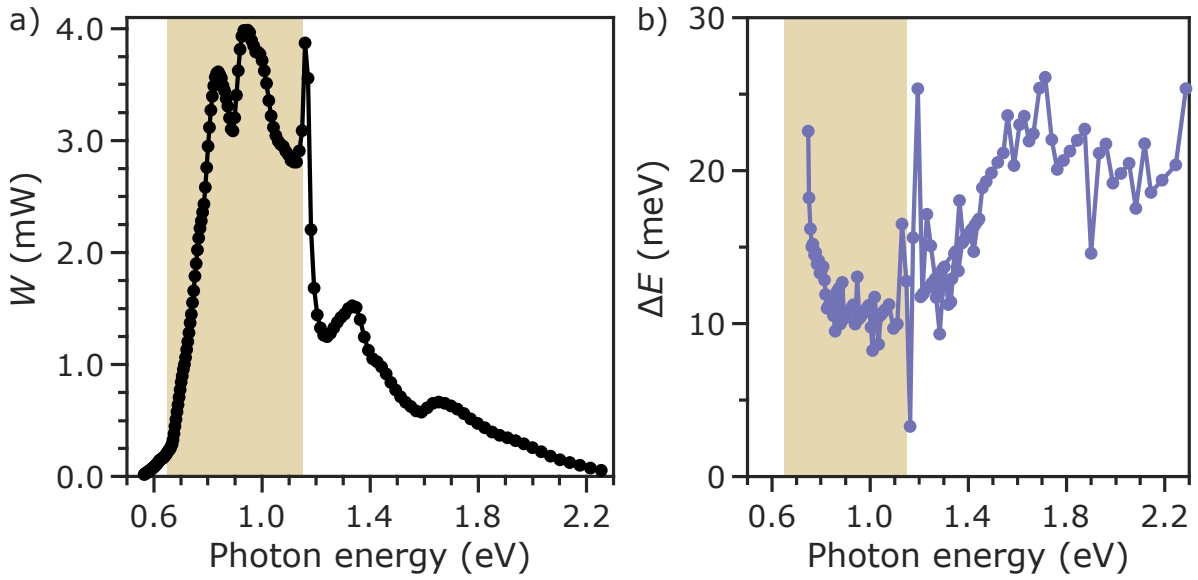

Figure 2.3: The photon-energy dependence of (a) the optical power W, and (b) the energy bandwidth ΔE, after the multimode fiber. The region in brown-yellow highlights the range explored in photoinduced ISHE measurements.

where R_{PEM} is the maximum phase difference called the retardation. In the optimal configuration, the light passes firstly through a linear polarizer positioned at an angle $\vartheta_{\mathrm{p}} = \pm 45°$ with respect to the $\mathrm{OA_{PEM}}$ and then through the SiO_2 window, as shown in Fig. 2.4. To characterize the output circular polarization, we express the electric field components that enter the PEM as functions of ϑ_{p}:

$$\mathbf{E}_{\mathrm{in}} = \begin{pmatrix} E_0 \sin\vartheta_{\mathrm{p}} \\ E_0 \cos\vartheta_{\mathrm{p}} \end{pmatrix}. \tag{2.7}$$

Within the Jones calculus, the PEM matrix can be expressed for the $\mathrm{OA_{PEM}}$ along the y axis in the geometry of Fig. 2.4 as follows:

$$\mathbf{M}_{\mathrm{PEM}} = \begin{pmatrix} e^{i\frac{\phi}{2}} & 0 \\ 0 & e^{-i\frac{\phi}{2}} \end{pmatrix}. \tag{2.8}$$

The electric field in output from the PEM is thus calculated as $\mathbf{E}_{\mathrm{out}} = \mathbf{M}_{\mathrm{PEM}} \cdot \mathbf{E}_{\mathrm{in}}$, and turns out to be:

$$\mathbf{E}_{\mathrm{out}} = \begin{pmatrix} E_0 \sin\vartheta_{\mathrm{p}}\, e^{i\frac{\phi}{2}} \\ E_0 \cos\vartheta_{\mathrm{p}}\, e^{-i\frac{\phi}{2}} \end{pmatrix} = \begin{pmatrix} E^x_{\mathrm{out}} \\ E^y_{\mathrm{out}} \end{pmatrix}. \tag{2.9}$$

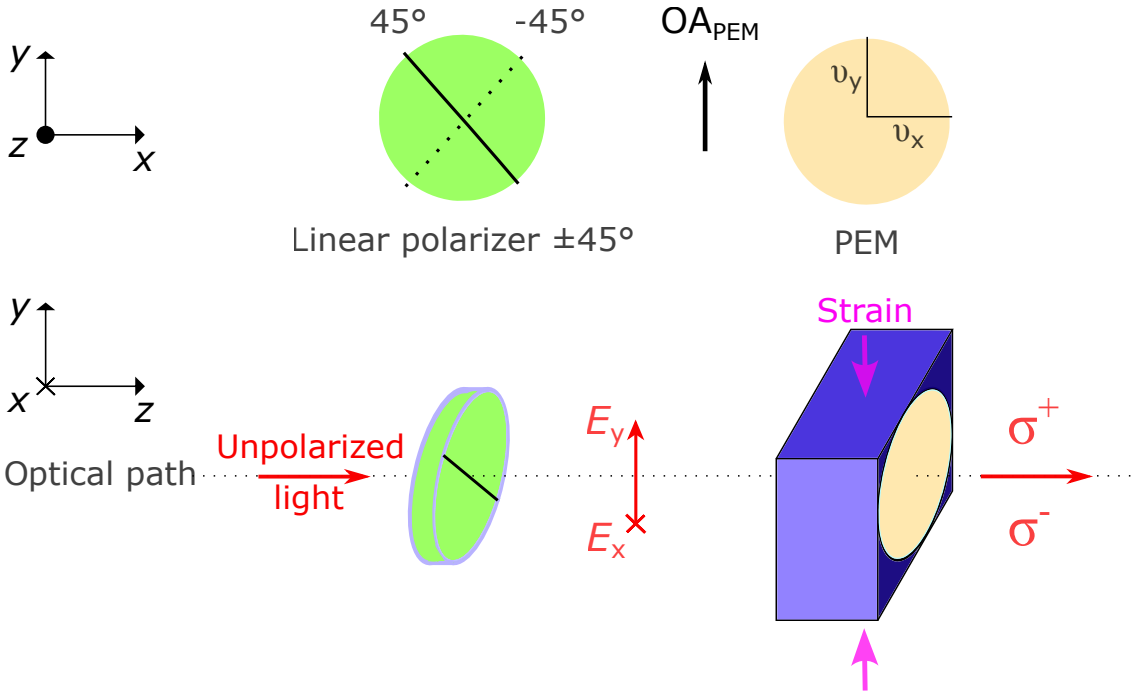

Figure 2.4: Scheme of the linear polarizer and photoelastic modulator (PEM) effects along the optical path. The PEM long axis (OA_{PEM}) is parallel to the applied strain direction along the y axis. The linear polarizer (in green) is set with an angle of $\pm 45°$ with respect to OA_{PEM}. The refractive index of the SiO_2 window (in orange) is thus modulated along the y axis (υ_y), while the one along the x axis (υ_x) remains unchanged. The light outgoing from the PEM results circularly polarized ($\sigma^{\pm}$) by applying a sufficiently strong modulation.

The circular polarization state is obtained projecting $\mathbf{E}_{out}$ on the Jones vectors of σ^+- and σ^--polarized light:

$$\sigma^+ \longrightarrow \frac{1}{\sqrt{2}}\begin{pmatrix}1\\+i\end{pmatrix}, \tag{2.10a}$$

$$\sigma^- \longrightarrow \frac{1}{\sqrt{2}}\begin{pmatrix}1\\-i\end{pmatrix}. \tag{2.10b}$$

The components on this basis of the output electric field are:

$$E^+_{out} = \frac{1}{\sqrt{2}}(E^x_{out} + iE^y_{out}), \tag{2.11a}$$

$$E^-_{out} = \frac{1}{\sqrt{2}}(E^x_{out} - iE^y_{out}). \tag{2.11b}$$

At this stage, the degree of circular polarization (DCP) is introduced:

$$\mathrm{DCP} = \frac{I^+ - I^-}{I^+ + I^-}, \tag{2.12}$$

where $I^{\pm} \propto |E^{\pm}_{\mathrm{out}}|^2$ is the intensity. Therefore, the DCP is given by:

$$\mathrm{DCP} = \frac{i(E^{x*}_{\mathrm{out}} E^{y}_{\mathrm{out}} - E^{x}_{\mathrm{out}} E^{y*}_{\mathrm{out}})}{E^{x}_{\mathrm{out}} E^{x*}_{\mathrm{out}} + E^{y}_{\mathrm{out}} E^{y*}_{\mathrm{out}}} = \sin(\phi)\sin(2\vartheta_{\mathrm{p}}), \tag{2.13}$$

and the choice of $\vartheta_{\mathrm{p}} = \pm 45°$ correctly maximizes the DCP. We substitute Eq. (2.6) in Eq. (2.13) and expand the DCP in Fourier series to disentangle contributions at different frequencies, obtaining:

$$\mathrm{DCP} \approx 2J_1(R_{\mathrm{PEM}})\cos(\omega t) - 2J_3(R_{\mathrm{PEM}})\cos(3\omega t), \tag{2.14}$$

where $J_1(R_{\mathrm{PEM}})$ and $J_3(R_{\mathrm{PEM}})$ are the first and third Bessel functions, respectively. Hence, the intensity of a signal demodulated at the first harmonic (ω) and proportional to the circular polarization has to follow the dependence of $J_1(R_{\mathrm{PEM}})$, which reaches its maximum for $R_{\mathrm{PEM}} = 106°$. In wavelength units, this retardation corresponds to $\approx 0.3\lambda$. Fig. 2.5a presents the time dependence of the DCP for various $R_{\mathrm{PEM}}(\lambda)$. The retardation can be set together with the wavelength to get the desired polarization modulation in output. The light passes in time through linear, elliptical, and circular polarization states only if $R_{\mathrm{PEM}} \geq 0.25\lambda$. This threshold corresponds to the PEM operating as a quarter-wave plate when it applies the maximum strain. Nevertheless, the first harmonic component of the DCP is maximum for $\approx 0.3\lambda$, as denoted from the Fourier analysis, and this is because polarization remains circular for longer periods. Increasing further R_{PEM}, the PEM overmodulates the polarization with benefits only if working at different harmonics. Fig. 2.5b shows the $J_1(R_{\mathrm{PEM}})$ function. A useful test is to reproduce the Bessel functions by varying continuously R_{PEM} to verify the DCP-dependency of the signal. In photoinduced ISHE experiments, a spin-dependent signal has also to be DCP-dependent and, therefore, this measurement is often done.

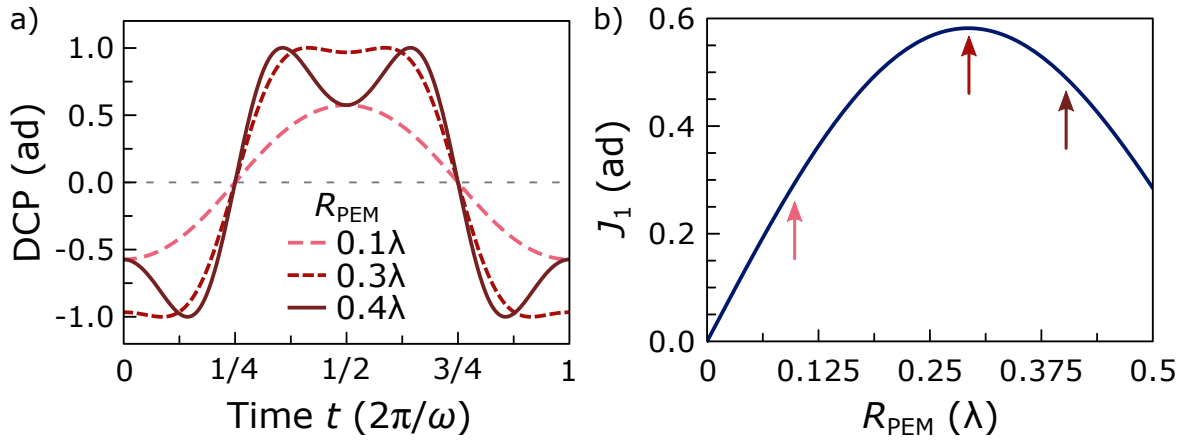

Figure 2.5: (a) Temporal dependence of the DCP for different PEM retardation $R_{\mathrm{PEM}} = 0.1\lambda$ (pink), 0.3λ (red), and 0.4λ (dark red). (b) First Bessel function $J_1(R_{\mathrm{PEM}})$. The arrows show the values of R_{PEM} used in (a). (Adapted from Ref. [105])

3 | Results

This chapter presents the main results of the experimental work discussed in the thesis. Section 3.1 describes ARPES measurements carried on $CdGeAs_2$ and provides a comparison with the 8-band $\mathbf{k} \cdot \mathbf{p}$ model of Sec. 1.2.4. Section 3.2 presents optical orientation in $CdGeAs_2$. Section 3.3 reports findings of spin-to-charge conversion on $CdGeAs_2$ by generating spin-polarized currents via optical orientation. Section 3.4 presents calculations of the spin lifetime τ_s in Ge, Si, and GaAs. Section 3.5 discusses simulations of spin-polarized electron transport dynamics in the drift-diffusion regime, furnishing cut-off frequencies for spin current modulation in the three semiconductors.

3.1. Electronic structure of $CdGeAs_2$

In this section, we present an ARPES investigation of the electronic band structure of $CdGeAs_2$, which, to the best of our knowledge, constitutes the first such study of this chalcopyrite semiconductor. Atomically clean surfaces are obtained by cleaving in ultra-high vacuum, despite $CdGeAs_2$ does not present a unique preferential cleavage plane because of its strong 3D character. Crystals are generally prismatic and elongated along [111], naturally exposing optically smooth (112), (101), and (011) faces [74]. After fracturing more than twenty crystals, band dispersions are observed only for the (112) termination as confirmed by post-cleaving Laue diffraction, with a success rate of $\sim 20\%$. The components of the electron wavevector k_x, k_y, and k_z sampled with ARPES are shown in Fig. 3.1a in the first BZ. The k_y and k_z axes are parallel to low-symmetry directions, whereas the k_x axis is parallel to the ΓX direction ($\Gamma X = 0.52\,\text{Å}^{-1}$). Fig. 3.1b reports a constant-energy map acquired at $E - E_F = -0.2\,\text{eV}$ with a photon energy of 72.5 eV. The Fermi level E_F is measured on polycrystalline silver in electrical contact with the crystal. Along the k_x direction, the map shows valence-band maxima forming pockets centered at Γ and Γ' and separated by twice the ΓX distance, confirming the alignment of the sample. The absence of spectral weight at negative k_x values in the BZ is ascribed to matrix-element effects. Fig. 3.1c presents the valence-band dispersion along ΓX obtained with 72.5 eV photon energy, where three distinct states at the top of the valence-band

manifold are resolved. The states are labeled VB1, VB2, and VB3, in agreement with the notation used in Sec. 1.2.4. Fig. 3.1d presents energy distribution curves collected at the Γ point as functions of photon energy, which show the valence-band dispersion along k_z. A parabolic behavior is discernible for VB1, which reaches its maximum for photon energies in the $77 - 86\,\mathrm{eV}$ range, whereas the dispersion of VB2 and VB3 is not clearly resolved. Figs. 3.2a and 3.2b show the valence-band dispersions measured with a photon energy of 86 eV along k_x and k_y, respectively. The energy splitting at the Γ point between VB2 and VB3, induced by the combination of tetragonal crystal field and spin-orbit interaction, is confirmed experimentally. However, a reliable quantitative estimation of the energy distance is hampered because of weak signal and band broadening. Likewise, the splitting between VB1 and VB2 and the spin splitting expected from inversion-symmetry breaking for $\mathbf{k} \neq 0$ cannot be resolved. Note that the broadening does not originate from energy resolution limitations, but from k_z integration due to the surface sensitivity of ARPES and the bulk character of the bands.

To quantify the dispersions, momentum distribution curves (MDCs) are extracted within a 25 meV energy window between $E - E_F = -1.75$ and $-0.25\,\mathrm{eV}$. Each MDC is fitted with a variable number of Lorentzian peaks on top of a quadratic background and the resulting peak positions are used to trace the band dispersions. The same analysis is repeated for photon energies of 77, 83 and 86 eV. Figs. 3.2c and 3.2d report the very same band dispersions of panels a and b, with colored markers superimposed to indicate the momentum-energy positions of VB1, VB2, and VB3 obtained from the MDC analysis. A small shift of VB1 and VB2 of approximately $0.03\,\mathrm{Å}^{-1}$ toward positive k_x values relative to VB3, whose maximum coincides with the BZ center, is observed when tracing the bands at photon energies of 77 and 83 eV (see Fig. 3.2c). The origin of this shift is nonphysical and likely stems from uncertainties in determining the peak positions in the MDC analysis, as well as in identifying the exact center of the BZ. In particular, in addition to the broadening and weak intensity of the bands, the determination of the BZ center is affected by slight sample misalignment, since the crystal surface is never perfectly flat, resulting in deviations from ideal normal emission. These effects lead to uncertainties comparable to the magnitude of the observed shift in the extracted band positions. Nevertheless, the close overlap of the extracted dispersions at different photon energies indicates weak out-of-plane dispersion in this energy window, consistent with the k_z-dependent behavior shown in Fig 3.1d. VB2 and VB3 display nearly linear dispersions over an energy range exceeding 1 eV, while VB1 is significantly flatter and well described by a parabolic dispersion. Linear fits yield velocities for VB3 ranging from $\sim 0.9 \times 10^6$ m/s along k_x to $\sim 1.3 \times 10^6$ m/s along k_y; for VB2, the velocities are about a factor of two

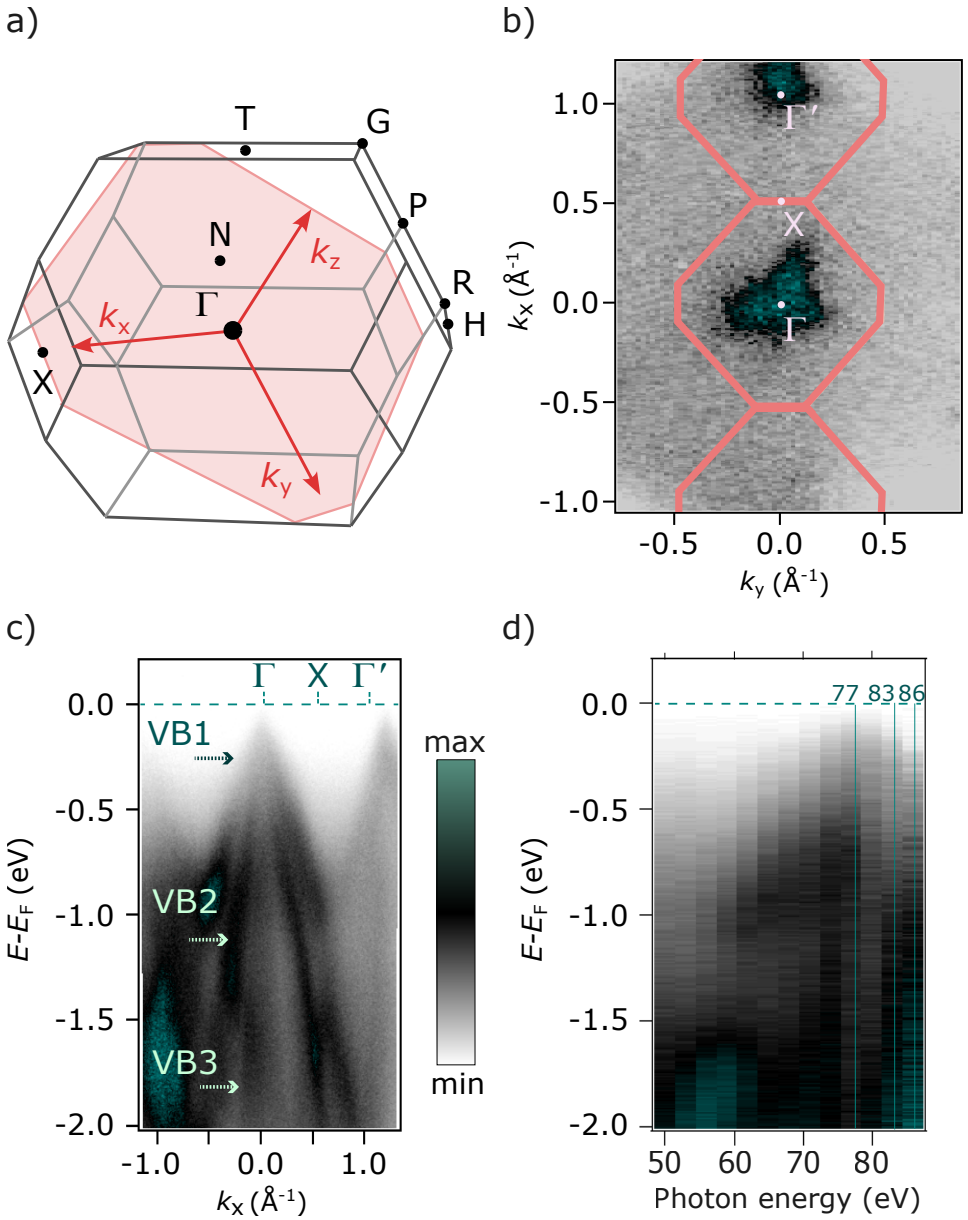

Figure 3.1: (a) The orientation of the electron-wavevector directions k_x, k_y, k_z sampled in the ARPES measurements with respect to the first Brillouin zone (BZ). (b) Constant-energy map acquired at $E - E_F = -0.2\,\text{eV}$ using a photon energy of 72.5 eV. The Γ, X, and Γ′ points are indicated together with the boundary of the first BZ for $k_z = 0\,\text{Å}^{-1}$, corresponding to the red plane in panel (a). (c) Valence-band dispersion measured at a photon energy of 72.5 eV along k_x. The three bands forming the highest valence-band manifold are labeled VB1, VB2, and VB3, respectively, in agreement with the notation used in Sec. 1.2.4. (d) Photon-energy dependence map between 50 and 86 eV of the ARPES intensity constructed from energy distribution curves collected at the Γ point.

smaller, $\sim 0.5 \times 10^6\,\mathrm{m/s}$ along both k_x and k_y. These band velocities are large and comparable to those reported for graphene [106] and Dirac semimetals [107]. VB1 yields effective masses of $\sim 1.09\,m_0$ and $\sim 1.06\,m_0$ along k_x and k_y, respectively. These values are larger than the one estimated using the Kildal and the Limpijumnong-Lambrecht models (Table 1.2) by factors of approximately 1.7 and 3.7, respectively. Such discrepancies are reasonable as the calculations rely on a limited number of bands to reproduce the electronic band structure and their estimates account only for states within a very narrow region around the Γ point. In contrast, the experimental analysis probes valence bands along the full ΓX direction, and the parabolic fit includes states even far from the BZ center. Refined calculations including a larger number of bands would therefore be required to obtain more accurate effective masses. Eventually, it is worth to note that the close agreement of velocities and masses along the two in-plane directions indicates an approximately isotropic valence-band character within the investigated cleavage plane.

The band dispersion measured by ARPES is overall well reproduced by the 8-band $\mathbf{k}\cdot\mathbf{p}$ model along both k_x (Fig. 3.3a) and k_y (Fig. 3.3b). The band positions extracted from the ARPES analysis are shifted to higher energies to account for the offset between the Fermi level and the valence-band maximum, which is approximately 0.18 eV. The VB1 and VB2 band positions measured at photon energies of 77 and 83 eV are also shifted along k_x by $0.03\,\mathrm{Å}^{-1}$ towards the BZ center. Along the k_x direction, the parabolic dispersion of VB1 and the nearly linear dispersion of VB3 are well captured by the model. In contrast, the nearly linear dispersion of VB2 at large k_x and k_y values is less accurately described, as the model predicts a parabolic behavior. Moreover, the very high velocity of VB3 observed experimentally along k_y is not fully reproduced by the calculations, which predict highly dispersive bands along this direction but with a smaller velocity. Finally, no experimental evidence is found for the abrupt change in the slope of VB1 along k_y close to the Γ point predicted in the estimation of the band structure. The description of the probed electronic states of $CdGeAs_2$ concludes here. The 8-band $\mathbf{k}\cdot\mathbf{p}$ model is validated through comparison with ARPES spectra and is now used to calculate the DSP generated in the CB via optical orientation.

3.2. Optical orientation in $CdGeAs_2$

Interband optical transitions from VB1, VB2, and VB3 to CB are allowed by dipole selection rules depending on whether the light polarization, expressed through the electric field vector $\mathbf{E}$, is parallel or perpendicular to the c axis [77], [78]. In particular, all the transitions are allowed for $\mathbf{E} \perp c$, whereas the transitions VB1→CB and VB3→CB are

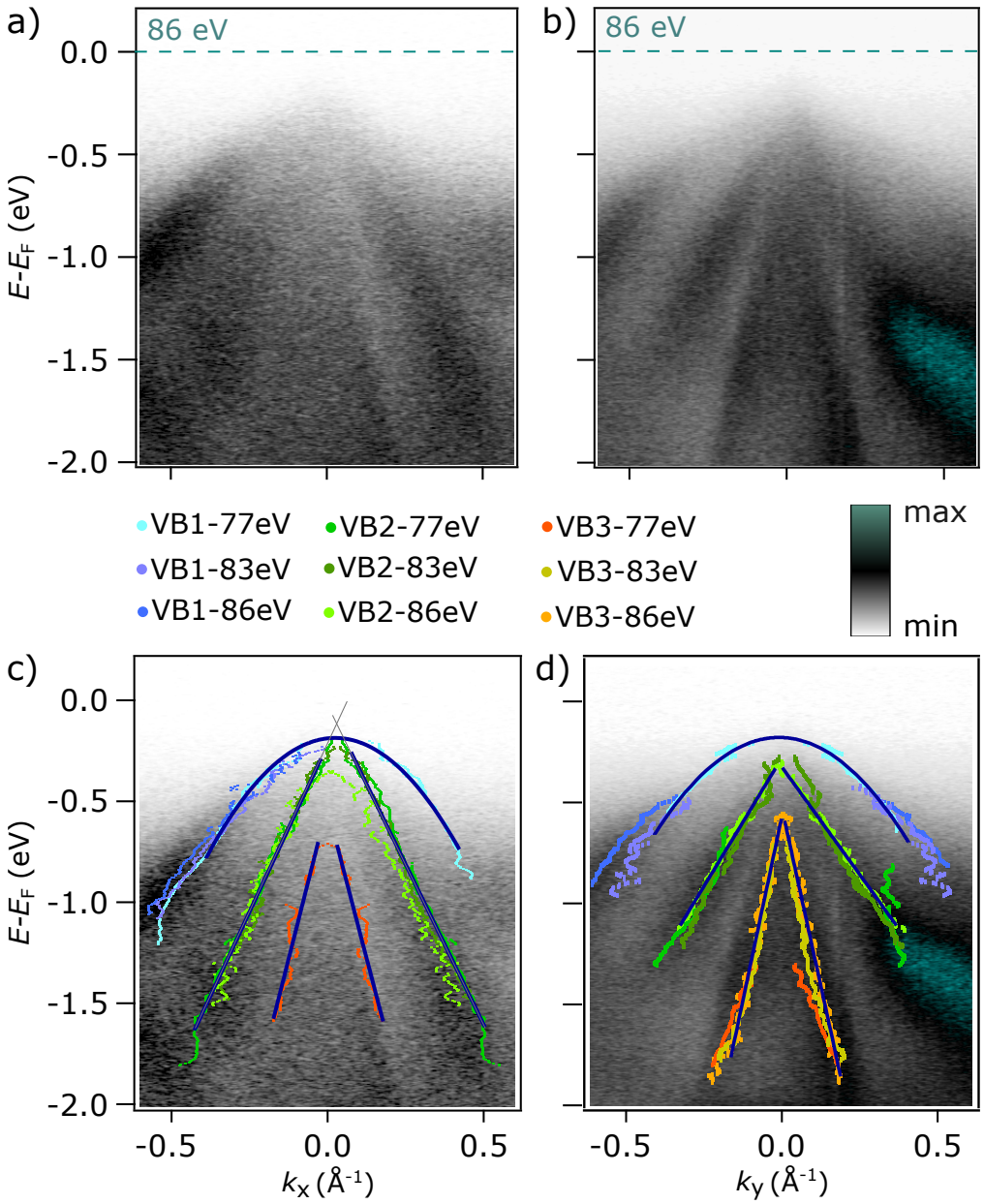

Figure 3.2: Valence-band dispersion measured with a photon energy of 86 eV along (a) k_x and (b) k_y. Panels (c) and (d) reproduce the very same band dispersions, with colored markers indicating the momentum-energy positions of VB1, VB2, and VB3. These are extracted as the peak positions of the momentum distribution curves integrated over a 25 meV energy window between -1.75 and -0.25 eV. Different colors correspond to band positions obtained from data sets acquired at photon energies of 77, 83, and 86 eV. Dark-blue lines indicate the best fits to the band positions: VB1 is well described by a parabolic dispersion, whereas VB2 and VB3 exhibit nearly linear dispersions with large band velocities.

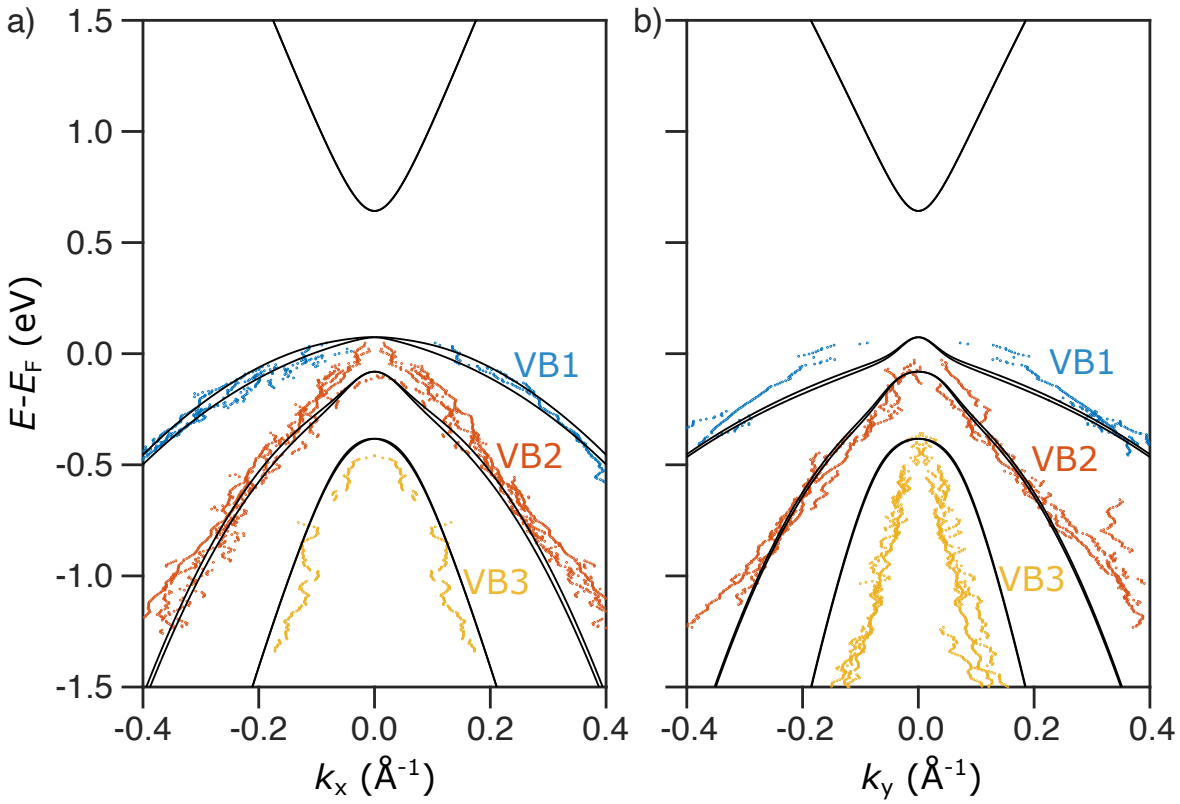

Figure 3.3: Comparison between the band dispersion measured by ARPES and calculated using the 8-band $\mathbf{k}\cdot\mathbf{p}$ model proposed in Sec. 1.2.4, of VB1 (blue), VB2 (orange), and VB3 (yellow) bands along the (a) k_x and (b) k_y electron wavevector directions.

allowed and VB2→CB is forbidden for $\mathbf{E} \parallel c$ at the Γ point. Before implementing the fully linear response theory to estimate the DSP spectrum, we first provide a simplified picture of optical orientation in $CdGeAs_2$. We consider only optical transitions at the Γ point and circularly polarized light with $\mathbf{E} \perp c$, *i.e.*, with the light wavevector parallel to the c axis, thus having all the excitation channels permitted. Fig. 3.4 presents transitions with the relative rates from the three VBs to the CB for both σ^+ and σ^- polarizations that satisfy the dipole selection rules depicted in Eq. (1.48). The rates are calculated using the FGR (details in Appendix A) and result:

$$W_{\mathrm{VB1,CB}} \propto |AB|^2 \,;\, W_{\mathrm{VB2,CB}} \propto 1;$$

$$W_{\mathrm{VB3,CB}} \propto |CD|^2 \,.$$

The values are normalized with respect to $W_{\mathrm{VB2,CB}}$. In $CdGeAs_2$, $|AB|^2 \simeq 1/7$ and $|CD|^2 \simeq 6/7$. By illuminating with σ^+-polarized light, dipole selection rules ($\Delta m_j = +1$) imply:

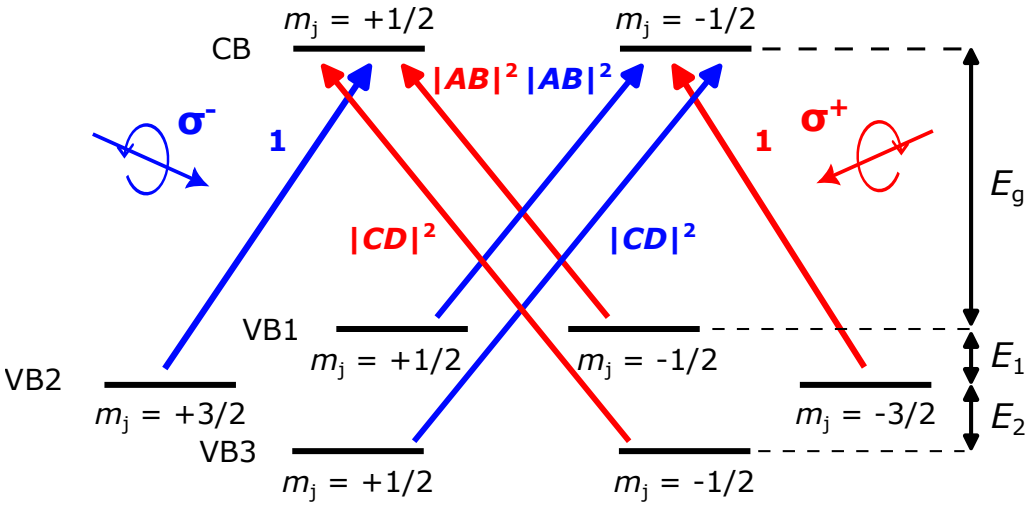

Figure 3.4: Scheme of the energy levels at the Γ point of $CdGeAs_2$. The conduction band (CB) is separated from the first valence band (VB1) by the band gap E_g. The VB1 band and the second valence bands (VB2) are separated by the energy splitting E_1, while VB2 and the third valence band (VB3) are separated by the energy splitting E_2. The degenerate energy levels are labelled based on their m_j value. The transitions allowed by dipole selection rules illuminating with σ^+- and σ^--polarized light are represented in red and blue, respectively. The transition rates are reported close to the arrows, being $|AB|^2 \simeq 1/7$ and $|CD|^2 \simeq 6/7$.

- When $0 \leq \hbar\omega - E_g < E_1$:
  Only electrons from the VB1 ($m_j = -\frac{1}{2}$) are promoted to the CB ($m_j = +\frac{1}{2}$). As a consequence, a spin population with $m_j = +\frac{1}{2}$ is generated in the CB with:

$$\mathrm{DSP} = 100\%,$$

- When $E_1 \leq \hbar\omega - E_g < E_2$:
  For each electron promoted from the VB1 to the CB, seven electrons are excited from the VB2 ($m_j = -\frac{3}{2}$) to the CB ($m_j = -\frac{1}{2}$). As a consequence, a spin population with $m_j = -\frac{1}{2}$ is generated with:

$$\mathrm{DSP} \simeq \frac{\frac{1}{7} - 1}{\frac{1}{7} + 1} = -75\%,$$

- When $\hbar\omega - E_g \geq E_2$:
  For each electron promoted from the VB1 to the CB, other six electrons are promoted from the VB3 ($m_j = -\frac{1}{2}$) to the CB ($m_j = +\frac{1}{2}$). In this regime, the electron

densities in the CB with $m_\mathrm{j} = \pm\frac{1}{2}$ are equal, resulting in zero spin polarization:

$$\mathrm{DSP} = \frac{\frac{1}{7} + \frac{6}{7} - 1}{\frac{1}{7} + \frac{6}{7} + 1} = 0\%.$$

The DSP is calculated following Eq. (1.51) and its sign changes by illuminating with σ^--polarized light. Accordingly, the DSP is expected to reach 100% as the photon energy approaches the band gap. Moreover, it reverses sign upon the onset of excitations from VB2, indicating the injection of electrons with opposite spin polarization between VB1 and VB2, and reaches an absolute value as high as 75%. Finally, when excitations from VB3 occur, electrons with spin-up and spin-down character compensate each other, and the DSP vanishes.

We now present the calculation of $\dot{\mathbf{S}}$, $\dot{n}$, and the DSP as functions of the photon energy within the fully linear response theory, using Eqs. (1.52) - (1.56). The explored photon-energy range spans from the band gap up to 1.3 eV. The only direct optical transitions involved in this energy range originate from VB1, VB2, and VB3 and terminate in the first CB around the Γ point [77]. The energy onsets of these transitions are $E_\mathrm{VB1} = 0.571\,\mathrm{eV}$, $E_\mathrm{VB2} = 0.720\,\mathrm{eV}$, and $E_\mathrm{VB3} = 1.025\,\mathrm{eV}$. Phonon-assisted indirect optical transitions from VB1 and VB2 to the CB minimum at the X point of the BZ also occur within this energy range, with estimated onset energies of $E^\mathrm{X}_\mathrm{VB1} = 1.05\,\mathrm{eV}$ and $E^\mathrm{X}_\mathrm{VB2} = 1.2\,\mathrm{eV}$. However, these processes are neglected here as they are weaker than the direct transitions and any possible contribution is expected to be hidden. Moreover, their inclusion would be computationally demanding because of explicit treatment of phonon states [67].

In a tetragonal system, the cartesian coordinates x, y, and z refer to the a, b, and c axes in Fig. 1.5a, respectively. Figs. 3.5a - 3.5d present the coefficients of the carrier-injection tensor $\xi^{xx}(\omega)$, $\xi^{yy}(\omega)$, and $\xi^{zz}(\omega)$ as functions of the photon energy. These are the only nonzero coefficients and $\xi^{zz}(\omega)$ no more equals $\xi^{xx}(\omega)$ and $\xi^{yy}(\omega)$ (Fig. 3.5a), reflecting the presence of anisotropy during the light absorption process. In particular, ξ^{zz} is higher compared to $\xi^{xx}(\omega)$, which equals $\xi^{yy}(\omega)$, indicating, according to Eq. (1.55), a higher $\dot{n}$ when an electric-field component is aligned along the z axis. Specifically, when σ^+-polarized light with wavevector $\mathbf{k}_\mathrm{l}$ forming an angle ϑ with the z axis is absorbed, the carrier-injection rate is equal to:

$$\mathbf{k}_\mathrm{l} \angle^{\vartheta} z \longrightarrow \dot{n}_\vartheta = [\xi^{xx}(\omega)(\cos^2\vartheta + 1) + \xi^{zz}(\omega)\sin^2\vartheta]|E_0|^2/2. \tag{3.1}$$

Thus, when $\mathbf{k}_\mathrm{l}$ is parallel or perpendicular to the z axis, one finds:

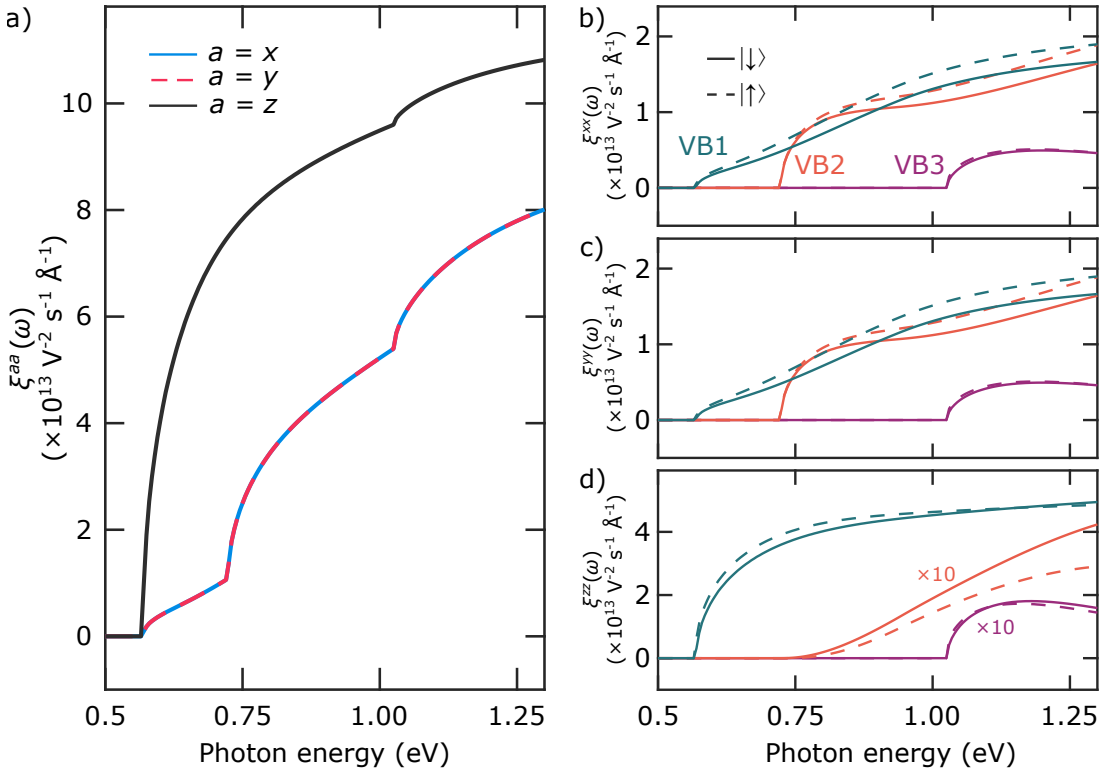

Figure 3.5: (a) The coefficients $\xi^{xx}(\omega)$ (azure), $\xi^{yy}(\omega)$ (pink), and $\xi^{zz}(\omega)$ (black) of the carrier-injection tensor calculated for $CdGeAs_2$. Decomposition of (b) $\xi^{xx}(\omega)$, (c) $\zeta^{yy}(\omega)$, and (d) $\zeta^{zz}(\omega)$ in single contributions from VB1 (green-blue), VB2 (orange), and VB3 (violet) bands.

$$\mathbf{k}_\mathrm{l} \parallel z \longrightarrow \dot{n}_\parallel = \xi^{xx}(\omega)|E_0|^2, \tag{3.2a}$$

$$\mathbf{k}_\mathrm{l} \perp z \longrightarrow \dot{n}_\perp = [\xi^{xx}(\omega) + \xi^{zz}(\omega)]|E_0|^2/2. \tag{3.2b}$$

Therefore, $\dot{n}_\perp > \dot{n}_\vartheta > \dot{n}_\parallel$ since $\xi^{zz}(\omega) > \xi^{xx}(\omega)$. This relation holds across the entire photon-energy range, as both $\xi^{xx}(\omega)$ and $\xi^{zz}(\omega)$ increase with photon energy while preserving $\xi^{zz}(\omega) > \xi^{xx}(\omega)$. Figs. 3.5b - 3.5d present the decomposition of $\xi^{xx}(\omega)$, $\xi^{yy}(\omega)$, and $\xi^{zz}(\omega)$ into individual contributions from VB1, VB2, and VB3. The VB1→CB transition dominates in $\xi^{zz}(\omega)$ (Fig. 3.5d) over the VB2→CB and VB3→CB transitions. In contrast, the latter are more pronounced in $\xi^{xx}(\omega)$ (Fig. 3.5b) and $\xi^{yy}(\omega)$ (Fig. 3.5c). The zero contribution from VB2 at its onset in $\xi^{zz}(\omega)$ shows that these transitions are forbidden for $E \parallel z$ (the c axis) at the Γ point by dipole selection rules.

We now proceed to discuss $\dot{\mathbf{S}}$. In a tetragonal system, only two independent coefficients of the spin-injection pseudotensor, namely $\zeta^{xyz}(\omega)$ and $\zeta^{zxy}(\omega)$, exist and both are purely

imaginary. Moreover, there are six nonzero coefficients, given by:

$$\zeta^{xyz}(\omega) = \zeta^{yzx}(\omega) = -\zeta^{xzy}(\omega) = -\zeta^{yxz}(\omega),$$

$$\zeta^{zxy}(\omega) = -\zeta^{zyx}(\omega).$$

According to Eq. (1.52), $\zeta^{xyz}(\omega)$, $\zeta^{yzx}(\omega)$, and $\zeta^{zxy}(\omega)$ describe the x-, y-, and z-components of $\dot{\mathbf{S}}$, respectively. The absence of additional terms in the spin-injection pseudotensor beyond the six listed above implies that the spin-injection rate components are generated only by orthogonal electric-field components, accordingly those lying in the yz, zx, and xy planes, respectively. Thus, when light propagates along the x, y, or z axis, $\dot{\mathbf{S}}$ has a single nonzero component, as in a cubic system, and is aligned with $\mathbf{k}_\mathrm{l}$. Specifically, for σ^+-polarized light it holds:

$$\begin{aligned} \mathbf{k}_\mathrm{l} \parallel x \longrightarrow \dot{\mathbf{S}} &= (\dot{S}^x, 0, 0), \\ \dot{S}^x &= i\,\zeta^{xyz}(\omega)|E_0|^2, \end{aligned} \tag{3.3a}$$

$$\begin{aligned} \mathbf{k}_\mathrm{l} \parallel y \longrightarrow \dot{\mathbf{S}} &= (0, \dot{S}^y, 0), \\ \dot{S}^y &= i\,\zeta^{xyz}(\omega)|E_0|^2, \end{aligned} \tag{3.3b}$$

$$\begin{aligned} \mathbf{k}_\mathrm{l} \parallel z \longrightarrow \dot{\mathbf{S}} &= (0, 0, \dot{S}^z), \\ \dot{S}^z &= i\,\zeta^{zxy}(\omega)|E_0|^2. \end{aligned} \tag{3.3c}$$

Moreover, the symmetry properties in the xy plane resemble those of cubic systems. Consequently, for light propagating from any direction in the xy plane, $\dot{\mathbf{S}}$ remains fully polarized along $\mathbf{k}_\mathrm{l}$, with $\dot{S} = i\,\zeta^{xyz}(\omega)|E_0|^2$. In contrast, when σ^+-polarized light with $\mathbf{k}_\mathrm{l}$ forming an angle ϑ with the z axis in the xz plane is absorbed, the spin-injection rate is equal to:

$$\begin{aligned} \mathbf{k}_\mathrm{l} \measuredangle^{\vartheta}_{xz} z \longrightarrow \dot{\mathbf{S}}_\vartheta &= (\dot{S}^x, 0, \dot{S}^z), \\ \dot{S}^x &= i\zeta^{xyz}(\omega)|E_0|^2 \sin\vartheta, \\ \dot{S}^z &= i\zeta^{zxy}(\omega)|E_0|^2 \cos\vartheta. \end{aligned} \tag{3.4}$$

When the light wavevector forms an angle ϑ with the z axis in the yz plane, the spin-injection rate is equal to:

$$\begin{aligned} \mathbf{k}_\mathrm{l} \angle_{yz}^{\vartheta} z \longrightarrow \dot{\mathbf{S}}_\vartheta &= (0, \dot{S}^y, \dot{S}^z), \\ \dot{S}^y &= i\zeta^{xyz}(\omega)|E_0|^2 \sin\vartheta, \\ \dot{S}^z &= i\zeta^{zxy}(\omega)|E_0|^2 \cos\vartheta. \end{aligned} \tag{3.5}$$

Therefore, when $\mathbf{k}_\mathrm{l}$ has a component along the z axis, as in Eqs. (3.4) and (3.5), the difference between $\zeta^{xyz}(\omega)$ and $\zeta^{zxy}(\omega)$ leads to a misalignment of $\dot{\mathbf{S}}$ with respect to $\mathbf{k}_\mathrm{l}$. For a generic light wavevector with directional angles ϑ and φ, the electric field for $\sigma^{\pm}$-polarized light is:

$$\mathbf{E}^{\pm}(\omega) = \frac{E_0}{\sqrt{2}} \begin{pmatrix} \cos\vartheta\cos\varphi \mp i\sin\varphi \\ \cos\vartheta\sin\varphi \pm i\cos\varphi \\ -\sin\vartheta \end{pmatrix},$$

and the spin-injection rate results:

$$\dot{\mathbf{S}}^{\pm}_{\vartheta,\varphi} = \pm i|E_0|^2 \begin{pmatrix} \zeta^{xyz}(\omega)\sin\vartheta\cos\varphi \\ \zeta^{xyz}(\omega)\sin\vartheta\sin\varphi \\ \zeta^{zxy}(\omega)\cos\vartheta \end{pmatrix}. \tag{3.6}$$

Therefore, $\dot{\mathbf{S}}$ is reversed for σ^+ and σ^- polarizations, regardless of the orientation of the incident beam with respect to the crystallographic axes. Remarkably, by expressing the light wavevector as:

$$\mathbf{k}_\mathrm{l} = \begin{pmatrix} \sin\vartheta\cos\varphi \\ \sin\vartheta\sin\varphi \\ \cos\vartheta \end{pmatrix},$$

the misalignment angle β between $\mathbf{k}_\mathrm{l}$ and $\dot{\mathbf{S}}$ is given by:

$$\cos\beta = \frac{\dot{\mathbf{S}}^{\pm}_{\vartheta,\varphi} \cdot \mathbf{k}_\mathrm{l}}{|\dot{\mathbf{S}}^{\pm}_{\vartheta,\varphi}||\mathbf{k}_\mathrm{l}|} = \mp \frac{\mathrm{Im}[\zeta^{xyz}(\omega)]\sin^2\vartheta + \mathrm{Im}[\zeta^{zxy}(\omega)]\cos^2\vartheta}{\sqrt{\mathrm{Im}^2[\zeta^{xyz}(\omega)]\sin^2\vartheta + \mathrm{Im}^2[\zeta^{zxy}(\omega)]\cos^2\vartheta}}. \tag{3.7}$$

Figs. 3.6a - 3.6d present the imaginary part of the coefficients of the spin-injection pseudotensor $\zeta^{xyz}(\omega)$, $\zeta^{yzx}(\omega)$, and $\zeta^{zxy}(\omega)$ as functions of the photon energy. The $\mathrm{Im}[\zeta^{zxy}(\omega)]$ differs from $\mathrm{Im}[\zeta^{xyz}(\omega)]$, which equals $\mathrm{Im}[\zeta^{yzx}(\omega)]$ (Fig. 3.6a). The $\mathrm{Im}[\zeta^{xyz}(\omega)]$ increases sharply above the band gap and remains positive over the entire photon-energy range.

Then, it decreases abruptly above 1.025 eV, corresponding to the onset of transitions from VB3. In contrast, the $\mathrm{Im}[\zeta^{zxy}(\omega)]$ is smaller and negative from the band gap until 0.72 eV, that corresponds to the onset of absorption from VB2. Beyond this value, the $\mathrm{Im}[\zeta^{zxy}(\omega)]$ strongly increases and changes sign, reaching a maximum at approximately 1 eV. Above 1.025 eV, it decreases rapidly while remaining positive. The decomposition of $\mathrm{Im}[\zeta^{xyz}(\omega)]$ (Fig. 3.6b) into individual contributions from VB1, VB2, and VB3 confirms strong generation from VB1 and a nearly negligible from VB2. The zero spin injection from VB2 at its onset is because these transitions are forbidden for $\mathbf{E} \parallel z$. As a result, when $\mathbf{k}_\mathrm{l} \perp z$, only the component of the electric field perpendicular to the z axis is absorbed as the light were linearly polarized, and no angular momentum is transferred. Increasing the photon energy, the transitions involve electronic states outside the Γ point, where reduced symmetry weaken the dipole selection rules, yielding a weak spin-injection contribution. Moreover, the decrease observed at 1.025 eV is attributed to a spin-injection contribution from VB3 with opposite sign compared to that from VB1. The decomposition of $\mathrm{Im}[\zeta^{zxy}(\omega)]$ (Fig. 3.6d) confirms a weak and negative contribution to spin injection from VB1, while a large and positive from VB2 and a negative from VB3. Moreover, the sign reversal and enhanced VB1 contribution above 0.82 eV indicate that the maximum spin injection arises from combined VB1 and VB2 transitions rather than from VB2 alone. Finally, we note that the contribution from VB2 progressively vanishes for photon energies above 1.025 eV, and electrons with opposite polarizations are transferred from VB1 and VB3 partially canceling each other.

The injection rates $\dot{n}$ and $\dot{\mathbf{S}}$ can be calculated from $\xi^{xx}(\omega)$, $\xi^{zz}(\omega)$, $\zeta^{xyx}(\omega)$, and $\zeta^{zxy}(\omega)$ using Eqs. (3.1) and (3.6) for a specific light orientation. The DSP is then obtained from Eq. (1.54). For σ^+-polarized light propagating parallel and perpendicular to the z axis, $\dot{\mathbf{S}}$ is aligned with $\mathbf{k}_\mathrm{l}$ according to Eqs.(3.3), and the DSP is given by:

$$\mathbf{k}_\mathrm{l} \parallel z \longrightarrow \mathrm{DSP} = -\mathrm{Im}[\zeta^{zxy}(\omega)]/\xi^{xx}(\omega), \tag{3.8a}$$

$$\mathbf{k}_\mathrm{l} \perp z \longrightarrow \mathrm{DSP} = -2\,\mathrm{Im}[\zeta^{xyz}(\omega)]/[\xi^{xx}(\omega) + \xi^{zz}(\omega)]. \tag{3.8b}$$

The signs in Eqs. (3.8) are reversed for σ^- polarization. Fig. 3.7 presents the DSP spectra for σ^+-polarized light with $\mathbf{k}_\mathrm{l} \parallel x$, $\mathbf{k}_\mathrm{l} \parallel y$, and $\mathbf{k}_\mathrm{l} \parallel z$. For $\mathbf{k}_\mathrm{l} \parallel z$, the DSP spectrum is well explained by the simplified picture of optical orientation introduced at the beginning of this section, in which only transitions at the Γ point are considered. The DSP is 100% for excitations resonant with the band gap, demonstrating the possibility of injecting very high spin polarization via optical orientation. As the photon energy increases, the DSP

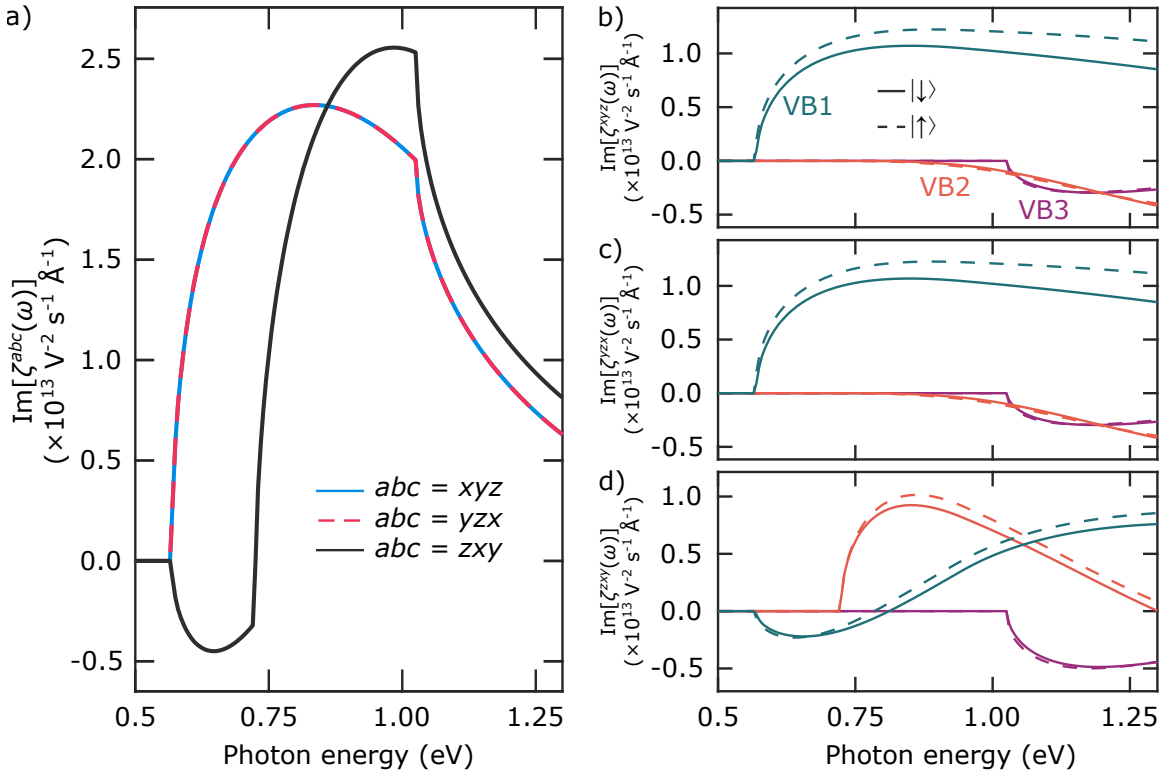

Figure 3.6: (a) The imaginary part of the coefficients $\zeta^{xyz}(\omega)$ (azure), $\zeta^{yzx}(\omega)$ (pink), and $\zeta^{zxy}(\omega)$ (black) of the spin-injection pseudotensor calculated for $CdGeAs_2$. Decomposition of (b) $\mathrm{Im}[\zeta^{xyz}(\omega)]$, (c) $\mathrm{Im}[\zeta^{yzx}(\omega)]$, and (d) $\mathrm{Im}[\zeta^{zxy}(\omega)]$ in single contributions from VB1 (green-blue), VB2 (orange), and VB3 (violet) bands.

rapidly decreases because of transitions outside the Γ point. At 0.72 eV, electrons with opposite polarization are efficiently excited from VB2, causing the DSP to change sign and reach values as low as −55%. This value is slightly overestimated by the simplified picture, although it correctly captures the sign reversal. The DSP remains below −45% up to 1.025 eV, where it sharply increases due to transitions from VB3, reaching approximately −10% at the upper end of the explored photon-energy range. Even though it occurs at photon energies far above the band gap, this final reduction of |DSP| is qualitatively reproduced by the simplified description, despite with an incorrect assignment of the relative contributions of the transitions. Specifically, the model attributes the decay to compensation between the opposite spin polarizations from VB3 and VB1 and that from VB2. In contrast, Fig. 3.6d shows that the decay is mainly associated with opposite spin polarizations from VB3 and VB1, while VB2 contributes only marginally.

The DSP spectra for $\mathbf{k}_\mathrm{l} \parallel x$ and $\mathbf{k}_\mathrm{l} \parallel y$ have not a simple interpretation. The DSP remains negative over the entire photon-energy range, reaching a maximum absolute value of approximately 56% when the photon energy is resonant with the band gap, although only

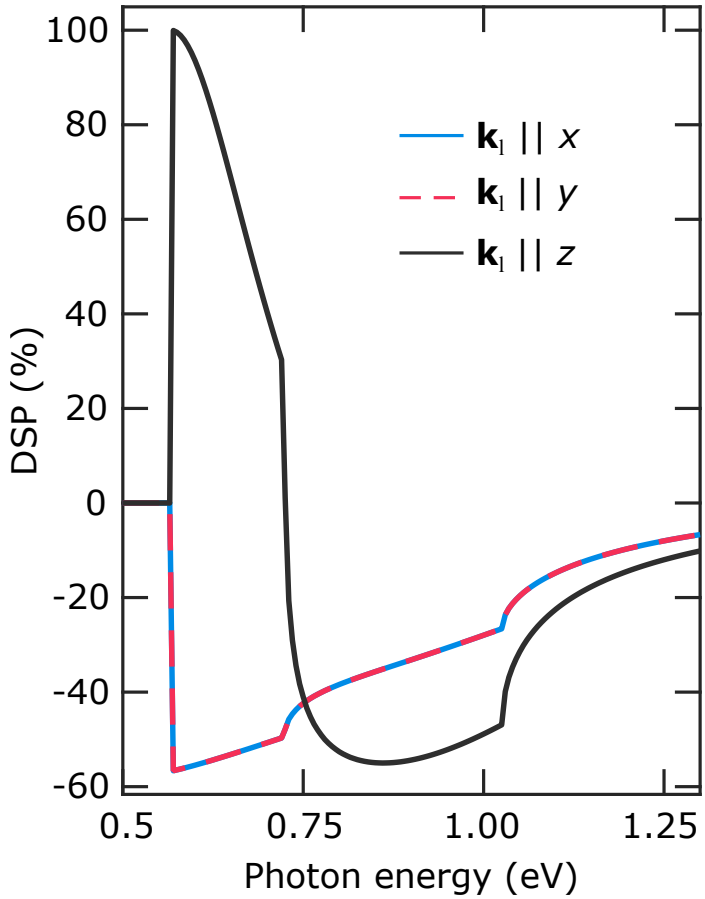

Figure 3.7: The photon-energy dependence of the degree of spin polarization (DSP) in $CdGeAs_2$ generated by illuminating with σ^+-polarized light with wavevector $\mathbf{k}_l$ parallel to the x (azure), y (pink), and z (black) axes, which correspond to the a, b, and c axes in Fig. 1.5a.

transitions from VB1 are involved. This peculiar behavior stems from the anisotropic absorption of light with electric-field components parallel and perpendicular to the z axis. Consequently, even if the incident beam is purely circularly polarized, the absorbed field becomes a mixture of circular and linear polarizations. Therefore, the DSP injected into the CB remains below 100%, despite the transitions involving only VB1. As the photon energy increases, the absolute value of the DSP gradually decreases due to transitions outside the Γ point and opposite contributions from VB2 and VB3. The minimum absolute value is reached at 1.3 eV and is approximately 7%. This concludes the part regarding optical orientation in $CdGeAs_2$. I now turn to the characterization of optically induced spin-to-charge conversion in $CdGeAs_2$.

3.3. Spin-to-charge conversion in $CdGeAs_2$

In this section, spin-to-charge conversion properties of $CdGeAs_2$ are investigated by measuring the photon-energy dependence of the ISHE signal, which originates from spin-dependent scattering of optically injected spin-polarized electrons. Fig. 3.8a illustrates the experimental geometry. The ISHE-induced voltage drop ΔV_{ISHE} is measured under open-circuit conditions across two Au(200 nm)/Ti(7 nm) electrodes evaporated at the edges of a $4 \times 2 \times 1\,\mathrm{mm}^3$ $CdGeAs_2$ crystal. In the investigated sample, the x and y axes form an angle $\eta \simeq 37°$ with respect to the crystallographic axes corresponding to the k_{x} and k_{y} directions probed in the ARPES measurements, respectively. These axes are the $[1\bar{1}0]$ and $[c/a,\ c/a,\ -a/c]$ directions expressed in the basis of the direct lattice vectors. Whereas, the z axis is parallel to the crystallographic axis corresponding to the k_{z} direction, which is the [112]. Their unit vectors are:

$$\tilde{\mathbf{x}} = \left(\frac{1}{\sqrt{2}}, -\frac{1}{\sqrt{2}}, 0\right), \quad \tilde{\mathbf{y}} = \frac{1}{\gamma'}\left(c, c, -a\right), \quad \tilde{\mathbf{z}} = \frac{1}{\gamma'}\left(\frac{a}{\sqrt{2}}, \frac{a}{\sqrt{2}}, \frac{2c}{\sqrt{2}}\right), \tag{3.9}$$

where $\gamma' = \sqrt{2c^2 + a^2}$. The orientation is sketched in Fig. 3.8b and verified by Laue diffraction.

The circularly polarized laser beam is focused onto the sample at a polar angle Θ with respect to the z axis in the xz plane. The photo-excited spin-polarized electrons diffuse within the crystal, giving rise to a spin current density $\mathbf{j}_{\mathrm{s}}$. Although diffusion in the bulk is isotropic, spin-polarized currents flowing in opposite directions within the xy plane generate ISHE contributions of opposite sign according to Eq. (1.61), which cancel each other. Owing to the breaking of symmetry at the surface along the out-of-plane direction, the only measurable component of the spin current density is that along the z axis. Consequently, $\mathbf{j}_{\mathrm{s}}$ can be regarded as having only a z-axis component. By contrast, the measured ΔV_{ISHE} probes a charge current density $\mathbf{j}$ flowing along the y axis because of the electrodes position on the crystal. Under these conditions, only the x-axis component of the spin polarization satisfies the ISHE geometry of Eq. (1.61) and can be detected.

Therefore, we evaluate the x-axis component of the spin-injection rate $\dot{\mathbf{S}}$ for σ^+-polarized light propagating at the polar angle Θ in the geometry of Fig. 3.8a. In this case, the electric field can be written as:

$$\mathbf{E}(\omega) = \frac{E_0}{\sqrt{2}}\left(\cos\Theta\,\mathbf{e}_{\mathrm{x}} + i\,\mathbf{e}_{\mathrm{y}} - \sin\Theta\,\mathbf{e}_{\mathrm{z}}\right).$$

where $\mathbf{e}_{\mathrm{x}}$, $\mathbf{e}_{\mathrm{y}}$, and $\mathbf{e}_{\mathrm{z}}$ are the unit vectors of the x, y, and z axes of Figs. 3.8a and 3.8b.

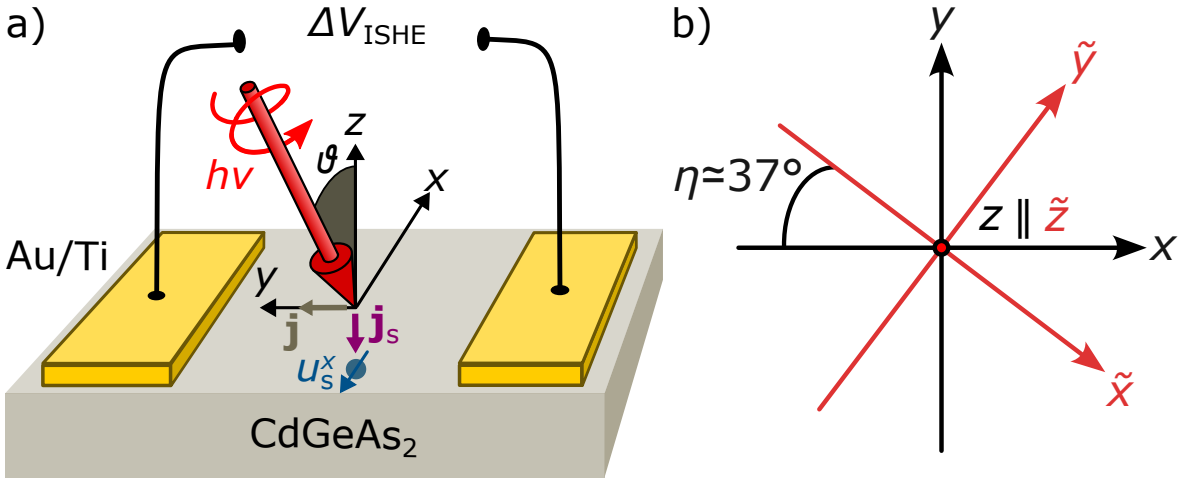

Figure 3.8: a) Sketch of the ISHE geometry. Two Au/Ti ohmic contacts are deposited on top of a $4 \times 2\,\mathrm{mm}^2$-wide and 1 mm-thick $CdGeAs_2$ sample. A circularly polarized light beam illuminates the sample at a polar angle Θ with respect to the normal in the xz plane. The u_s^x denotes the detected x-axis component of the spin-polarization unit vector, $\mathbf{j}_\mathrm{s}$ the spin current density, and $\mathbf{j}_\mathrm{c}$ the charge current density. b) The orientation of the ISHE geometry (black) with respect to the $\tilde{x}$, $\tilde{y}$ and $\tilde{z}$ axes (red), which correspond to the $[1\bar{1}0]$, $[c/a,\ c/a,\ -a/c]$ and [112] crystallographic directions, respectively. The angle $\eta \simeq 37°$ accounts for the in-plane alignment.

These can be expressed using $\tilde{\mathbf{x}}$, $\tilde{\mathbf{y}}$, and $\tilde{\mathbf{z}}$ as basis vectors, yielding:

$$\mathbf{e}_\mathrm{x} = \cos\eta\,\tilde{\mathbf{x}} + \sin\eta\,\tilde{\mathbf{y}};\ \mathbf{e}_\mathrm{y} = -\sin\eta\,\tilde{\mathbf{x}} + \cos\eta\,\tilde{\mathbf{y}};\ \mathbf{e}_\mathrm{z} = \tilde{\mathbf{z}}.$$

Nevertheless, the electric field $\mathbf{E}(\omega)$ must be expressed in the (a, b, c) coordinate system used for the DSP calculations in Sec. 3.2 to evaluate the spin-injection rate $\dot{\mathbf{S}}$ generated via optical orientation. Using the unit vectors in Eq. (3.9), we obtain:

$$\begin{aligned}\mathbf{E}(\omega) = E_0 \Bigg[&\left(\frac{\cos\eta\cos\Theta}{2} + \frac{c\sin\eta\cos\Theta}{\gamma'\sqrt{2}} - \frac{a\sin\Theta}{2\gamma'} - i\frac{\sin\eta}{2} + i\frac{c\cos\eta}{\gamma'\sqrt{2}} \right)\mathbf{a} \\ &+ \left(-\frac{\cos\eta\cos\Theta}{2} + \frac{c\sin\eta\cos\Theta}{\gamma'\sqrt{2}} - \frac{a\sin\Theta}{2\gamma'} + i\frac{\sin\eta}{2} + i\frac{c\cos\eta}{\gamma'\sqrt{2}} \right)\mathbf{b} \\ &+ \left(-\frac{a\sin\eta\cos\Theta}{\gamma'\sqrt{2}} - \frac{c\sin\Theta}{\gamma'} - i\frac{a\cos\eta}{\gamma'\sqrt{2}} \right)\mathbf{c} \Bigg],\end{aligned} \tag{3.10}$$

where $\mathbf{a}$, $\mathbf{b}$, and $\mathbf{c}$ are the unit vectors of the (a, b, c) coordinate system. The spin-injection rate $\dot{\mathbf{S}}$ is then evaluated within the fully linear response theory, using Eq. (1.52), and is given by:

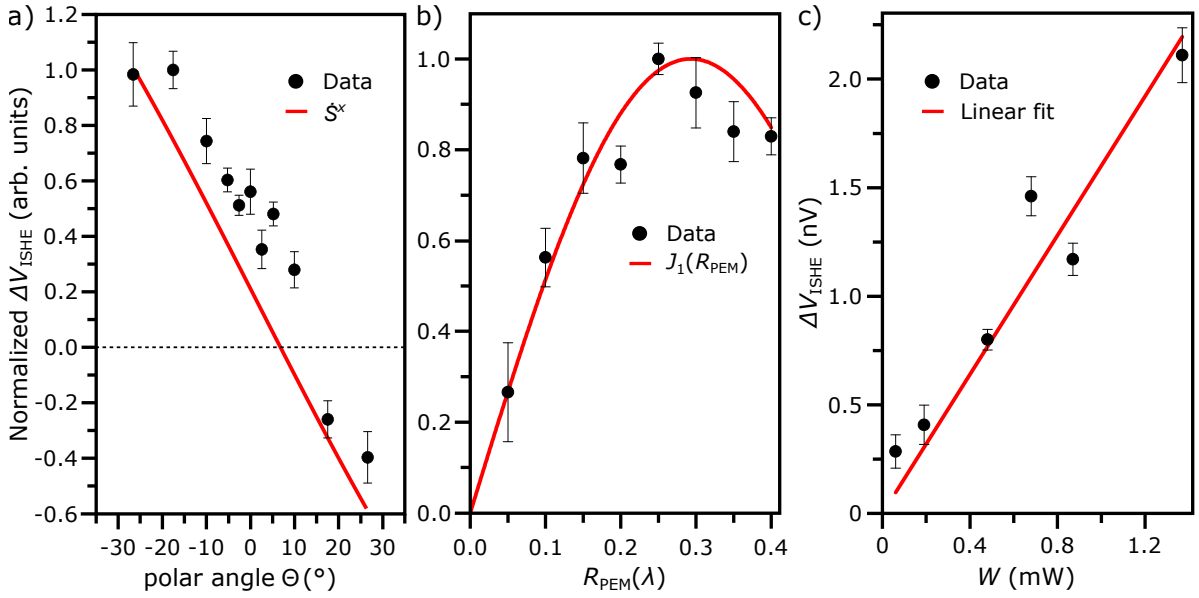

Figure 3.9: (a) ΔV_{ISHE} normalized to its maximum as a function of the polar angle Θ for $\hbar\omega = 0.8\,\mathrm{eV}$, $R_{\mathrm{PEM}} = 0.3\,\lambda$, and $W = 1.37\,\mathrm{mW}$. The solid red line represents the Θ-angle dependence of the spin-injection rate component $\dot{S}^x$ along the x axis in the geometry of Fig. 3.8a. (b) Dependence of ΔV_{ISHE} on the PEM retardation R_{PEM} for $\hbar\omega = 0.8\,\mathrm{eV}$, $\Theta = -27°$, and $W = 1.37\,\mathrm{mW}$. The solid red line represents the first-order Bessel function $J_1(\lambda)$. (c) ΔV_{ISHE} as a function of the incident optical power W for $\hbar\omega = 0.8\,\mathrm{eV}$, $R_{\mathrm{PEM}} = 0.3\,\lambda$, and $\Theta = -27°$. The solid red line represents a linear fit to the data.

$$
\begin{aligned}
\dot{\mathbf{S}} &= (\dot{S}^a, \dot{S}^b, \dot{S}^c),\\
\dot{S}^a &= \frac{i\zeta^{xyz}(\omega)}{\gamma'\sqrt{2}}(a\cos\Theta + \gamma'\sin\Theta\cos\eta + c\sqrt{2}\sin\Theta\sin\eta)|E_0|^2,\\
\dot{S}^b &= \frac{i\zeta^{xyz}(\omega)}{\gamma'\sqrt{2}}(a\cos\Theta - \gamma'\sin\Theta\cos\eta + c\sqrt{2}\sin\Theta\sin\eta)|E_0|^2,\\
\dot{S}^c &= \frac{i\zeta^{zxy}(\omega)}{\gamma'}(c\sqrt{2}\cos\Theta - a\sin\Theta\sin\eta)|E_0|^2,
\end{aligned}
\tag{3.11}
$$

Finally, the x-axis component of $\dot{\mathbf{S}}$ in the experimental geometry is then obtained by projecting the spin-injection rate onto the x axis, yielding:

$$
\begin{aligned}
\dot{S}^x = \dot{\mathbf{S}}\cdot\mathbf{e}_{\mathrm{x}} = \frac{i}{\gamma'^2}\Big\{ & ac\sqrt{2}\left[\zeta^{xyz}(\omega) - \zeta^{zxy}(\omega)\right]\cos\Theta\sin\eta + \gamma'^2\zeta^{xyz}(\omega)\sin\Theta\\
& + a^2\left[\zeta^{zxy}(\omega) - \zeta^{xyz}(\omega)\right]\sin\Theta\sin^2\eta\Big\}|E_0|^2.
\end{aligned}
\tag{3.12}
$$

The Eq. (3.12) represents the only measurable part of the spin-injection rate and is used

to interpret experimental results. The first is the dependence of the ISHE signal on the polar angle Θ (Fig. 3.9a) at photon energy $\hbar\omega = 0.8\,\mathrm{eV}$. The ΔV_{ISHE}, normalized to its maximum, is compared with $\dot{S}^x$, that is evaluated using Eq. (3.12) and the coefficients $\zeta^{xyz}(\omega)$ and $\zeta^{zxy}(\omega)$ calculated using the 8-band $\mathbf{k}\cdot\mathbf{p}$ model in Sec. 3.2. The ΔV_{ISHE} has a linear dependence with Θ, as $\dot{S}^x$, and changes sign for opposite angles beyond $|\Theta| > 15°$. This behavior is expected from Eq. (3.12) for small Θ angles, which is the relevant regime here as the maximum external angle is $\Theta = 27°$, corresponding to an internal propagation angle of $\Theta_{\mathrm{in}} \approx 8.5°$ given the refractive index $\upsilon \approx 3$ in $CdGeAs_2$ [108]. Interestingly, the signal crosses zero at a finite angle, *i.e.*, for $\Theta \neq 0$. This feature in the ISHE signal is observed because of the tetragonal symmetry of the system, as it is reproduced by Eq. (3.12) only when $\zeta^{xyz}(\omega)$ and $\zeta^{zxy}(\omega)$ are different. Contrary, $\zeta^{xyz}(\omega)$ is equal to $\zeta^{zxy}(\omega)$ for a cubic system and Eq. (3.12) predicts a single term proportional to $\sin\Theta$. Experimentally, the zero-crossing occurs between 10° and 17°, whereas $\dot{S}^x$ is zero for $\Theta \simeq 7°$. This difference is consistent with the $\approx 2°$ uncertainty in the experimental determination of Θ, together with additional few-degree inaccuracy in the estimate of the angle η. The consistency of the ISHE signal is further verified by measuring its dependence on the PEM retardation R_{PEM} (Fig. 3.9b), and on the incident optical power W (Fig. 3.9c) at photon energy $\hbar\omega = 0.8\,\mathrm{eV}$. As a function of R_{PEM}, the signal follows the first-order Bessel function $J_1(R_{\mathrm{PEM}})$, with a maximum near $\simeq 0.3\,\lambda$, consistent with the PEM control of circular polarization. Moreover, ΔV_{ISHE} scales linearly with W, reflecting the proportionality between the spin-injection rate and the photon flux within the linear response regime.

Along with $\dot{S}^x$, we evaluate the carrier-injection rate $\dot{n}$ using Eq. (1.55) in the geometry of Fig. 3.8a, and consequently using Eq. (1.54) the DSP^x, that is the degree of spin polarization of electrons with a measurable spin component. Moreover, the absorption coefficient can also be estimated from Eq. (1.57). By expressing the electric field through Eq. (3.10), the $\dot{n}$ results:

$$\begin{aligned}\dot{n} = \frac{1}{4}\Big\{3\xi^{xx}(\omega) + \xi^{zz}(\omega) + \frac{\xi^{xx}(\omega) - \xi^{zz}(\omega)}{\gamma'^2}\Big[\gamma'^2\cos(2\Theta) - 2a^2\cos^2\eta \\ - 2a^2\cos^2\Theta\,\sin^2\eta + 2a^2\sin^2\Theta - 2ac\sqrt{2}\,\sin\eta\,\sin(2\Theta)\Big]\Big\}|E_0|^2.\end{aligned} \tag{3.13}$$

At this stage, we define the effective spin-injection rate $\zeta = \mathrm{Re}\left(\dot{S}^x/|E_0|^2\right)$ and the effective carrier-injection rate $\xi = \dot{n}/|E_0|^2$ normalized to the beam intensity. Therefore, the measurable degree of spin polarization is given by $\mathrm{DSP}^x = \zeta/\xi$ and the absorption coefficient by $\alpha = \hbar\omega\xi/(2\upsilon c\varepsilon_0)$.

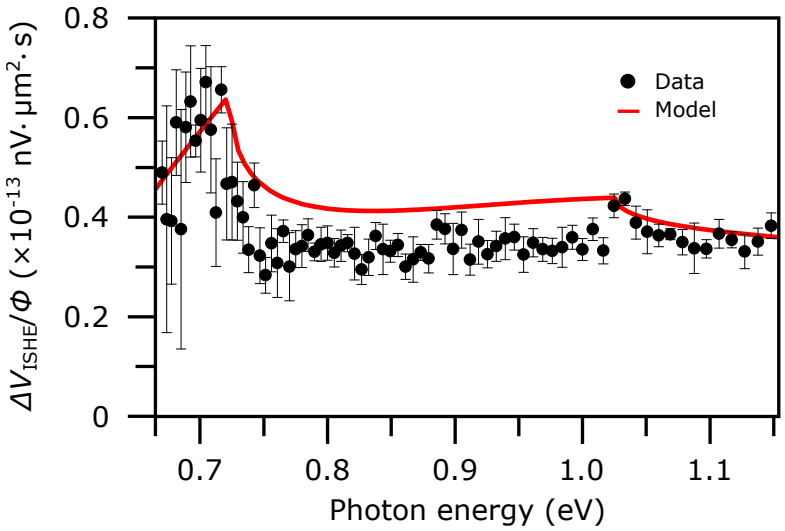

Figure 3.10: Photon-energy dependence of ΔV_{ISHE}, normalized to the incident photon flux Φ, for $\Theta = -27°$ and $R_{\mathrm{PEM}} = 0.3\,\lambda$. The solid red line shows the model prediction for $\Delta V_{\mathrm{ISHE}}/\Phi$ obtained from the right-hand side of Eq. (3.20).

Fig. 3.10 presents the photon-energy dependence of ΔV_{ISHE} normalized to photon flux Φ measured in the $0.65 - 1.15\,\mathrm{eV}$ range, for $R_{\mathrm{PEM}} = 0.3\,\lambda$ and $\Theta = -27°$. The W delivered on the sample varies within 50 and 1500 μW in the explored photon-energy range, and the photon flux is $\Phi = W/[\pi(\mathcal{D}/2)^2\hbar\omega]$, where $\mathcal{D}$ is the spot diameter on the sample (≈ 10 μm). The spectrum exhibits a pronounced peak near $\hbar\omega \simeq 0.72\,\mathrm{eV}$, followed by an almost constant signal up to $\simeq 1.15\,\mathrm{eV}$, with a weak feature at $\simeq 1.025\,\mathrm{eV}$. To gain insight into the photon-energy dependence of the normalized ISHE spectrum, we employ a 1D spin diffusion model for optically injected electrons. From Eq. (1.61), and considering the experimental configuration shown in Fig. 3.8a, the measured charge current density flowing along the y axis, j, is determined by the spin current density flowing along the z axis and polarized along the x axis, j_{s}^{x}, according to:

$$j(z) = \gamma_{\mathrm{sc}}\, j_{\mathrm{s}}^{x}(z)\,. \tag{3.14}$$

Consequently, the ISHE voltage drop can be expressed as:

$$\Delta V_{\mathrm{ISHE}} = \gamma_{\mathrm{sc}}\, \langle j_{\mathrm{s}}^{x}(z)\rangle_z\, \rho\, d\,, \tag{3.15}$$

where ρ is the electrical resistivity, d the distance between the electrodes, and $\langle j_{\mathrm{s}}^{x}(z)\rangle_z$ denotes the spatial average of the spin current density along the out-of-plane direction. Within the model, the spin current satisfies:

$$\frac{1}{D_\mathrm{e}}\frac{\partial j_\mathrm{s}^x(z)}{\partial z} = -\frac{s^x(z)}{L_\mathrm{s}^2} + \frac{\mathrm{DSP}^x\,\alpha\,\Phi\,e^{\alpha z}}{D_\mathrm{e}}, \tag{3.16}$$

where $j_\mathrm{s}^x(z) = -D_\mathrm{e}\,\partial s^x(z)/\partial z$ and $s^x(z)$ is the spin density polarized along x. The Eq. (3.16) is solved under the boundary conditions $j_\mathrm{s}^x(0) = 0$ and $j_\mathrm{s}^x(-t) = 0$, reflecting the absence of spin leakage through the sample surfaces at $z = 0$ and $z = -t$, being t the crystal thickness. The average spin current density, $\langle j_\mathrm{s}^x(z)\rangle_z$, is obtained by averaging $j_\mathrm{s}^x(z)$ over t. In the limit $t \gg L_\mathrm{s}$ and $t \gg \alpha^{-1}$, it can be approximated as:

$$\langle j_\mathrm{s}^x(z)\rangle_z = \Phi\,\frac{\mathrm{DSP}^x\,\alpha\,L_\mathrm{s}^2}{t\,(1+\alpha L_\mathrm{s})}. \tag{3.17}$$

Substituting Eq. (3.17) into Eq. (3.15) and assuming the spin Hall angle γ_sc as a constant, the spectral dependence of the normalized ISHE signal can be interpreted as:

$$\frac{\Delta V_\mathrm{ISHE}}{\Phi} \propto \frac{\mathrm{DSP}^x\,\alpha\,L_\mathrm{s}^2}{1+\alpha\,L_\mathrm{s}}. \tag{3.18}$$

The ISHE spectrum results governed by three parameters: the light absorption coefficient, the electron degree of spin polarization and the spin diffusion length. While the α and DSP^x can be directly evaluated within the fully linear response theory from the electronic band structure, the value of L_s for $CdGeAs_2$ has not yet been established. In the following, we use the ISHE spectrum to gain insight into L_s.

The 8-band $\mathbf{k}\cdot\mathbf{p}$ model provides the photon-energy dependence of the coefficients $\xi^{xx}(\omega)$ and $\xi^{zz}(\omega)$ (Fig. 3.5a) of the carrier-injection tensor, and $\zeta^{xyz}(\omega)$ and $\zeta^{zxy}(\omega)$ (Fig. 3.6a) of the spin-injection pseudotensor. Thus, the effective carrier- and spin-injection rates, ξ and ζ, as functions of the photon energy are computed using Eqs. (3.12) and (3.13) for $\Theta = -27°$. These are reported for σ^- polarization in Figs. 3.11a and 3.11b, together with α and DSP^x in Figs. 3.11c and 3.11d, respectively. At this stage, we use α and DSP^x to infer the spin diffusion length L_s that best reproduces the measured spectral dependence of the ISHE signal. The right-hand side of Eq. (3.18) is evaluated assuming the spin diffusion length constant for $L_\mathrm{s} \simeq 10\ \mu$m, $L_\mathrm{s} \simeq 1\ \mu$m, and $L_\mathrm{s} \simeq 100$ nm. The results are presented in Fig. 3.11e. The curve for $L_\mathrm{s} = 10\ \mu$m is representative of the limit $L_\mathrm{s} \gg \alpha^{-1}$, where Eq. (3.18) reduces to $\Delta V_\mathrm{ISHE} \propto \mathrm{DSP}^x L_\mathrm{s}$. Conversely, $L_\mathrm{s} = 100$ nm illustrates the opposite regime $L_\mathrm{s} \ll \alpha^{-1}$, yielding $\Delta V_\mathrm{ISHE} \propto \mathrm{DSP}^x \alpha L_\mathrm{s}^2$. In this limit, since $\mathrm{DSP}^x = \zeta/\xi$ and $\alpha \propto \xi$, one obtains $\Delta V_\mathrm{ISHE} \propto \zeta\,L_\mathrm{s}^2$.

Comparison between experiment and model indicates that the increase of the detected

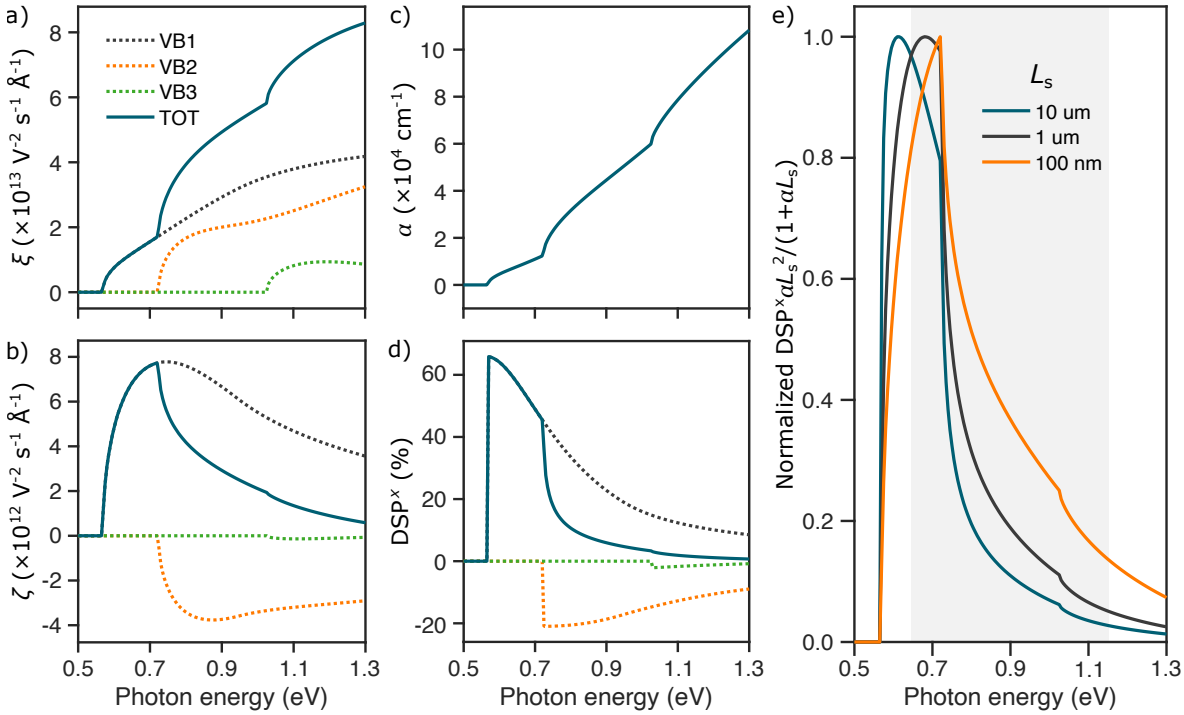

Figure 3.11: (a) Effective carrier injection rate ξ and (b) spin injection rate ζ as functions of the photon energy for σ^- polarization, along with (c) the absorption coefficient α and (d) the degree of spin polarization DSP^x. These quantities are calculated from the 8-band $\mathbf{k}\cdot\mathbf{p}$ model described in Sec. 3.2. Individual contributions from VB1 (gray dashed line), VB2 (orange dashed line) and VB3 (green dashed line) are separated from the total ξ, ζ, α, and DSP^x (blue line). (e) Photon-energy dependence of $\mathrm{DSP}^x \alpha L_\mathrm{s}^2/(1+\alpha L_\mathrm{s})$ evaluated for a spin diffusion length $L_\mathrm{s} = 10$ μm (blue line), 1 μm (gray line), and 100 nm (orange line). Each curve is normalized to the maximum and the gray area is the explored photon-energy range of the ISHE spectrum. The behavior for $L_\mathrm{s} = 100$ nm best reproduces the features of the ISHE spectrum and furnishes an estimation for the spin diffusion length in $CdGeAs_2$.

signal up to 0.72 eV (Fig. 3.10) is reproduced only by $L_\mathrm{s} = 100$ nm. By contrast, the 10 μm curve shows a marked decrease in the $0.6 - 0.7$ eV range, while the 1 μm case remains approximately flat. For $\hbar\omega > 0.72$ eV, all curves drop sharply due to the onset of transitions from VB2, which inject electrons with spin polarization opposite to that from VB1 (Fig. 3.11d). This reduction is weakest for $L_s = 100$ nm, which again provides the closest match to the experiment. At higher photon energies, the diffusion-model curve for $L_\mathrm{s} = 100$ nm predicts a gradual decrease not observed experimentally. This discrepancy is attributed to the assumption of constant L_s and γ_sc even when electrons are generated well above the CB minimum. In semiconductors, γ_sc can increase significantly for hot carriers,

commonly enhancing the ISHE signal at increasing photon energy [68], [88], [109]. The dependence of the spin Hall angle with the photon energy is of the type:

$$\gamma_{\mathrm{sc}}(\hbar\omega) \propto e^{\mathcal{C}\hbar\omega}, \tag{3.19}$$

where $\mathcal{C}$ is the exponential rate, which is ≈ 5 in Ge [68]. A similar growth is observed also in GaAs [88], where it is ascribed to the inter-valley scattering of spin-polarized electrons from Γ into the L point. Therefore, we fit here the $\Delta V_{\mathrm{ISHE}}/\Phi$ spectrum with Eq. (3.18), including the spin Hall angle given by Eq. (3.19). The exponential rate is used as free parameter. The spectral $\Delta V_{\mathrm{ISHE}}/\Phi$ dependence is then interpreted as:

$$\frac{\Delta V_{\mathrm{ISHE}}}{\Phi} \propto \frac{\mathrm{DSP}^x\,\alpha\,L_{\mathrm{s}}^2}{1+\alpha\,L_{\mathrm{s}}}\,e^{\mathcal{C}\hbar\omega}. \tag{3.20}$$

The fitting analysis leads to $\mathcal{C} \simeq 3.4$. Such a model (Fig. 3.10) accounts for the nearly flat ISHE response above 0.8 eV. The small peak at $\simeq 1.025$ eV, which coincides with the absorption onset from VB3, corresponds to a kink in the fit, partially explaining the feature. We further mention that, at this threshold, electrons excited from VB3 are injected close to the CB minimum. Consequently, they are less affected by momentum scattering and spin relaxation, which also may yield a distinguishable contribution around $\simeq 1.025$ eV.

The spectral behavior is thus consistent with $L_{\mathrm{s}} \lesssim 100$ nm in $CdGeAs_2$, comparable to GaAs [110], [111] but much smaller than in Si and Ge, where $L_{\mathrm{s}} \sim 1$ μm [38], [49], [110], [112], [113]. In $CdGeAs_2$, $L_{\mathrm{s}} \ll \alpha^{-1}$ and the ISHE voltage scales as $\Delta V_{\mathrm{ISHE}} \propto \gamma_{\mathrm{sc}}\zeta\,L_{\mathrm{s}}^2$, so a short spin diffusion length suppresses the ISHE amplitude. Despite this suppression, the measured signal is greater than that reported for Ge [68], suggesting a significantly larger γ_{sc} for thermalized electrons in $CdGeAs_2$ (for comparison, $\gamma_{\mathrm{sc}} \sim 10^{-4}$ and $\Delta V_{\mathrm{ISHE}}/\Phi \sim 10^{-15}$ nV μm^2 s in Ge [68]). A quantitative estimate of γ_{sc} in $CdGeAs_2$ would require a more precise determination of L_{s}, which is beyond the scope of the present analysis. Finally, it is worth noting that a short spin diffusion length is a key ingredient to enable fast modulation of spin-dependent signals using high-frequency electric fields, as explained in the next sections.

3.4. Spin relaxation in Ge, Si, and GaAs

Before studying how fast a spin signal can be electrically modulated in the drift-diffusion regime, we focus here on momentum and spin lifetime of polarized electrons with kinetic

energy $E_\mathrm{k} = k_\mathrm{B}T$ above the CB minimum in n-doped Ge, Si, and GaAs at 300 K. These electrons occupy the minima at the L and Γ points for Ge and GaAs, respectively, and the Δ valleys of the BZ for Si. The spin lifetime will then be used as input in the simulations of Sec. 3.5. The starting point is the calculation of the momentum lifetime τ_m. Momentum scattering occurs because of perturbations in the lattice potential, which are related to collisions with phonons (accounted by the total phonon-scattering time $\tau_\mathrm{m}^{\mathrm{ph,tot}}$) or impurities (similarly expressed by $\tau_\mathrm{m}^{\mathrm{imp}}$). Since both mechanisms contribute to the total momentum lifetime, the latter is given by:

$$(\tau_\mathrm{m}^{\mathrm{tot}})^{-1} = (\tau_\mathrm{m}^{\mathrm{ph,tot}})^{-1} + (\tau_\mathrm{m}^{\mathrm{imp}})^{-1}. \tag{3.21}$$

In the following, the evaluation of both contributions and the total momentum lifetime in Ge, Si, and GaAs are discussed.

Phonons are distinguished based on their energy $\hbar\omega^{\mathrm{ph}}$ in acoustic (accounted by $\tau_\mathrm{m}^{\mathrm{ph,a}}$ and $\hbar\omega_\mathrm{a}^{\mathrm{ph}}$) and optical (expressed by $\tau_\mathrm{m}^{\mathrm{ph,o}}$ and $\hbar\omega_\mathrm{o}^{\mathrm{ph}}$). The energy $\hbar\omega_\mathrm{a}^{\mathrm{ph}}$ is a few meV, whereas $\hbar\omega_\mathrm{o}^{\mathrm{ph}}$ is a few tens of meV in Ge, Si, and GaAs [114], [115]. Optical phonon scattering can also induce carrier transfer from a valley to another, which leads us to distinguish from intra- and inter-valley processes. For thermalized electrons, inter-valley processes that cause transfer between different-type valleys are not possible due to the low energies of the involved electrons and phonons. Nevertheless, in Ge and Si inter-valley scattering between different L (inter-LL) and Δ (inter-ΔΔ) valleys, respectively, is allowed and results in significant contributions to the phonon-scattering time, namely $\tau_\mathrm{m}^{\mathrm{ph,LL}}$ and $\tau_\mathrm{m}^{\mathrm{ph},\Delta\Delta}$. For both intra- and inter-valley mechanisms, we have to account for both the emission (emi) and absorption (abs) of phonons to evaluate the rate of phonon scattering:

$$(\tau_\mathrm{m}^{\mathrm{ph}})^{-1} = (\tau_\mathrm{m}^{\mathrm{ph,abs}})^{-1} + (\tau_\mathrm{m}^{\mathrm{ph,emi}})^{-1}. \tag{3.22}$$

Phonons are emitted only when electrons have sufficient energy, therefore $\tau_\mathrm{m}^{\mathrm{ph,emi}}$ furnishes a contribution only for $E_\mathrm{k} > \hbar\omega^{\mathrm{ph}}$. For acoustic phonon scattering, $\hbar\omega_\mathrm{a}^{\mathrm{ph}}$ can be neglected and Eq. (3.22) becomes [116]:

$$(\tau_\mathrm{m}^{\mathrm{ph,a}})^{-1} = \frac{\pi D_\mathrm{a}^2 k_\mathrm{B} T}{\hbar\rho v_\mathrm{s}^2} g(E_\mathrm{k}), \tag{3.23}$$

being D_a the deformation potential, T the temperature, ρ the volumetric mass density, v_s the sound velocity, and $g(E_\mathrm{k})$ the density of states. The latter is given by:

$$g(E_{\mathrm{k}}) = \frac{1}{2\pi^2}\left(\frac{2m^*}{\hbar^2}\right)^{3/2}\sqrt{E_{\mathrm{k}}}, \tag{3.24}$$

with m^* the effective mass of electrons in the CB minima. For optical phonon scattering, Eq. (3.22) is used to evaluate $\tau_{\mathrm{m}}^{\mathrm{ph,o}}$ with the emission and absorption rates calculated as [116]:

$$[\tau_{\mathrm{m}}^{\mathrm{ph,abs(emi)}}]^{-1} = \frac{\pi D_{\mathrm{o}}^2}{2\rho\omega_{\mathrm{o}}^{\mathrm{ph}}} g[E_{\mathrm{k}} \overset{+}{(-)} \hbar\omega_{\mathrm{o}}^{\mathrm{ph}}] \cdot \left[n_{\mathrm{ph}} + \frac{1}{2} \overset{-}{(+)} \frac{1}{2}\right], \tag{3.25}$$

where n_{ph} is the number of phonons. This can be calculated from Bose-Einstein statistics:

$$n_{\mathrm{ph}} = \left(e^{\hbar\omega_{\mathrm{o}}^{\mathrm{ph}}/k_{\mathrm{B}}T} - 1\right)^{-1}. \tag{3.26}$$

For inter-valley scattering, Eqs. (3.25) and (3.26) become:

$$[\tau_{\mathrm{m}}^{\mathrm{ph,abs(emi)}}]^{-1} = \frac{M_{\mathrm{x}}\pi D_{\mathrm{xx}}^2}{2\rho\omega_{\mathrm{xx}}^{\mathrm{ph}}} g[E_{\mathrm{k}} \overset{+}{(-)} \hbar\omega_{\mathrm{xx}}^{\mathrm{ph}}] \cdot \left[n_{\mathrm{ph}} + \frac{1}{2} \overset{-}{(+)} \frac{1}{2}\right], \tag{3.27a}$$

$$n_{\mathrm{ph}} = \left(e^{\hbar\omega_{\mathrm{xx}}^{\mathrm{ph}}/k_{\mathrm{B}}T} - 1\right)^{-1}, \tag{3.27b}$$

being $x = \mathrm{L}$ for Ge, $x = \Delta$ for Si, and M_{x} the degeneracy of the x valley. The times $\tau_{\mathrm{m}}^{\mathrm{ph,LL}}$ and $\tau_{\mathrm{m}}^{\mathrm{ph},\Delta\Delta}$ are then calculated using Eq. (3.22). Once intra-valley times $\tau_{\mathrm{m}}^{\mathrm{ph,a}}$ and $\tau_{\mathrm{m}}^{\mathrm{ph,o}}$, and inter-valley times $\tau_{\mathrm{m}}^{\mathrm{ph,LL}}$ and $\tau_{\mathrm{m}}^{\mathrm{ph},\Delta\Delta}$ are known, the total phonon-scattering time is evaluated as:

$$(\tau_{\mathrm{m}}^{\mathrm{ph,tot}})^{-1} = (\tau_{\mathrm{m}}^{\mathrm{ph,a}})^{-1} + (\tau_{\mathrm{m}}^{\mathrm{ph,o}})^{-1} + (\tau_{\mathrm{m}}^{\mathrm{ph,xx}})^{-1}. \tag{3.28}$$

The parameters used in calculations are taken from the Monte Carlo simulation of Fischetti [114] and are reported in Tables 3.1 and 3.2 for intra- and inter-valley scattering, respectively. Figs. 3.12a - 3.12c present optical ($\tau_{\mathrm{m}}^{\mathrm{ph,o}}$), acoustic ($\tau_{\mathrm{m}}^{\mathrm{ph,a}}$), inter-LL ($\tau_{\mathrm{m}}^{\mathrm{ph,LL}}$), and inter-$\Delta\Delta$ ($\tau_{\mathrm{m}}^{\mathrm{ph},\Delta\Delta}$) phonon-scattering times as functions of the kinetic energy E_{k}. In Ge and Si, inter-LL and inter-$\Delta\Delta$ valleys scattering are faster than intra-valley scattering and are the dominating contributions. In GaAs, scattering with acoustic phonons whereas has the lowest momentum lifetime. The $\tau_{\mathrm{m}}^{\mathrm{ph}}$ values for $E_{\mathrm{k}} = k_{\mathrm{B}}T$ are then used to evaluate $\tau_{\mathrm{m}}^{\mathrm{ph,tot}}$, that is compared with the impurity contribution and employed to calculate $\tau_{\mathrm{m}}^{\mathrm{tot}}$ with Eq. (3.21).

Table 3.1: Parameters employed in the calculation of τ_{m} in Ge, Si, and GaAs for intra-valley scattering, reported from Ref. [114]. m_0 is the free electron mass.

Material	D_{a} [eV]	ρ [kg/m^3]	v_{s} [m/s]	D_{o} [10^{10} eV m^{-1}]	$\hbar\omega_{\mathrm{o}}^{\mathrm{ph}}$ [meV]	m^* [m_0]
Ge	2.5	5323	4910	3.5	37	0.22†
Si	1.7	2330	5910	2.1	62	0.30‡
GaAs	5.0	5360	4700	2.1	35	0.07§

† taken from Ref. [117]; ‡ Ref. [118]; § Ref. [115].

Table 3.2: Parameters employed in the calculation of τ_{m} in Ge and Si for inter-valley scattering, reported from Ref. [114].

Material	D_{xx} [10^{10} eV m^{-1}]	$\hbar\omega_{\mathrm{xx}}^{\mathrm{ph}}$ [meV]	M_{x} [ad]
Ge ($x = \mathrm{L}$)	5.26	24	4
Si ($x = \Delta$)	2.26	51	6

The rate of impurity scattering is evaluated using the Brooks-Herring approach [116]:

$$(\tau_{\mathrm{m}}^{\mathrm{imp}})^{-1} = \frac{N_{\mathrm{d}} q^4}{16\pi\epsilon^2\sqrt{2m^*}} \left[\ln\left(1+\beta^2\right) - \frac{\beta^2}{1+\beta^2}\right] E_{\mathrm{k}}^{-3/2,} \tag{3.29}$$

being N_{d} the doping density, ϵ the permittivity, and:

$$\beta^2 = \frac{8m^* l_{\mathrm{TF}}^2}{\hbar^2} E_{\mathrm{k}}, \tag{3.30}$$

with l_{TF} the Thomas-Fermi screening length. This in SI units is (details in Appendix B):

$$l_{\mathrm{TF}} = \left(\frac{q^2 m^* (3\pi^2 N_{\mathrm{d}})^{1/3}}{\epsilon\pi^2\hbar^2}\right)^{-1/2} \tag{3.31}$$

The permittivities employed to calculate $\tau_{\mathrm{m}}^{\mathrm{imp}}$ are 16.2 for Ge, 11.7 for Si, and 12.9 for GaAs, expressed in units of the vacuum permittivity ϵ_0 [114]. Figs. 3.13a - 3.13c present the total phonon-scattering time $\tau_{\mathrm{m}}^{\mathrm{ph,tot}}$, the impurity-scattering time $\tau_{\mathrm{m}}^{\mathrm{imp}}$, and the total momentum lifetime $\tau_{\mathrm{m}}^{\mathrm{tot}}$ as functions of the semiconductors doping level N_{d} at room temperature. In Ge, phonon scattering, dominated by inter-LL valleys scattering, is the leading contribution to the total momentum lifetime for $N_{\mathrm{d}} < 3 \times 10^{16}\,\mathrm{cm}^{-3}$, providing a nearly flat dependence of $\tau_{\mathrm{m}}^{\mathrm{tot}}$ with N_{d}. For larger doping concentrations, $\tau_{\mathrm{m}}^{\mathrm{tot}}$ begins to

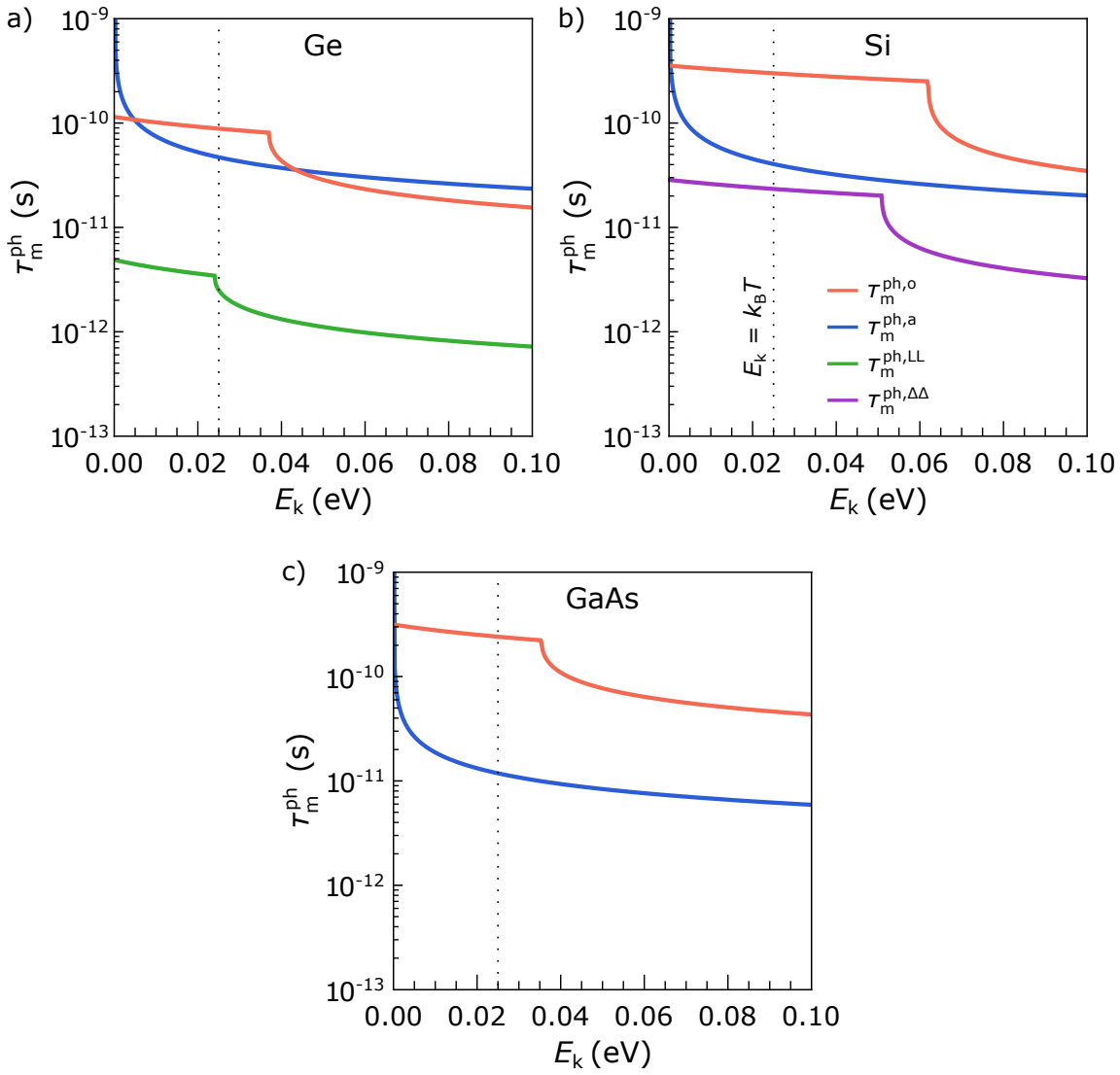

Figure 3.12: Optical $\tau_m^{ph,o}$ (red), acoustic $\tau_m^{ph,a}$ (blue), and inter-valley $\tau_m^{ph,xx}$ (green and violet) phonon-scattering times as functions of the electron kinetic energy E_k for (a) Ge ($x = L$), (b) Si ($x = \Delta$), and (c) GaAs at 300 K. The vertical dotted lines indicate the thermal energy $k_B T$.

decrease due to impurity scattering. In Si and GaAs, phonon scattering results negligible with respect to impurity scattering except around $N_d \approx 10^{15}\,cm^{-3}$, where the momentum lifetimes of the two processes are equal. Accordingly, τ_m^{tot} decreases by increasing N_d in the explored doping-density range, with values spanning from 10 fs to 10 ps.

Spin relaxation mechanisms presented in Sec. 1.2.6 connect the momentum and spin lifetimes. In Ge and Si, spin relaxation is only driven by the Elliott-Yafet (EY) mechanism being centrosymmetric semiconductors. Conversely, GaAs lacks inversion symmetry and spin depolarization is driven by the combined EY and Dyakonov-Perel (DP) mechanisms.

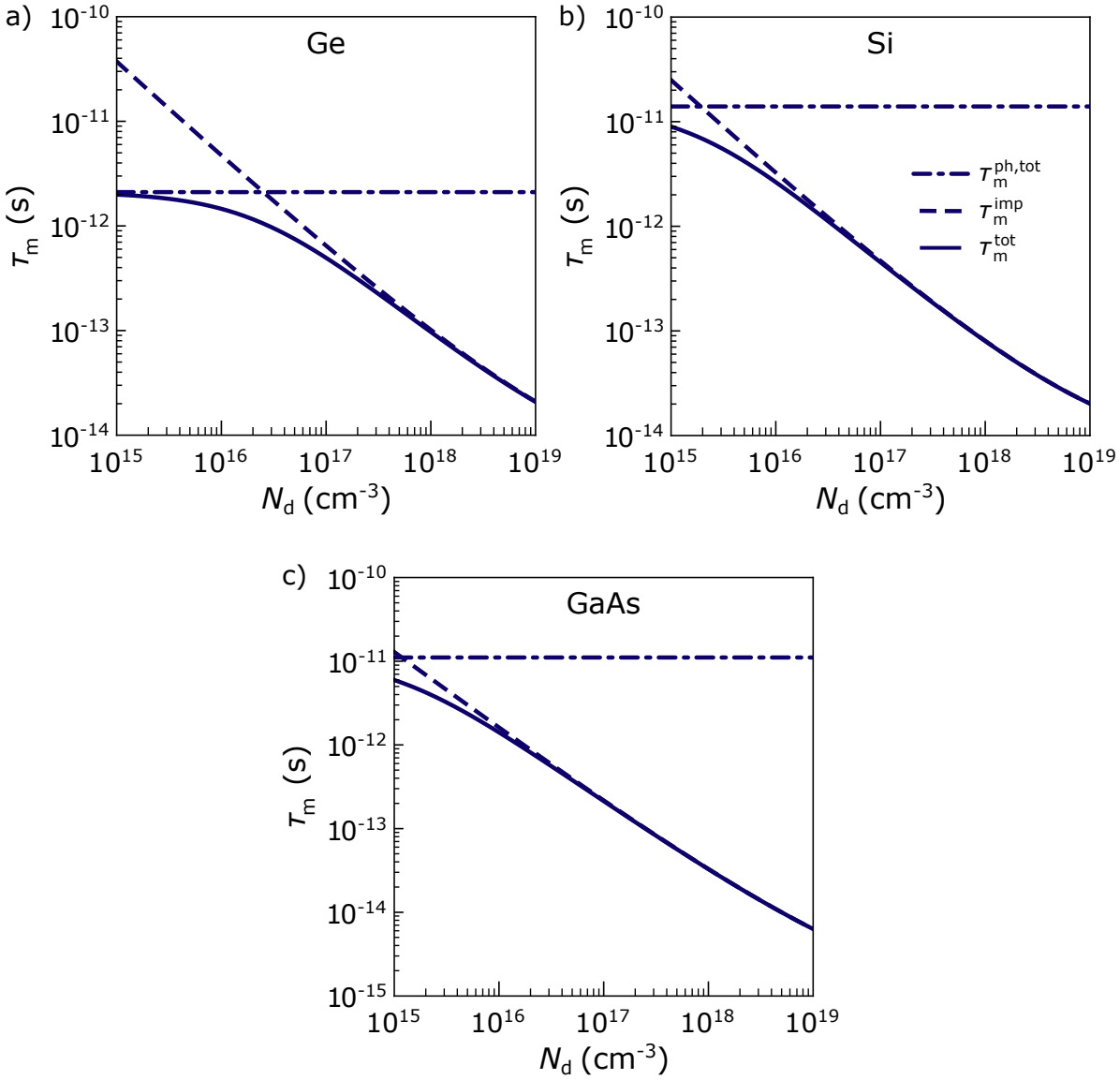

Figure 3.13: Total phonon-scattering time $\tau_{\mathrm{m}}^{\mathrm{ph,tot}}$ (dashed and dotted), impurity-scattering time $\tau_{\mathrm{m}}^{\mathrm{imp}}$ (dashed), and total momentum lifetime $\tau_{\mathrm{m}}^{\mathrm{tot}}$ (solid) as functions of the doping density N_{d} for n-doped (a) Ge, (b) Si, and (c) GaAs at 300 K.

The spin lifetimes associated with the EY mechanism are calculated separately for phonon scattering ($\tau_{\mathrm{s}}^{\mathrm{EY,ph}}$) and impurity scattering ($\tau_{\mathrm{s}}^{\mathrm{EY,imp}}$), using Eq. 1.67. The spin lifetime associated with the DP mechanism in GaAs is estimated using Eq. 1.69, with the parameters $Q = 1.5$ and $\alpha_c = 0.07$ [98]. The total spin lifetime is then evaluated as:

$$(\tau_{\mathrm{s}}^{\mathrm{tot}})^{-1} = (\tau_{\mathrm{s}}^{\mathrm{EY,ph}})^{-1} + (\tau_{\mathrm{s}}^{\mathrm{EY,imp}})^{-1} + (\tau_{\mathrm{s}}^{\mathrm{DP}})^{-1}. \tag{3.32}$$

Figs. 3.14a - 3.14c present the spin lifetimes for Ge, Si, and GaAs, respectively. Because

of EY relaxation, τ_s^{tot} decreases with N_d, following the same dependence of τ_m^{tot} in the first two semiconductors. In contrast, DP relaxation is more efficient than EY relaxation in GaAs, except for $N_d \simeq 10^{19}\,cm^{-3}$, resulting in an increase of τ_s^{tot} with N_d. The resulting spin lifetimes τ_s in Ge and GaAs agree with previous reports (Table 3.3), whereas in Si the spin lifetime is larger than in Refs. [49], [73], [112], [118]–[122]. This discrepancy likely arises from the application of Eq. (1.67), which is fully valid only near the Γ point, to evaluate the EY spin lifetime of electrons in the Δ valleys [73], [122]. Moreover, treating impurity scattering solely as an intra-valley process could also lead to discrepancies in the estimated spin lifetime in Si [118].

3.5. Frequency response of spin drift-diffusion

The spatial and temporal evolution of the spin density s, defined as in Eq. (1.7), is analyzed under the influence of a time-dependent electric field $E(t) = E_0 \sin(2\pi f t)$. The field is considered uniform and directed parallel to the electron velocity within a one-dimensional (1D) domain which simulates the channel of a non-local (NL) device. The geometry of the simulation is shown in Fig. 3.15. The system is investigated using the finite element method implemented in *COMSOL Multiphysics® 6.0* to numerically solve the time-dependent, coupled spin drift-diffusion and continuity equations. In a 1D geometry with uniform electric field along the x axis, these equations take the following form:

$$j_s(x,t) = q\left[\mu_e s(x,t)E(t) + D_e\frac{\partial s(x,t)}{\partial x}\right], \tag{3.33a}$$

$$\frac{\partial s(x,t)}{\partial t} = \frac{1}{q}\frac{\partial j_s(x,t)}{\partial x} - \frac{s(x,t)}{\tau_s}. \tag{3.33b}$$

They are solved for n-doped Ge, Si, and GaAs. Figs. 3.16a - 3.16f present the doping dependence of the electron diffusion coefficient D_e, extracted from Refs. [127]–[129], of the spin lifetime τ_s, evaluated as described in Sec. 3.4, and of the spin diffusion length $L_s = \sqrt{D_e\tau_s}$. Because L_s varies substantially with semiconductor type and doping density (see Figs. 3.16d - 3.16f), the simulation domain and mesh are scaled accordingly. A domain length of $10L_s$ is chosen to ensure that the net spin population becomes negligible at the end of the channel, even under the applied electric field, and a mesh size of $L_s/30$ is used for numerical stability. For $t > 0$, the boundary conditions are defined as $j_s(0,t) = j_{s,0}$ and $s(10L_s,t) = 0$, corresponding to a constant spin current at the injection point and vanishing spin density at the channel extremity. The initial condition is defined as:

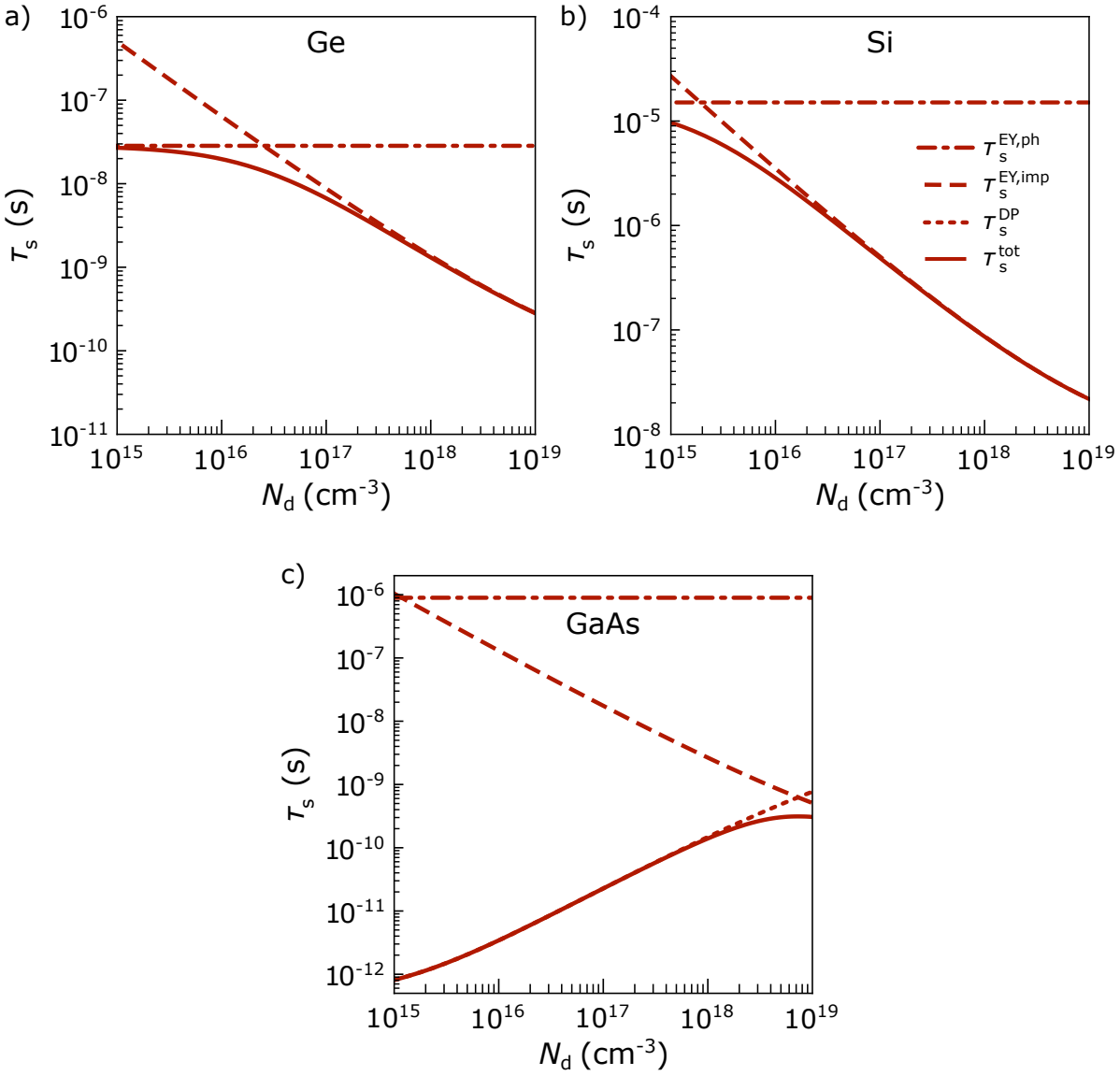

Figure 3.14: Elliott-Yafet (EY) spin lifetime induced by phonon scattering $\tau_s^{EY,ph}$ (dashed and dotted) and by impurity scattering $\tau_s^{EY,imp}$ (dashed), together with the Dyakonov-Perel (DP) spin lifetime τ_s^{DP} (dotted) and the total spin lifetime τ_s^{tot} (solid) as functions of the doping density N_d for n-doped (a) Ge, (b) Si, and (c) GaAs at 300 K.

$$s(x,0) = s_0(x) = s_0(0)e^{-x/L_s}, \tag{3.34}$$

which represents the steady-state analytical solution of Eqs. (3.33) in the purely diffusive regime, i.e., for $E(t) = 0$. With μ_e, D_e, τ_s, and L_s as input parameters, Eqs. (3.33) are numerically solved for different electric-field amplitudes E_0 and frequencies f at room temperature. The computed output quantity is the spin density $s(x,t)$, normalized to its

Table 3.3: Experimental and calculated spin lifetime τ_s of thermalized electrons at 300 K in Ge, Si, and GaAs. References: (1) Zucchetti, Bollani, Isella, *et al.* [123]; (2) Yamada, Tsukahara, Fujita, *et al.* [40]; (3) Rortais, Vergnaud, Marty, *et al.* [124]; (4) Li, Song, and Dery [117]; (5) Bottegoni, Zucchetti, Ciccacci, *et al.* [112]; (6) Zucchetti, Scali, Grassi, *et al.* [49]; (7) Dash, Sharma, Patel, *et al.* [120]; (8) Jeon, Min, Shin, *et al.* [121]; (9) Suzuki, Sasaki, Oikawa, *et al.* [119]; (10) Cheng, Wu, and Fabian [73]; (11) Li and Dery [122]; (12) Oertel, Huebner, and Oestreich [125]; (13) Jiang and Wu [126].

Material	τ_s [ns]	N_d [cm^{-3}]	Exp. Technique	Calc. Method	Ref. (see caption)
Ge	60±10	2.0×10^{15}	OO	-	1
Ge	26±10	8.2×10^{16}	OO	-	1
Ge	17±11	1.2×10^{18}	OO	-	1
Ge	0.4	1.0×10^{19}	LSV	-	2
Ge	0.5	2.0×10^{19}	LSV	-	3
Ge	1	undoped	-	$\mathbf{k} \cdot \mathbf{p}$	4
Si	15±5	9.0×10^{14}	OO	-	5
Si	40±5	1.0×10^{15}	OO	-	6
Si	0.14	1.8×10^{19}	LSV	-	7
Si	0.16	2.5×10^{19}	LSV	-	8
Si	1.3±0.3	5.0×10^{19}	LSV	-	9
Si	10	undoped	-	EPM	10
Si	10	undoped	-	EPM	11
GaAs	0.04	undoped	PL	-	12
GaAs	0.02	1.0×10^{17}	-	KSBE	13

OO = optical orientation; LSV = lateral spin valve; EPM = empirical pseudopotential model; PL = photoluminescence; KSBE = kinetic spin Bloch equation.

diffusive reference value $s_0(x)$.

3.5.1. Temporal dependence of the spin density

Figs. 3.17a - 3.17c present the temporal evolution of the normalized spin density s/s_0 for n-doped Ge ($N_d = 5 \times 10^{18}$ cm^{-3}) over a single period of the electric field (Fig. 3.17a), considering field amplitudes of $E_0 = 10^3$ V/cm and $E_0 = 10^4$ V/cm. The spin density is sampled at injector-detector distances of $x = L_s/2$, $x = L_s$, and $x = 2L_s$, and for a frequency $f = 10^7$ Hz, below the cut-off frequency discussed later.

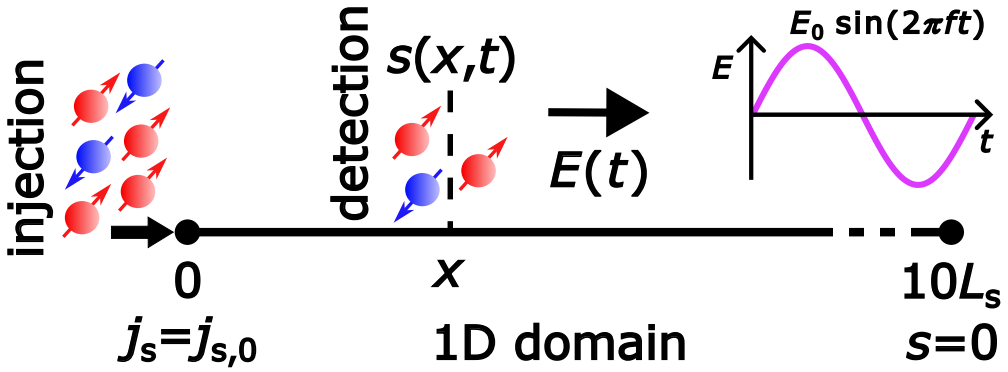

Figure 3.15: The geometry of the simulation. A constant spin current injection happens for $x = 0$ by fixing $j_s(0,t) = j_{s,0}$. The spin density $s(x,t)$ is detected in a $10L_s$-long domain. The boundary condition at the channel end is fixed to $s(10L_s,t) = 0$, imposing a vanishing spin density far away from the injection point. The electric field $E(t)$ varies sinusoidally in time, as shown in the inset.

By varying E_0, two distinct spin drift-diffusion regimes emerge. The first, corresponding to $E_0 = 10^3$ V/cm (Fig. 3.17b), represents a *weak-field regime*, in which s primarily oscillates at the field frequency f and can exceed the diffusive equilibrium value s_0 when $x \neq L_s$. In this regime, $s > s_0$ when the electric field accelerates spin-polarized electrons for $x = 2L_s$, or when it decelerates them for $x = L_s/2$. In the first case, the electric field pushes electrons further away from the injection point, while in the second it confines them closer to the injector. Consequently, the spin density oscillates mainly at f, with $s(x = L_s/2,t)$ and $s(x = 2L_s,t)$ in antiphase. Notably, for $x = L_s$, the maximum spin density occurs at integer multiples of $T/2$, where $E(t) = 0$ and $s(L_s, nT/2) = s_0(L_s)$, being $T = 1/f$ the field period and n an integer number. Therefore, both positive and negative fields reduce the spin density that reaches a detector located at L_s, yielding oscillations at twice the field frequency.

The second regime, observed for $E_0 = 10^4$ V/cm (Fig. 3.17c), corresponds to a *strong-field regime*, in which s exhibits peaks at a repetition rate of $2f$ and remains mostly below s_0. In this scenario, both positive and negative $E(t)$ values reduce s compared to s_0. This occurs as the field is strong enough to confine electrons either very close to or very far from the injection position. Accordingly, s/s_0 oscillates mainly at twice the field frequency, with peaks appearing at integer multiples of $T/2$ for $x = L_s$, or slightly shifted for $x \neq L_s$ (see the red trace in Fig. 3.17c). The shift occurs because s can transiently exceed s_0 when $t \approx nT/2$.

The distinct behavior at L_s and the existence of two regimes originate from the electric field altering the average propagation distance of spin-polarized electrons before depolarization,

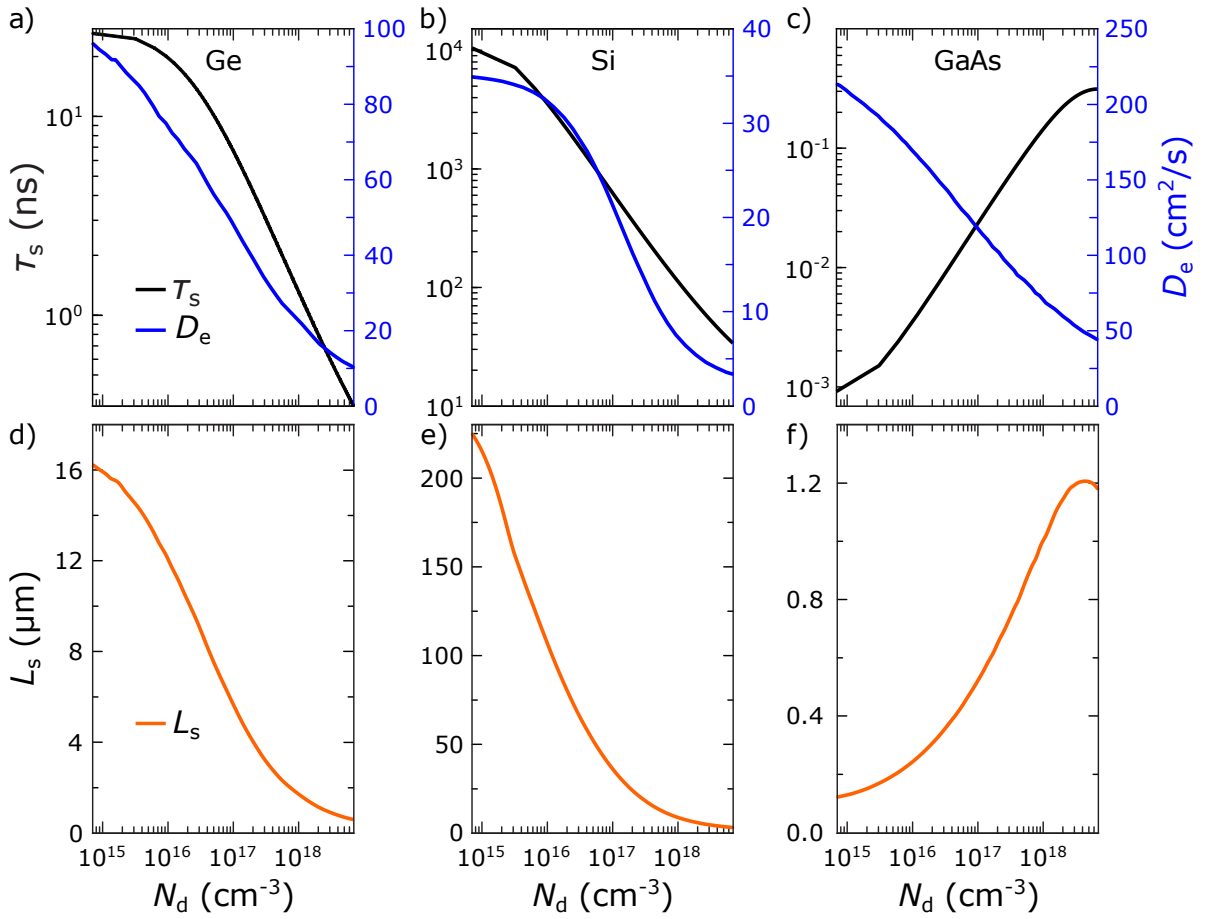

Figure 3.16: (a-c) Electron spin lifetime τ_s (black), diffusion coefficient D_e (blue), and (d-f) spin diffusion length L_s (orange) as functions of the doping density N_d for n-doped Ge, Si, and GaAs at 300 K.

without changing the total spin density in the domain. To gain further insight into the temporal dependence of s/s_0, we consider a semi-infinite region with a fixed spin-current source at the left boundary ($x = 0$) and a temporally constant electric field $E(t > 0) = E_0$ uniformly applied across the domain. The analytical solution of Eqs. (3.33) for the spin density is given by [47]–[49]:

$$s(x) = \bar{A}\, e^{-x/\bar{L}_s}, \tag{3.35}$$

where $\bar{A}$ and $\bar{L}_s$ denote the spin-density amplitude and the spin-transport length, respectively. Both quantities depend on the applied electric field and, in its absence, they reduce to their purely diffusive counterparts: $\bar{A} = s_0(0)$ and $\bar{L}_s = L_s$, as in Eq. (3.34). Accordingly, the spin density for $x = L_s$ at any time $t > 0$ is:

$$s(L_s, t) = \bar{A}\, e^{-L_s/\bar{L}_s}, \tag{3.36}$$

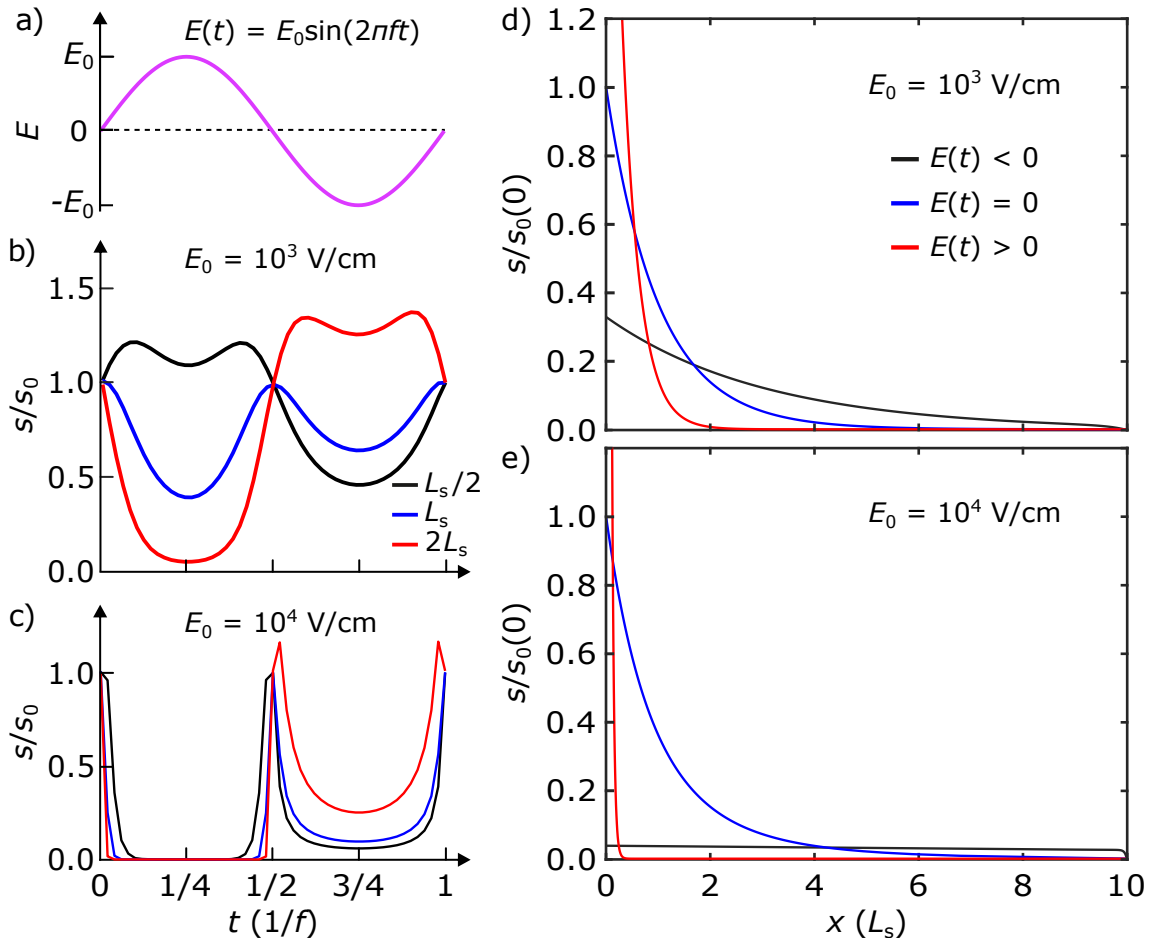

Figure 3.17: Temporal dependence of (a) the electric field $E(t)$ and (b-c) the normalized spin density s/s_0 evaluated for an injector-detector distance $x = L_s/2$ (black), L_s (blue) and $2L_s$ (red). The amplitude of the field is (b) $E_0 = 10^3$ V/cm and (c) 10^4 V/cm, representative cases of the weak- and strong-field regimes, respectively. Spatial dependence of $s/s_0(0)$ evaluated for $E(t) < 0$ (black), $E(t) = 0$ (blue) and $E(t) > 0$ (red) with field's amplitude (d) $E_0 = 10^3$ V/cm and (e) 10^4 V/cm. Calculations are performed with a field frequency $f = 10^7$ Hz in n-doped Ge ($N_d = 5 \times 10^{18}$ cm^{-3}).

which, when $E(t) = 0$, simplifies to $s(L_s, 0) = s_0(0)/e$. Thus:

$$\frac{s(L_s,t)}{s(L_s,0)} = \frac{\bar{A}}{s_0(0)}\, e^{1-L_s/\bar{L}_s}. \tag{3.37}$$

Since the application of an electric field does not modify the source and sink terms in Eqs. (3.33), the total spin density accumulated in the domain, that is given by:

$$s_{tot} = \int_0^\infty s(x,t)\, dx, \tag{3.38}$$

remains conserved between $t = 0$ and any $t > 0$. Integrating Eq. (3.38) for $t > 0$ yields $s_{\mathrm{tot}} = \bar{A}\bar{L}_{\mathrm{s}}$ which therefore must equal its diffusive counterpart $s_0(0)L_{\mathrm{s}}$ obtained for $t = 0$. This conservation condition, $s_0(0)L_{\mathrm{s}} = \bar{A}\bar{L}_{\mathrm{s}}$, allows Eq. (3.37) to be rewritten as:

$$\frac{s(L_{\mathrm{s}}, t)}{s(L_{\mathrm{s}}, 0)} = \frac{L_{\mathrm{s}}}{\bar{L}_{\mathrm{s}}}\, e^{1-L_{\mathrm{s}}/\bar{L}_{\mathrm{s}}}. \tag{3.39}$$

The right-hand side of Eq. (3.39) has an absolute maximum for $\bar{L}_{\mathrm{s}} = L_{\mathrm{s}}$, which leads to $s(L_{\mathrm{s}}, t) = s(L_{\mathrm{s}}, 0)$. This demonstrates that the application of any electric fields that result in $\bar{L}_{\mathrm{s}} \neq L_{\mathrm{s}}$ reduces the spin density accumulated at L_{s} compared to the purely diffusive scenario, as observed in Figs. 3.17b and 3.17c.

Figs. 3.17d and 3.17e present for n-doped Ge the spatial evolution of the spin density s normalized to $s_0(0)$ sampled at fixed times corresponding to $E(t) < 0$, $E(t) = 0$, and $E(t) > 0$ in the *weak-* and *strong-field regimes*, respectively. At fixed times, $E(t)$ can be approximated as constant and Eq. (3.35) becomes the valid analytical solution. From the spatial dependencies, we recognize that the temporal behavior of s and the presence of two regimes also stem from the conservation of s_{tot}. Specifically, the area under the curves in Fig. 3.17d (s_{tot}) is conserved because the electric field can only shift the region where the spin density is accumulated, therefore s oscillates in phase (antiphase) with the field for $x < L_{\mathrm{s}}$ ($x > L_{\mathrm{s}}$). Under strong positive fields in Fig. 3.17e, s is accumulated very closed to $x = 0$. Whereas, under strong negative fields, s is pushed toward the end of the geometry and becomes distributed across the entire domain. Consequently, the positions outside from L_{s} approach the behavior always observed at L_{s}, where the application of either a positive or a negative electric field reduces s compared to s_0. This accounts for the temporal dependence observed in the *strong-field regime*, with peaks occurring at a repetition rate of $2f$.

3.5.2. Frequency dependence of the spin density

Keeping in mind the distinct temporal dependencies of s/s_0, we now turn to investigate spin transport in the frequency domain. The first s_ω/s_0 and second $s_{2\omega}/s_0$ harmonic components of s/s_0 are evaluated as functions of E_0 and f. Fig. 3.18a presents the E_0 dependencies for n-doped Ge and $x = L_{\mathrm{s}}/2$, L_{s}, and $2L_{\mathrm{s}}$. The behaviors confirm the presence of two spin drift-diffusion regimes for $x \neq L_{\mathrm{s}}$. Indeed, s_ω dominates the response at low E_0 and exhibits a maximum at $E_{0,\mathrm{max}}$. The latter depends on the semiconductor and doping concentration, as shown in Fig. 3.18b. For $E_0 > E_{0,\mathrm{max}}$, $s_{2\omega}$ becomes the dominant component, thus $E_{0,\mathrm{max}}$ delineates the threshold between the *weak-* and *strong-field regimes*. At $x = L_{\mathrm{s}}$, $s_{2\omega}$ remains the leading term even for $E_0 < E_{0,\mathrm{max}}$, consistent with

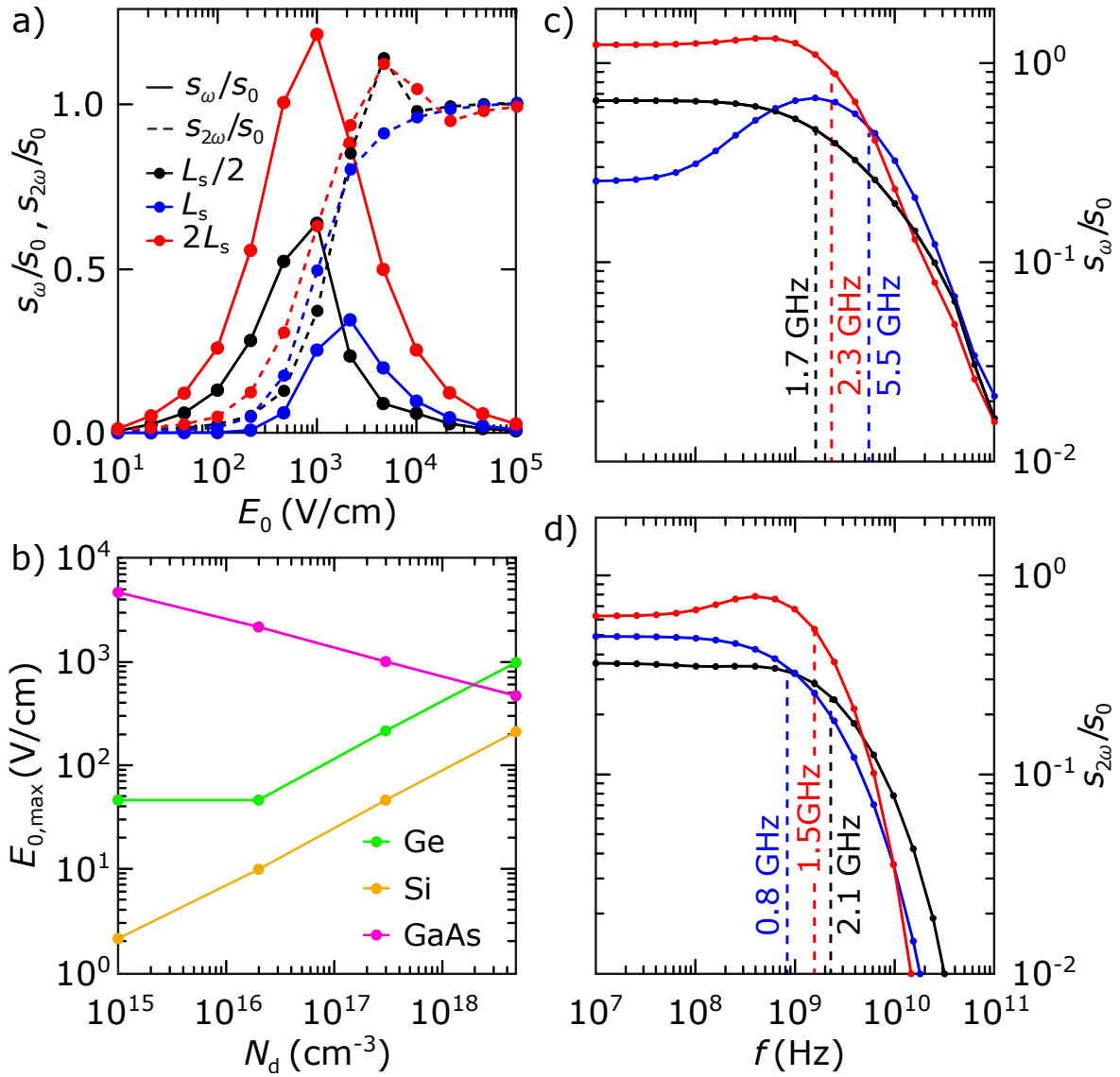

Figure 3.18: (a) The E_0 dependencies of the first s_ω/s_0 (solid lines) and second $s_{2\omega}/s_0$ (dashed lines) harmonics of s/s_0, for $x = L_s/2$ (black), $x = L_s$ (blue), and $x = 2L_s$ (red). (b) The N_d dependence of $E_{0,max}$ in Ge (green), Si (yellow) and GaAs (violet). The f dependencies of (c) s_ω/s_0 and (d) $s_{2\omega}/s_0$ for $E_0 = E_{0,max}$. The dashed vertical lines in panels (c) and (d) report the cut-off frequencies f_ω and $f_{2\omega}$, respectively. Calculations in panels (a), (c), and (d) are performed in n-doped Ge ($N_d = 5 \times 10^{18}$ cm^{-3}).

the time-domain analysis done before. We now address the question regarding how fast such forced oscillations can occur. As a figure of merit of the modulation, we determine the cut-off frequencies f_ω and $f_{2\omega}$ from:

$$|s_\omega(x, f_\omega)| = \frac{\max\left[|s_\omega(x, f)|\right]}{\sqrt{2}}, \qquad |s_{2\omega}(x, f_{2\omega})| = \frac{\max\left[|s_{2\omega}(x, f)|\right]}{\sqrt{2}}. \tag{3.40}$$

Figs. 3.18c and 3.18d illustrate the frequency responses of s_ω/s_0 and $s_{2\omega}/s_0$ for $E_0 = E_{0,\max}$ and the estimated cut-off frequencies f_ω and $f_{2\omega}$, respectively. The non-monotonic behaviors increasing f arise from the suppression of higher harmonics with lower cut-off frequencies compared to f_ω and $f_{2\omega}$, which enhances s_ω/s_0 and $s_{2\omega}/s_0$ near their respective cut-off points. For example, as a consequence of $f_{2\omega} < f_\omega$ for $x = L_\mathrm{s}$ (blue curves), s_ω begins to dominate over $s_{2\omega}$ beyond $f \approx 0.5\,\mathrm{GHz}$, revealing a modulation that is in phase with the electric field. This effect is not captured by the picture based on the conservation of s_tot outlined earlier, which remains valid well below the cut-off frequency and does not provide a straightforward explanation for the behavior observed in its vicinity. In the following, $E_0 = E_{0,\max}$ is used to estimate the cut-off frequency f_ω in the *weak-field regime*, as it maximizes s_ω (Fig. 3.18a). The bias voltage ΔV_0 required for $E_0 = E_{0,\max}$ in a device can be estimated considering two ohmic contacts separated by $5L_\mathrm{s}$. Assuming a uniform field within the semiconductor, ΔV_0 ranges between 200 and 700 mV for Ge, Si, and GaAs, depending on the doping density. Conversely, $E_0 = 10\,E_{0,\max}$ is adopted to evaluate the cut-off frequency $f_{2\omega}$ in the *strong-field regime*, ensuring that $s_{2\omega}$ dominates without requiring bias voltages exceeding a few volts.

Before going into the details of the results for Ge, Si, and GaAs, it is useful to give a general insight about f_ω. Since no analytical expression for f_ω can be derived, the dependence of f_ω at room temperature on τ_s, E_0, and D_e is examined by varying each parameter individually while keeping the others fixed, in order to identify the most favorable operating condition. The resulting dependencies are reported for $x = 2L_\mathrm{s}$ in Figs. 3.19a - 3.19c. f_ω decreases with increasing τ_s, indicating that the modulation governed by spin drift–diffusion becomes more effective when spin-polarized electrons depolarize more rapidly. f_ω increases with E_0 as a result of a stronger driving field that displaces spin-polarized carriers more efficiently within the domain, suggesting that the cut-off frequency can be enhanced by exploiting larger field amplitudes. Finally, f_ω increases with D_e, and therefore with μ_e, showing that high-mobility spin-polarized electrons that possess larger drift velocities enable faster modulation. In summary, operating under strong electric fields with high-mobility electrons exhibiting short spin lifetimes enhances the response speed of spin drift–diffusion.

Figs. 3.20a - 3.20f present s_ω/s_0 and f_ω as functions of the doping density N_d and injector-detector distance x for Ge, Si, and GaAs in the *weak-field regime* ($E_0 = E_{0,\max}$). The ratio s_ω/s_0 is evaluated for $f < f_\omega$ as a figure of merit for the modulated spin amplitude. It decreases with increasing x for $x \lesssim 0.8L_\mathrm{s}$, reaching zero around $x \approx 0.8L_\mathrm{s}$, where the spin density is balanced for positive and negative electric fields. Beyond this point, s_ω/s_0 rises, ultimately following the exponential decay of s_0 with x. Notably, except near

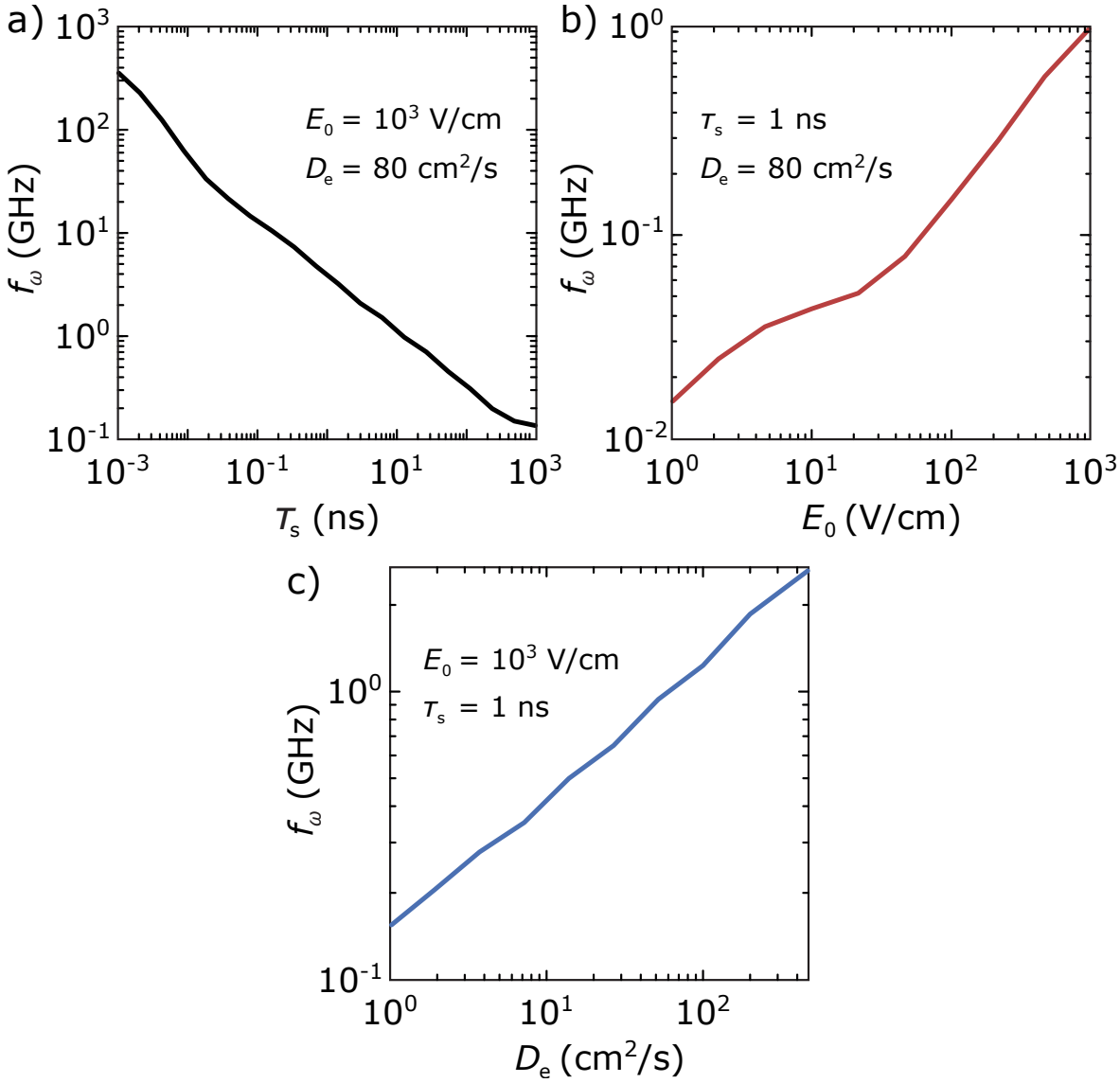

Figure 3.19: The cut-off frequency f_ω as a function of (a) τ_s, (b) E_0 and (c) D_e, evaluated for $x = 2L_s$. The dependencies are calculated by varying each single parameter keeping the others constant and equal to $\tau_s = 1$ ns, $E_0 = 10^3$ V/cm and $D_e = 80$ cm^2/s, respectively.

$x \approx 0.8L_s$, s_ω/s_0 exceeds 10% for nearly all the investigated materials, doping levels, and injector-detector distances. In contrast, f_ω increases approaching positions closer to L_s, pointing to a faster response when the modulated spin amplitude is smaller. Moreover, f_ω increases as L_s decreases. Indeed, the highest f_ω values are achieved in heavily doped Ge and Si (green curves), and in lightly doped GaAs (black curve), reflecting the opposing dependencies of L_s with N_d (see Figs. 3.16d - 3.16f). Specifically, f_ω reaches about 80 MHz in Si, 7 GHz in Ge, and exceeds 2.5 THz in GaAs, owing to the much shorter L_s in the latter semiconductor.

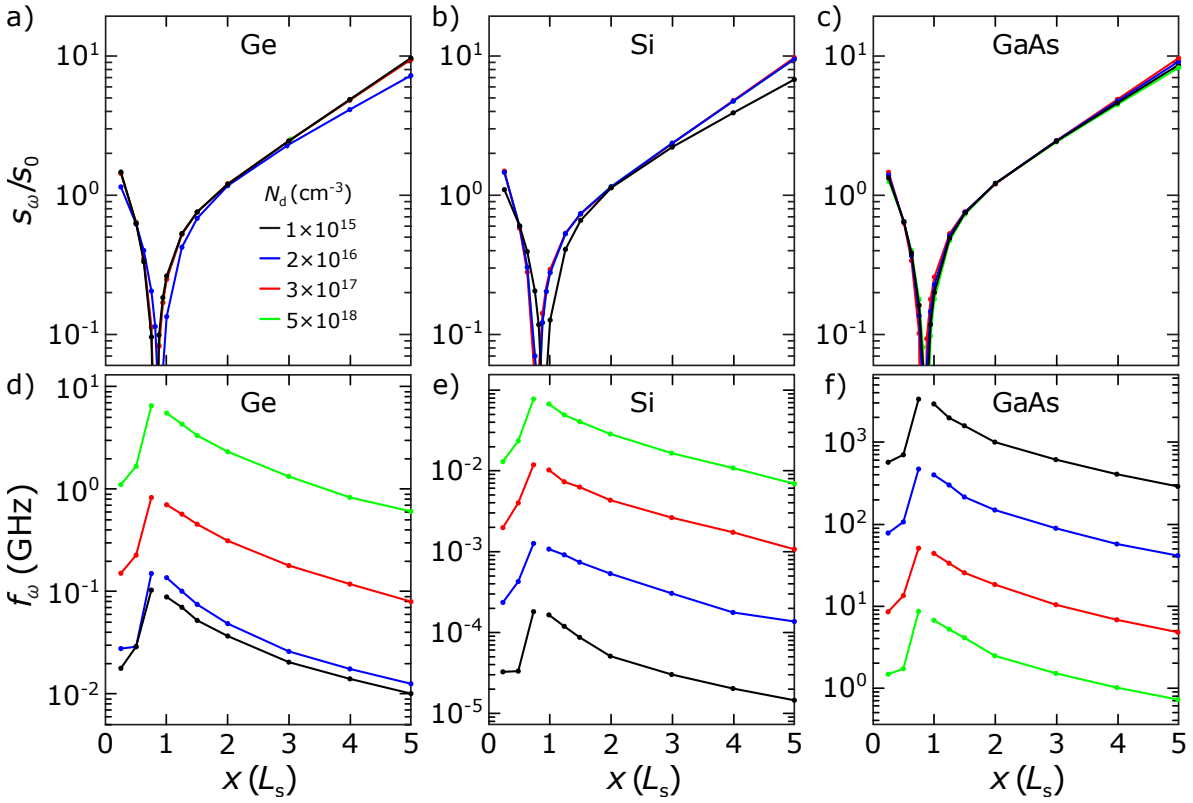

Figure 3.20: (a-c) The s_ω/s_0 and (d-f) f_ω as functions of the injector-detector distance x for Ge, Si, and GaAs. The N_d ranges between 1×10^{15} cm^{-3} (black), 2×10^{16} cm^{-3} (blue), 3×10^{17} cm^{-3} (red) and 5×10^{18} cm^{-3} (green). All the data are evaluated for $E_0 = E_{0,\mathrm{max}}$ and s_ω/s_0 is calculated with a field frequency $f < f_\omega$.

Similarly, Figs. 3.21a - 3.21f present $s_{2\omega}/s_0$ and $f_{2\omega}$ as functions of N_d and x in the *strong-field regime* ($E_0 = 10\,E_{0,\mathrm{max}}$). The ratio $s_{2\omega}/s_0$ remains above 90% across the entire domain, including positions near L_s. The enhancement of $s_{2\omega}/s_0$ for $x \leq L_\mathrm{s}/2$ and $x \geq 2L_\mathrm{s}$ originates from transient increase near $t \approx nT/2$, as already highlighted in the temporal behavior. As for f_ω and s_ω, $f_{2\omega}$ attains maxima where $s_{2\omega}$ is near minima, thus closer to L_s, indicating again a faster response for smaller modulated spin amplitudes. Furthermore, $f_{2\omega}$ consistently exceeds f_ω across all investigated conditions, reflecting the higher modulation speed enabled by stronger electric fields (Fig. 3.19b). In the *strong-field regime*, $f_{2\omega}$ reaches for $x = L_\mathrm{s}/2$ approximately 35 GHz in heavily doped Ge, 480 MHz in heavily doped Si, and 15 THz in lightly doped GaAs. It is worth mentioning that such values are obtained only considering spin transport, neglecting secondary effects that could be determinant in a real device. For example, the detection-junction capacitance and frequency response of spin detectors could further limit the response time. Nevertheless, the spin transport modulation based on drift-diffusion is characterized by a fast response time, allowing for the exploitation of frequencies in the sub-terahertz and terahertz bands

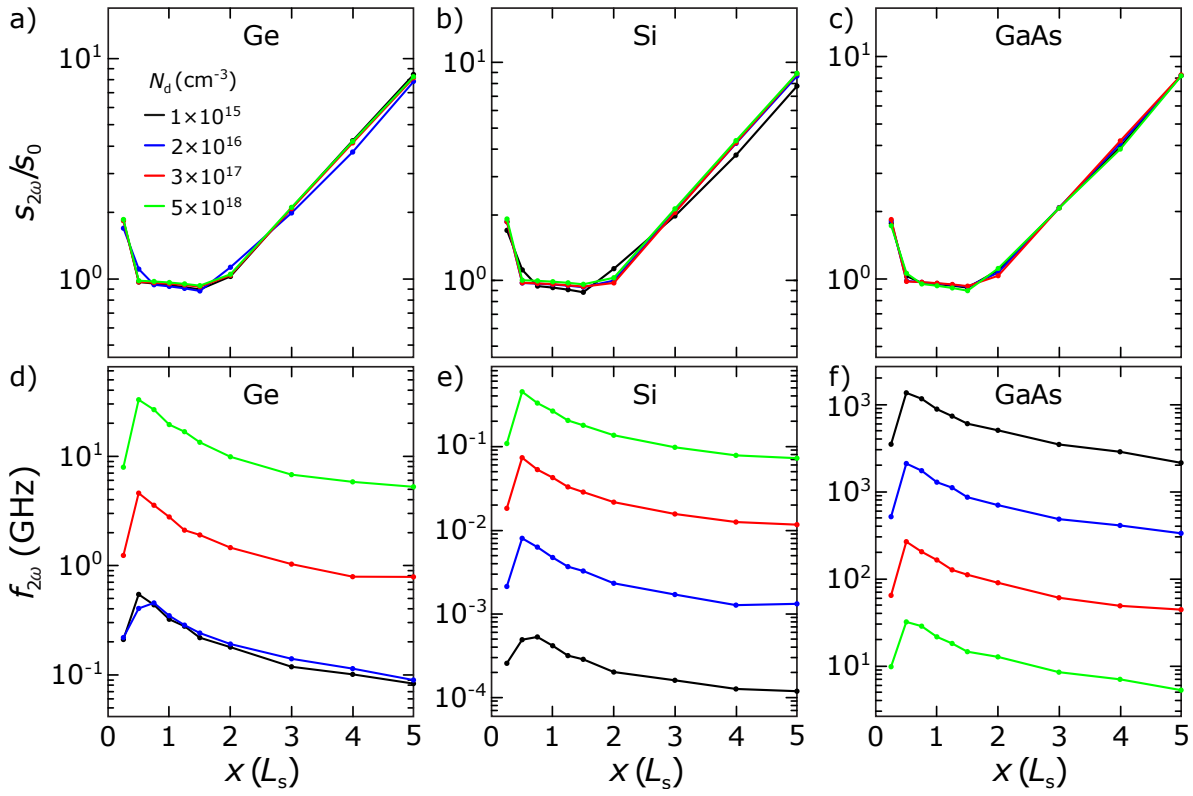

Figure 3.21: (a-c) The $s_{2\omega}/s_0$ and (d-f) $f_{2\omega}$ as functions of the injector-detector distance x for Ge, Si, and GaAs. The N_d ranges between 1×10^{15} cm^{-3} (black), 2×10^{16} cm^{-3} (blue), 3×10^{17} cm^{-3} (red) and 5×10^{18} cm^{-3} (green). All the data are evaluated for $E_0 = 10\, E_{0,\mathrm{max}}$ and $s_{2\omega}/s_0$ is calculated with a modulation frequency $f < f_{2\omega}$.

by using bias voltages commonly employed in electronics. Our simulations finally suggest that strong electric fields and small spin diffusion lengths enable faster modulation.

Conclusions

The work presented in this thesis has addressed two complementary aspects of semiconductor spintronics: the optical orientation and electrical detection of spin currents in a new platform, $CdGeAs_2$, and the investigation of the dynamical limits of the electrical modulation of spin signals in the drift-diffusion regime. Taken together, these results provide a clearer picture of the microscopic properties that make a semiconductor attractive for spin-based applications.

With regard to $CdGeAs_2$, this thesis has shown that this chalcopyrite semiconductor exhibits electronic properties that are particularly favorable for spin-to-charge conversion. ARPES measurements made it possible to resolve the valence-band structure near the band gap and to constrain the parameters of the 8-band $k \cdot p$ model, establishing a solid framework for the interpretation of optical orientation and of the ISHE response. The photoinduced ISHE experiment revealed a spectral dependence of the signal, characterized by a pronounced maximum around 0.7 eV and by an almost constant behavior up to approximately 1.15 eV. Comparison between experiment and theory indicates that the response is dominated by VB1 $\rightarrow$ CB transitions at lower photon energies and the onset of transitions from VB2 substantially alters the spectral behavior. The same analysis further indicates that $CdGeAs_2$ is characterized by a short spin diffusion length, on the order of $L_s \lesssim 100$ nm, considerably smaller than the micrometer-scale values typical of Si and Ge and comparable to that of GaAs. Moreover, the ISHE signal is larger than that measured in Ge under similar conditions, pointing to a stronger spin-to-charge conversion efficiency in this semiconductor.

The second part of the thesis has shown that short spin diffusion lengths, although unfavorable for long-range information transfer, enables very fast electrical control. Simulations of the frequency response of spin transport, obtained by solving the time-dependent drift-diffusion and continuity equations under oscillating electric fields, revealed two distinct regimes determined by the field amplitude: a weak-field regime dominated by the first harmonic of the spin density and a strong-field regime in which the second harmonic becomes dominant. The key result is that the cutoff frequency increases as the spin diffusion length decreases. In the strong-field regime, the calculated characteristic frequencies

reach about 35 GHz in heavily doped Ge, 480 MHz in heavily doped Si, and up to 15 THz in weakly doped GaAs. Although these values should be regarded as ideal upper limits, they nevertheless demonstrate that drift-diffusive transport does not in itself preclude high-frequency spin-logic operation.

Overall, this thesis establishes a coherent connection between electronic structure, optical orientation, spin-to-charge conversion, and time-dependent spin transport. In light of these results, $CdGeAs_2$ emerges as a particularly interesting case. The experimental results show that it combines a clearly measurable spin-to-charge conversion response with a spin diffusion length similar to that of GaAs, namely the material that, among those considered in this work, exhibits the fastest dynamical response. This suggests that $CdGeAs_2$ should be regarded not only as a promising platform for spin-current detection, but also as a credible candidate for high-speed spin manipulation.

Bibliography

[1] M. N. Baibich, J. M. Broto, A. Fert, *et al.*, "Giant magnetoresistance of (001)Fe/(001)Cr magnetic superlattices," *Physical Review Letters* **61**, 2472 (1988).

[2] G. Binasch, P. Grünberg, F. Saurenbach, and W. Zinn, "Enhanced magnetoresistance in layered magnetic structures with antiferromagnetic interlayer exchange," *Physical review B* **39**, 4828 (1989).

[3] D. C. Ralph and M. D. Stiles, "Spin transfer torques," *Journal of Magnetism and Magnetic Materials* **320**, 1190–1216 (2008).

[4] C. Song, R. Zhang, L. Liao, *et al.*, "Spin-orbit torques: Materials, mechanisms, performances, and potential applications," *Progress in Materials Science* **118**, 100761 (2021).

[5] L. Liu, C.-F. Pai, Y. Li, H. Tseng, D. Ralph, and R. Buhrman, "Spin-torque switching with the giant spin Hall effect of tantalum," *Science* **336**, 555–558 (2012).

[6] I. M. Miron, K. Garello, G. Gaudin, *et al.*, "Perpendicular switching of a single ferromagnetic layer induced by in-plane current injection," *Nature* **476**, 189–193 (2011).

[7] Q. Shao, P. Li, L. Liu, *et al.*, "Roadmap of spin–orbit torques," *IEEE Transactions on Magnetics* **57**, 1–39 (2021).

[8] S. G. Tan and M. B. Jalil, *Introduction to the physics of nanoelectronics*. Elsevier, 2012.

[9] G. Prenat, K. Jabeur, P. Vanhauwaert, *et al.*, "Ultra-fast and high-reliability SOT-MRAM: From cache replacement to normally-off computing," *IEEE Transactions on Multi-Scale Computing Systems* **2**, 49–60 (2015).

[10] International Energy Agency, "Energy and AI," Tech. Rep., 2025. [Online]. Available: `https://www.iea.org/reports/energy-and-ai`.

[11] J. Fabian, A. Matos-Abiague, C. Ertler, P. Stano, and I. Žutić, "Semiconductor spintronics," *Acta Phys. Slovaca* **57**, 565 (2007).

[12] I. Žutić, J. Fabian, and S. Das Sarma, "Spintronics: Fundamentals and applications," *Rev. Mod. Phys.* **76**, 323–410 (2004).

[13] D. Awschalom and M. E. Flatté, "Challenges for semiconductor spintronics," *Nat. Phys* **3**, 153–159 (2007).

[14] M. Julliere, "Tunneling between ferromagnetic films," *Physics letters A* **54**, 225–226 (1975).

[15] R. Jansen, "Silicon spintronics," *Nat. Mater* **11**, 400–408 (2012).

[16] M. I. Dyakonov and V. I. Perel, "Current-induced spin orientation of electrons in semiconductors," *Phys. Lett. A* **35**, 459–460 (1971).

[17] W. Pötz, J. Fabian, and U. Hohenester, *Modern aspects of spin physics*. Springer Science & Business Media, 2006, 712.

[18] K. Wang, F. Xiu, and A. Jacob, "Spintronics of nanostructured manganese germanium (MnGe) dilute magnetic semiconductor," in *Silicon–Germanium (SiGe) Nanostructures*, Elsevier, 2011, 575–609.

[19] F. Meier and B. P. Zakharchenya, *Optical orientation*. Elsevier, 2012.

[20] M. I. Dyakonov and A. Khaetskii, *Spin physics in semiconductors*. Springer, 2008, 157.

[21] F. Bottegoni, M. Celebrano, M. Bollani, *et al.*, "Spin voltage generation through optical excitation of complementary spin populations," *Nat. Mater* **13**, 790–795 (2014).

[22] M. Finazzi, F. Bottegoni, C. Zucchetti, *et al.*, "Optical orientation and inverse spin Hall effect as effective tools to investigate spin-dependent diffusion," *Electronics* **5**, 80 (2016).

[23] T. Guillet, C. Zucchetti, A. Marchionni, *et al.*, "Spin orbitronics at a topological insulator-semiconductor interface," *Phys. Rev. B* **101**, 184406 (2020).

[24] G. Lampel, "Nuclear dynamic polarization by optical electronic saturation and optical pumping in semiconductors," *Physical Review Letters* **20**, 491 (1968).

[25] V. I. Belinicher and B. I. Sturman, "The photogalvanic effect in media lacking a center of symmetry," *Soviet Physics Uspekhi* **23**, 199 (1980).

[26] V. Berkovits, A. Ekimov, and V. Safarov, "Optical orientation in a system of electrons and lattice nuclei in semiconductors-experiment," *Zh. Eksp. Teor. Fiz* **65**, 346 (1973).

[27] Y. K. Kato, R. C. Myers, A. C. Gossard, and D. D. Awschalom, "Observation of the spin Hall effect in semiconductors," *Sci.* **306**, 1910–1913 (2004).

[28] J. Wunderlich, B. Kaestner, J. Sinova, and T. Jungwirth, "Experimental observation of the spin-Hall effect in a two-dimensional spin-orbit coupled semiconductor system," *Physical review letters* **94**, 047204 (2005).

[29] J. Sinova, S. O. Valenzuela, J. Wunderlich, C. H. Back, and T. Jungwirth, "Spin Hall effects," *Reviews of modern physics* **87**, 1213–1260 (2015).

[30] A. Bakun, B. Zakharchenya, A. Rogachev, M. Tkachuk, and V. Fleisher, "Observation of a surface photocurrent caused by optical orientation of electrons in a semiconductor," *Jetp Lett* **40**, 464–466 (1984).

[31] E. Saitoh, M. Ueda, H. Miyajima, and G. Tatara, "Conversion of spin current into charge current at room temperature: Inverse spin-Hall effect," *Applied physics letters* **88**, 182509 (2006).

[32] S. O. Valenzuela and M. Tinkham, "Direct electronic measurement of the spin Hall effect," *Nature* **442**, 176–179 (2006).

[33] H. Zhao, E. J. Loren, H. Van Driel, and A. L. Smirl, "Coherence control of Hall charge and spin currents," *Physical review letters* **96**, 246601 (2006).

[34] B. A. Bernevig and S.-C. Zhang, "Quantum spin Hall effect," *Physical review letters* **96**, 106802 (2006).

[35] X. Chen, S. Shi, G. Shi, *et al.*, "Observation of the antiferromagnetic spin Hall effect," *Nature Materials* **20**, 800–804 (2021).

[36] K. Kang, B. Shen, Y. Qiu, *et al.*, "Evidence of the fractional quantum spin Hall effect in moiré $MoTe_2$," *Nature* **628**, 522–526 (2024).

[37] M. Carrega, L. Chirolli, S. Heun, and L. Sorba, "Anyons in quantum Hall interferometry," *Nature Reviews Physics* **3**, 698–711 (2021).

[38] C. Zucchetti, F. Bottegoni, C. Vergnaud, *et al.*, "Imaging spin diffusion in germanium at room temperature," *Phys. Rev. B* **96**, 014403 (2017).

[39] F. Rortais, C. Vergnaud, C. Ducruet, *et al.*, "Electrical spin injection in silicon and the role of defects," *Physical Review B* **94**, 174426 (2016).

[40] M. Yamada, M. Tsukahara, Y. Fujita, *et al.*, "Room-temperature spin transport in n-Ge probed by four-terminal nonlocal measurements," *Appl. Phys. Express* **10**, 093001 (2017).

[41] F. Bloch, "Nuclear induction," *Physical review* **70**, 460 (1946).

[42] S. Datta and B. Das, "Electronic analog of the electro-optic modulator," *Appl. Phys. Lett.* **56**, 665–667 (1990).

[43] J. Nitta, T. Akazaki, H. Takayanagi, and T. Enoki, "Gate Control of Spin-Orbit Interaction in an Inverted $In_{0.53}Ga_{0.47}As/In_{0.52}Al_{0.48}As$ Heterostructure," *Physical Review Letters* **78**, 1335 (1997).

[44] J. H. Smet, R. A. Deutschmann, F. Ertl, W. Wegscheider, G. Abstreiter, and K. Von Klitzing, "Gate-voltage control of spin interactions between electrons and nuclei in a semiconductor," *Nat.* **415**, 281–286 (2002).

[45] P. Chuang, S. C. Ho, L. W. Smith, *et al.*, "All-electric all-semiconductor spin field-effect transistors," *Nat. Nanotechnol* **10**, 35–39 (2014).

[46] C. Morrison, P. Wiśniewski, S. D. Rhead, J. Foronda, D. R. Leadley, and M. Myronov, "Observation of Rashba zero-field spin splitting in a strained germanium 2D hole gas," *Appl. Phys. Lett.* **105** (2014).

[47] Z. G. Yu and M. E. Flatté, "Electric-field dependent spin diffusion and spin injection into semiconductors," *Phys. Rev. B* **66**, 201202 (2002).

[48] C. Zucchetti, A. Marchionni, M. Bollani, F. Ciccacci, M. Finazzi, and F. Bottegoni, "Electric field modulation of spin transport," *APL Mater.* **10**, 011102 (2022).

[49] C. Zucchetti, F. Scali, P. Grassi, *et al.*, "Non-local architecture for spin current manipulation in silicon platforms," *APL Mater.* **11**, 021102 (2023).

[50] K. S. Novoselov, A. K. Geim, S. V. Morozov, *et al.*, "Electric field effect in atomically thin carbon films," *science* **306**, 666 (2004).

[51] F. Scali, C. Zucchetti, L. Anzi, V. Falcone, and F. Bottegoni, "Photo-induced inverse spin Hall effect detection of spin-polarized holes in semiconductors," in *Spintronics XVII*, SPIE, 13119, 2024, 48–55.

[52] W. Pauli, "The connection between spin and statistics," *Physical Review* **58**, 716 (1940).

[53] J. Kessler, *Polarized electrons*. Springer Science & Business Media, 1985, 1.

[54] J. J. Sakurai and J. Napolitano, *Modern quantum mechanics*. Cambridge University Press, 2020.

[55] M. Cardona and F. H. Pollak, "Energy-band structure of germanium and silicon: The k·p method," *Physical Review* **142**, 530 (1966).

[56] E. O. Kane, "Band structure of indium antimonide," *Journal of Physics and Chemistry of Solids* **1**, 249–261 (1957).

[57] J. C. Slater and G. F. Koster, "Simplified LCAO method for the periodic potential problem," *Physical review* **94**, 1498 (1954).

[58] M. L. Cohen and T. Bergstresser, "Band structures and pseudopotential form factors for fourteen semiconductors of the diamond and zinc-blende structures," *Physical Review* **141**, 789 (1966).

[59] G. Weisz, "Band structure and fermi surface of white tin," *Physical Review* **149**, 504 (1966).

[60] W. Kohn and L. J. Sham, "Self-consistent equations including exchange and correlation effects," *Physical review* **140**, A1133 (1965).

[61] L. L. Foldy and S. A. Wouthuysen, "On the Dirac theory of spin 1/2 particles and its non-relativistic limit," *Physical Review* **78**, 29 (1950).

[62] W. Greiner *et al.*, *Relativistic quantum mechanics*. Springer, 1990, 3.

[63] M. Cardona and Y. Y. Peter, *Fundamentals of semiconductors*. Springer, 2005, 619.

[64] F. Nastos, J. Rioux, M. Strimas-Mackey, B. S. Mendoza, and J. Sipe, "Full band structure LDA and k·p calculations of optical spin-injection," *Physical Review B* **76**, 205113 (2007).

[65] O. Svelto, D. C. Hanna, *et al.*, *Principles of lasers*. Springer, 2010, 1.

[66] S. Richard, F. Aniel, and G. Fishman, "Energy-band structure of Ge, Si, and GaAs: A thirty-band k·p method," *Physical Review B—Condensed Matter and Materials Physics* **70**, 235204 (2004).

[67] J. Cheng, J. Rioux, J. Fabian, and J. E. Sipe, "Theory of optical spin orientation in silicon," *Phys. Rev. B* **83**, 165211 (2011).

[68] C. Zucchetti, F. Bottegoni, G. Isella, *et al.*, "Spin-to-charge conversion for hot photoexcited electrons in germanium," *Phys. Rev. B* **97**, 125203 (2018).

[69] G. Dresselhaus, "Spin-orbit coupling effects in zinc blende structures," *Physical Review* **100**, 580 (1955).

[70] R. Winkler, *Spin-orbit coupling effects in two-dimensional electron and hole systems*. Springer, 2003, 191.

[71] J. Rioux and J. Sipe, "Optical injection and control in germanium: Thirty-band k·p theory," *Physical Review B* **81**, 155215 (2010).

[72] P. Enders, A. Bärwolff, M. Woerner, and D. Suisky, "K·p theory of energy bands, wave functions, and optical selection rules in strained tetrahedral semiconductors," *Physical Review B* **51**, 16695 (1995).

[73] J. L. Cheng, M. W. Wu, and J. Fabian, "Theory of the spin relaxation of conduction electrons in silicon," *Phys. Rev. Lett.* **104**, 016601 (2010).

[74] F. Baumgartner, M. Lux-Steiner, and E. Bucher, "Growth of $CdGeAs_2$ single crystals by the chemical vapor transport method," *Journal of electronic materials* **19**, 777–781 (1990).

[75] S. Abrahams and J. Bernstein, "Piezoelectric nonlinear optic $CuGaSe_2$ and $CdGeAs_2$: Crystal structure, chalcopyrite microhardness, and sublattice distortion," *The Journal of Chemical Physics* **61**, 1140–1146 (1974).

[76] H. Kildal, "Band structure of $CdGeAs_2$ near $\overrightarrow{k} = 0$," *Physical Review B* **10**, 5082 (1974).

[77] S. Limpijumnong and W. R. Lambrecht, "Band structure of $CdGeAs_2$ near the fundamental gap," *Physical Review B* **65**, 165204 (2002).

[78] A. Shileika, "Energy band structure and modulation spectra of $A^2B^4C_2^5$ semiconductors," *Surface Science* **37**, 730–747 (1973).

[79] K. Cho, "Unified theory of symmetry-breaking effects on excitons in cubic and wurtzite structures," *Physical Review B* **14**, 4463 (1976).

[80] W. Zhang, V. Vlaminck, J. E. Pearson, R. Divan, S. D. Bader, and A. Hoffmann, "Determination of the Pt spin diffusion length by spin-pumping and spin Hall effect," *Applied Physics Letters* **103**, 242414 (2013).

[81] A. Azevedo, L. Vilela-Leão, R. Rodríguez-Suárez, A. L. Santos, and S. Rezende, "Spin pumping and anisotropic magnetoresistance voltages in magnetic bilayers: Theory and experiment," *Physical review B* **83**, 144402 (2011).

[82] K. Ando, S. Takahashi, K. Harii, *et al.*, "Electric manipulation of spin relaxation using the spin Hall effect," *Physical Review Letters* **101**, 036601 (2008).

[83] M. Obstbaum, M. Härtinger, H. Bauer, *et al.*, "Inverse spin Hall effect in $Ni_{81}Fe_{19}$/normal-metal bilayers," *Physical Review B* **89**, 060407 (2014).

[84] M. Isasa, E. Villamor, L. E. Hueso, M. Gradhand, and F. Casanova, "Temperature dependence of spin diffusion length and spin Hall angle in Au and Pt," *Physical Review B* **91**, 024402 (2015).

[85] K. Ando and E. Saitoh, "Observation of the inverse spin Hall effect in silicon," *Nat. Commun* **3**, 629 (2012).

[86] F. Bottegoni, A. Ferrari, G. Isella, M. Finazzi, and F. Ciccacci, "Experimental evaluation of the spin-Hall conductivity in Si-doped GaAs," *Physical Review B* **88**, 121201 (2013).

[87] J.-C. Rojas-Sánchez, M. Cubukcu, A. Jain, *et al.*, "Spin pumping and inverse spin Hall effect in germanium," *Physical Review B* **88**, 064403 (2013).

[88] N. Okamoto, H. Kurebayashi, T. Trypiniotis, *et al.*, "Electric control of the spin Hall effect by intervalley transitions," *Nature Materials* **13**, 932–937 (2014).

[89] N. Nagaosa, J. Sinova, S. Onoda, A. H. MacDonald, and N. P. Ong, "Anomalous Hall effect," *Reviews of modern physics* **82**, 1539–1592 (2010).

[90] N. Sinitsyn, A. MacDonald, T. Jungwirth, V. Dugaev, and J. Sinova, "Anomalous Hall effect in a two-dimensional Dirac band: The link between the Kubo-Streda formula and the semiclassical Boltzmann equation approach," *Physical Review B—Condensed Matter and Materials Physics* **75**, 045315 (2007).

[91] N. F. Mott, "The scattering of fast electrons by atomic nuclei," *Proceedings of the Royal Society of London. Series A, Containing Papers of a Mathematical and Physical Character* **124**, 425–442 (1929).

[92] S. Murakami, N. Nagaosa, and S.-C. Zhang, "Dissipationless quantum spin current at room temperature," *Science* **301**, 1348–1351 (2003).

[93] R. Kubo, "Statistical-mechanical theory of irreversible processes. i. General theory and simple applications to magnetic and conduction problems," *Journal of the physical society of Japan* **12**, 570–586 (1957).

[94] J. Sinova, D. Culcer, Q. Niu, N. Sinitsyn, T. Jungwirth, and A. H. MacDonald, "Universal intrinsic spin Hall effect," *Physical review letters* **92**, 126603 (2004).

[95] L. Berger, "Side-jump mechanism for the Hall effect of ferromagnets," *Physical Review B* **2**, 4559 (1970).

[96] R. J. Elliott, "Spin-Orbit Coupling in Band Theory—Character Tables for Some "Double" Space Groups," *Phys. Rev.* **96**, 280 (1954).

[97] Y. Yafet, "g Factors and spin-lattice relaxation of conduction electrons," in *Solid State Phys.* 14, Elsevier, 1963, 1–98.

[98] G. Pikus and A. Titkov, "Spin relaxation under optical orientation in semiconductors," *Optical Orientation* **8**, 73–131 (1984).

[99] J.-N. Chazalviel, "Spin relaxation of conduction electrons in n-type indium antimonide at low temperature," *Physical Review B* **11**, 1555 (1975).

[100] G. Bir, A. Aronov, and G. Pikus, "Spin relaxation of electrons due to scattering by holes," *Zh. Eksp. Teor. Fiz* **69**, 1382 (1975).

[101] M. P. Seah and W. Dench, "Quantitative electron spectroscopy of surfaces: A standard data base for electron inelastic mean free paths in solids," *Surface and interface analysis* **1**, 2–11 (1979).

[102] A. Damascelli, Z. Hussain, and Z.-X. Shen, "Angle-resolved photoemission studies of the cuprate superconductors," *Reviews of modern physics* **75**, 473 (2003).

[103] M. Binnewies, R. Glaum, M. Schmidt, and P. Schmidt, *Chemical vapor transport reactions*. Walter de Gruyter, 2012.

[104] H. Zhang, T. Pincelli, C. Jozwiak, *et al.*, "Angle-resolved photoemission spectroscopy," *Nature Reviews Methods Primers* **2**, 54 (2022).

[105] C. Zucchetti, "Spin-charge interconversion in Ge-based structures," *Ph.D. thesis, Politecnico di Milano, Department of Physics* (2019).

[106] A. Bostwick, T. Ohta, T. Seyller, K. Horn, and E. Rotenberg, "Quasiparticle dynamics in graphene," *Nature physics* **3**, 36–40 (2007).

[107] Z. Liu, J. Jiang, B. Zhou, *et al.*, "A stable three-dimensional topological Dirac semimetal Cd_3As_2," *Nature materials* **13**, 677–681 (2014).

[108] S. Xue, J. Ning, B. Zhang, Q. Wu, F. Zhang, and W. Zhang, "The Electronic Structure and Optical Properties of CdGeAs2 Crystal: A DFT and HSE06 Study," *Coatings* **12**, 1778 (2022).

[109] A. Marchionni, C. Zucchetti, F. Ciccacci, *et al.*, "Inverse spin-Hall effect in GeSn," *Appl. Phys. Lett.* **118**, 212402 (2021).

[110] F. Bottegoni, C. Zucchetti, G. Isella, E. Pinotti, M. Finazzi, and F. Ciccacci, "Modeling the photo-induced inverse spin-Hall effect in Pt/semiconductor junctions," *J. Appl. Phys.* **124**, 033902 (2018).

[111] F. Scali, M. Finazzi, F. Bottegoni, and C. Zucchetti, "Frequency response of spin drift-diffusion in n-doped Ge, Si, and GaAs," *Journal of Applied Physics* **137**, 063906 (2025).

[112] F. Bottegoni, C. Zucchetti, F. Ciccacci, M. Finazzi, and G. Isella, "Optical generation of pure spin currents at the indirect gap of bulk Si," *Appl. Phys. Lett.* **110**, 042403 (2017).

[113] C. Zucchetti, F. Scali, A. Ballabio, *et al.*, "Hole and electron spin lifetime in lightly n-doped silicon at low temperatures," *Appl. Phys. Lett.* **125**, 172404 (2024).

[114] M. V. Fischetti, "Monte Carlo simulation of transport in technologically significant semiconductors of the diamond and zinc-blende structures. I. Homogeneous transport," *IEEE Trans. Electron Devices* **38**, 634–649 (1991).

[115] M. V. Fischetti and J. M. Higman, "Theory and Calculation of the Deformation Potential Electron-Phonon Scattering Rates in Semiconductors," in *Monte Carlo Device Simulation: Full Band and Beyond*. Springer US, 1991, 123–160.

[116] M. Lundstrom, "Fundamentals of carrier transport, 2nd edn," *Meas. Sci. Technol.* **13**, 230–230 (2002).

[117] P. Li, Y. Song, and H. Dery, "Intrinsic spin lifetime of conduction electrons in germanium," *Phys. Rev. B* **86**, 085202 (2012).

[118] Y. Song, O. Chalaev, and H. Dery, "Donor-driven spin relaxation in multivalley semiconductors," *Phys. Rev. Lett.* **113**, 167201 (2014).

[119] T. Suzuki, T. Sasaki, T. Oikawa, M. Shiraishi, Y. Suzuki, and K. Noguchi, "Room-temperature electron spin transport in a highly doped Si channel," *Appl. Phys. Express* **4**, 023003 (2011).

[120] S. P. Dash, S. Sharma, R. S. Patel, M. P. de Jong, and R. Jansen, "Electrical creation of spin polarization in silicon at room temperature," *Nature* **462**, 491–494 (2009).

[121] K.-R. Jeon, B.-C. Min, I.-J. Shin, *et al.*, "Electrical spin accumulation with improved bias voltage dependence in a crystalline CoFe/MgO/Si system," *Applied Physics Letters* **98**, 262102 (2011).

[122] P. Li and H. Dery, "Spin-orbit symmetries of conduction electrons in silicon," *Phys. Rev. Lett.* **107**, 107203 (2011).

[123] C. Zucchetti, M. Bollani, G. Isella, M. Zani, M. Finazzi, and F. Bottegoni, "Doping dependence of the electron spin diffusion length in germanium," *APL Mater.* **7**, 101122 (2019).

[124] F. Rortais, C. Vergnaud, A. Marty, *et al.*, "Non-local electrical spin injection and detection in germanium at room temperature," *Appl. Phys. Lett.* **111**, 182401 (2017).

[125] S. Oertel, J. Huebner, and M. Oestreich, "High temperature electron spin relaxation in bulk GaAs," *Appl. Phys. Lett.* **93**, 132112 (2008).

[126] J. H. Jiang and M. W. Wu, "Electron-spin relaxation in bulk III–V semiconductors from a fully microscopic kinetic spin Bloch equation approach," *Phys. Rev. B* **79**, 125206 (2009).

[127] V. I. Fistul, M. I. Iglitsyn, and E. M. Omelyanovskii, "Mobility of electrons in germanium strongly doped with arsenic," *Sov. Phys. Solid State* **9**, 784-785 (1962).

[128] M. Sotoodeh, A. H. Khalid, and A. A. Rezazadeh, "Empirical low-field mobility model for III–V compounds applicable in device simulation codes," *J. Appl. Phys.* **87**, 2890–2900 (2000).

[129] C. Jacoboni, C. Canali, G. Ottaviani, and A. A. Quaranta, "A review of some charge transport properties of silicon," *Solid-State Electron.* **20**, 77–89 (1977).

Appendix

Appendix A: Transition rates in $CdGeAs_2$

For a light wavevector parallel to the c axis, the polarization unit vectors for right-handed (σ^-) and left-handed (σ^+) circularly polarized light are given by:

$$\sigma^+ \longrightarrow \mathbf{e}^+ = \frac{1}{\sqrt{2}}(\mathbf{e}_\mathrm{x} + i\mathbf{e}_\mathrm{y}), \tag{3.41a}$$

$$\sigma^- \longrightarrow \mathbf{e}^- = \frac{1}{\sqrt{2}}(\mathbf{e}_\mathrm{x} - i\mathbf{e}_\mathrm{y}). \tag{3.41b}$$

where $\mathbf{e}_\mathrm{x}$ and $\mathbf{e}_\mathrm{y}$ are the unit vectors of the a and b axes in Fig. 1.5a, respectively. The FGR within the electric dipole approximation, reported in Eq. (1.47), is used to calculate the transition rates from the VBs to the CB. Neglecting constant terms, it reads:

$$W_{\mathrm{i,f}}(\mathbf{k}) \propto M_{\mathrm{i,f}}(\mathbf{k})^2 \delta[E_\mathrm{f}(\mathbf{k}) - E_\mathrm{i}(\mathbf{k}) - \hbar\omega], \tag{3.42}$$

where $M_{\mathrm{i,f}}(\mathbf{k}) = |\mathbf{e} \cdot \langle\phi_\mathrm{f}| \hat{\mathbf{p}} |\phi_\mathrm{i}\rangle|$. The eigenstates at the Γ point of $CdGeAs_2$ (Table. 1.1) can be used as the final $|\phi_\mathrm{f}\rangle$ and the initial $|\phi_\mathrm{i}\rangle$ states, while the momentum operator is $\hat{\mathbf{p}} = -i\hbar\nabla$. For the following analysis, it is useful to define:

$$-i\hbar \langle S| \frac{\partial}{\partial x} |X\rangle = -i\hbar \langle S| \frac{\partial}{\partial y} |Y\rangle = \iota, \tag{3.43}$$

and to remind $\langle\uparrow \mid \downarrow\rangle = 0$ and $\langle\uparrow \mid \uparrow\rangle = 1$. By considering solely optical transitions induced by σ^- polarization with $\mathbf{e} = \mathbf{e}^-$ allowed by dipole selection rules between the three VBs and the CB in Fig. 3.4 (an analogous argument applies to σ^+ polarization and leads to the same conclusions), the transition rates can be calculated as follows:

- VB1→CB:

$$\begin{aligned} W_{\mathrm{VB1,CB}} &\propto |\mathbf{e}^- \cdot \langle -iS\downarrow| - i\hbar\nabla| - \frac{AB}{\sqrt{2}}\left[(X+iY)\downarrow - \sqrt{2}Z\uparrow\right]\rangle|^2 \\ &= |\frac{AB}{2} i(-i\hbar)\langle S|\frac{\partial}{\partial x} - i\frac{\partial}{\partial y}|X+iY\rangle|^2 \\ &= \iota|AB|^2; \end{aligned} \tag{3.44}$$

- VB2→CB:

$$\begin{aligned} W_{\mathrm{VB2,CB}} &\propto |\mathbf{e}^- \cdot \langle -iS\uparrow| - i\hbar\nabla|\frac{1}{\sqrt{2}}(X+iY)\uparrow\rangle|^2 \\ &= |-\frac{1}{2} i(-i\hbar)\langle S|\frac{\partial}{\partial x} - i\frac{\partial}{\partial y}|X+iY\rangle|^2 \\ &= \iota; \end{aligned} \tag{3.45}$$

- VB3→CB:

$$\begin{aligned} W_{\mathrm{VB3,CB}} &\propto |\mathbf{e}^- \cdot \langle -iS\downarrow| - i\hbar\nabla| - \frac{CD}{\sqrt{2}}\left[(X+iY)\downarrow - \sqrt{2}Z\uparrow\right]\rangle|^2 \\ &= |\frac{CD}{2} i(-i\hbar)\langle S|\frac{\partial}{\partial x} - i\frac{\partial}{\partial y}|X+iY\rangle|^2 \\ &= \iota|CD|^2. \end{aligned} \tag{3.46}$$

Appendix B: Thomas-Fermi screening length

The Thomas-Fermi screening length used to calculate the impurity-scattering time in Sec. 3.4 is derived from the Thomas-Fermi wavevector in SI units:

$$k_{\mathrm{TF}}^2 = \frac{q^2}{\epsilon}\frac{\partial n}{\partial \mu}, \tag{3.47}$$

being μ the chemical potential and n the electron density. At $T = 0\,\mathrm{K}$:

$$\frac{\partial n}{\partial \mu} = g(E_{\mathrm{F}}), \tag{3.48}$$

being $g(E_{\mathrm{F}})$ the density of states at the Fermi level. This is expressed:

$$g(E_{\mathrm{F}}) = \frac{m^* k_{\mathrm{F}}}{\pi^2 \hbar^2}, \tag{3.49}$$

with k_{F} the Fermi wavevector. For a degenerate semiconductor:

$$k_{\mathrm{F}} = (3\pi^2 N_{\mathrm{d}})^{1/3}. \tag{3.50}$$

Thus:

$$k_{\mathrm{TF}}^2 = \frac{q^2}{\epsilon}\frac{m^*}{\pi^2\hbar^2}(3\pi^2 N_{\mathrm{d}})^{1/3}, \tag{3.51a}$$

$$l_{\mathrm{TF}} = \frac{1}{k_{\mathrm{TF}}} = \left(\frac{q^2 m^* (3\pi^2 N_{\mathrm{d}})^{1/3}}{\epsilon \pi^2 \hbar^2}\right)^{-1/2}, \tag{3.51b}$$

which is Eq. (3.31) used in Sec. 3.4. This equation is strictly valid only for a degenerate semiconductor at $T = 0\,\mathrm{K}$. Here, we use the same derivation to estimate l_{TF} for non-degenerate semiconductors at 300 K, where it provides only an approximate result.

Appendix C: List of publications

- C. Zucchetti, F. Scali, P. Grassi, M. Bollani, L. Anzi, G. Isella, M. Finazzi, F. Ciccacci, and F. Bottegoni. Non-local architecture for spin current manipulation in silicon platforms. *Applied Physics Letters Materials* **11**, 021102 (2023).
- C. Zucchetti, F. Scali, A. Ballabio, M. Bollani, G. Isella, G. Ferrari, M. Finazzi, F. Ciccacci, and F. Bottegoni. Hole and electron spin lifetime in lightly n-doped silicon at low temperatures. *Applied Physics Letters* **125**, 172404 (2024).
- F. Scali, C. Zucchetti, L. Anzi, V. Falcone, and F. Bottegoni. Photo-induced inverse spin Hall effect detection of spin-polarized holes in semiconductors. *Proceedings Volume 13119, Spintronics XVII* **137**, 1311905 (2024).
- F. Scali, M. Finazzi, F. Bottegoni, and C. Zucchetti. Frequency response of spin drift-diffusion in n-doped Ge, Si, and GaAs. *Journal of Applied Physics* **137**, 063906 (2025).
- F. Scali, M. Finazzi, F. Bottegoni, and C. Zucchetti. Optically induced orbital polarization in bulk germanium. *arXiv preprint arXiv:2510.09525* **137** (2025).
- E. Tavaglione, E. Spagnoli, M. Valt, P. Bernardoni, M. Della Ciana, F. Bottegoni, M. Negri, F. Scali, C. Zucchetti, M. Ferroni, M. Ardit, L. Vanzetti, V. Cristino, F. Di Benedetto, and B. Fabbri. Photosensitivity and gas sensing mechanisms: Validation of an *operando* DRIFT spectroscopy apparatus for light-activated chemoresistive gas sensors. *Sensors and Actuators B: Chemical* **444**, 138504 (2025).
- C. Li, M. Hu, J. Zhang, M. H. Berntsen, F. Scali, D. Phuyal, C. Lin, W. Chen, J. Chang, O. J. Clark, T. K. Kim, J. Osiecki, C. Polley, B. Thiagarajan, Z. Li, T. Xiang, and O. Tjernberg. Extreme Strain Controlled Correlated Metal-Insulator Transition in the Altermagnet CrSb. *arXiv preprint arXiv:2512.07683* (2025).
- C. Li, Z. Yang, H. Liu, M. H. Berntsen, F. Scali, D. Phuyal, J. Zhang, T. K. Kim, J. Osiecki, C. Polley, B. Thiagarajan, Y. Shi, T. Xiang, Q. Wu, and O. Tjernberg. Hidden Moiré Topology of Low-Symmetry Weyl Surfaces. *arXiv preprint arXiv:2509.10106* (2025).